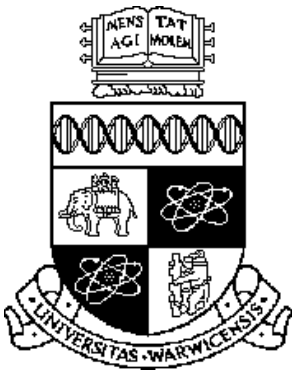

New Approaches in Optical Interferometry

Zuobin Wang

Centre for Nanotechnology and Microengineering

Department of Engineering

University of Warwick

Coventry

U.K.

Being a thesis submitted for the degree of

Doctor of Philosophy

28 April 1997

Declaration

I declare that this thesis is presented in accordance with the regulations for the degree of Doctor of Philosophy. It has been composed by myself and has not been submitted previously for a degree at any other university. All work shown has been done by myself unless stated otherwise.

Zuobin Wang

Acknowledgement

The main financial support of my PhD study from Sir Yue-Kong Pao Foundation through the Sino-British Friendship Scholarship Scheme (SBFSS) is gratefully acknowledged, and my sincere thanks go to all the people working on the Scheme.

In this thesis, I would also like to acknowledge the help and assistance from the following people during the three years of my PhD study. I could not have completed my thesis smoothly without their help.

Firstly, I would like to express my sincere gratitude to my supervisor, Professor P.J. Bryanston-Cross, on his precise guidance, and kind help throughout the duration of my PhD study.

I am very grateful to Professor D.J. Whitehouse for his time and effort to solve my personal problems.

I would also like to thank all the members of our research group, especially Dr C. Quan, Mr W.K. Lee, Dr P.H. Chan, Mr L. Davis, Mr H. Edwards, Mr D. Robinson, and Mr R.N. Davies for their considerate assistance.

Many thanks go to my friends, especially Dr N. Brown, Mr A. Dowell, Mr A.A. Brown, Professor T. Huang, and Professor F. Wang for their kind help during the period of my PhD study.

Finally, my special thanks go to my parents, my wife and my son for their constant support and encouragement.

Abstract

This thesis presents two new approaches in optical interferometry: phase difference determination by fringe pattern matching and a spatial phase-shifting interferometry (spatial PSI) algorithm. These two approaches are both theoretically described and experimentally illustrated in this thesis.

The method of phase difference determination by fringe pattern matching is capable of detecting the phase difference between two interferograms with subpixel resolution. In this method, the phase curves are obtained from mean-square-difference calculations of any two fringe patterns shifted pixel by pixel, and the phase difference between the interferograms can be achieved by linear interpolation or polynomial curve fitting from the phase curves. The signal to noise ratio is significantly improved due to the region-based matching and its effect of averaging noise. The equations derived from the statistical analysis of matching process clearly explain the reason that the larger image patches have a better accuracy in the measurement of phase difference. The three applications of fringe pattern matching, measurement of electrostatic force displacement, displacement measurement based on Young's experiment, and phase-shifting interferometry with arbitrary phase steps, are also investigated in this thesis. Computer simulation and experimental results have proved that fringe pattern matching is a powerful technique for measuring some basic parameters in optical interferometry such as phase difference, fringe spacing and displacement.

In the algorithm of spatial PSI, one fringe pattern is captured by a CCD camera, and the other two shifted fringe patterns with the phase steps of 90^{o} and 180^{o} are generated by computer, according to the features of the light intensity distributions and the method of interpolation. The phase is then calculated by a standard three-step algorithm of phase-shifting interferometry. Experimental results have shown that it is a useful approach to spatial PSI.

List of Publications

(1) Z. Wang, P.J. Bryanston-Cross, and K.C. Tong, "Application of LCD in Phase Stepping," *Proc. International Conference on Fringe Analysis*, York University, 66-70 (1994).

(2) Z. Wang and P.J. Bryanston-Cross, "An Algorithm of Spatial Phase-Shifting Interferometry," *Applied Optics & Optoelectronics*, Institute of Physics Publishing, Bristol, 280-285 (1996).

(3) Z. Wang, P.J. Bryanston-Cross, and D.J. Whitehouse, "Phase Difference Determination by Fringe Pattern Matching," *Optics & Laser Technology* **28**(6), 417-422 (1996).

(4) Z. Wang, M.S. Graça, P.J. Bryanston-Cross, and D.J. Whitehouse, "Phase-Shifted Image Matching Algorithm for Displacement Measurement," *Optical Engineering* **35**(8), 2327-2332 (1996).

(5) Z. Wang, P.J. Bryanston-Cross, and R.N. Davies, "Phase-Shifting Interferometry with Precise Phase Steps," *Proc. SPIE* **2775**, 452-459 (1996).

(6) Z. Wang, P.J. Bryanston-Cross and H. Long, "Displacement Measurement Based on Young's Experiment," *Proc. SPIE* **2782**, 786-793 (1996).

(7) Z. Wang, P.J. Bryanston-Cross, and D.J. Whitehouse, "Effect of Image Patch Size on Phase Difference Determination by Fringe Pattern Matching," *Optical Engineering* **36**(9), 2482-2488 (1997).

(8) Z. Wang, P.J. Bryanston-Cross, and D.T. Pham, "Two Methods for Achieving Sub-pixel Resolution in Phase Difference Determination by Fringe Pattern Matching," *Proc. SPIE* **3098**, 252-260 (1997).

(9) P.J. Bryanston-Cross and Z. Wang, "Camera Focusing Based on Fringe Pattern Matching," *Applied Optics* **36**(25), 6498-6502 (1997).

Contents

List of Tables

List of Figures

Chapter 1

Introduction

Optical interferometry is a technology that deals with the design and application of optical interferometers, as well as the study of interference patterns [1]. Optical interferometers, which are based on two-beam interference or multi-beam interference of light, have now become powerful tools for non-contact, non-destructive and high precision measurements in both laboratories and industry. In optical interferometry, the required information or physical quantity is normally encoded in the phase of interference or fringe patterns. A wide variety of measurements such as displacement, deformation, vibration and contour measurements of diffuse objects can be performed by optical interferometry with nanometer accuracy.

Optical interferometry has experienced a rapid development in recent years due to the advances in electronics and computer science. Today, almost all types of interferometer systems for high precision measurement are equipped with the advanced electronics devices such as the fast computers and charge-coupled devices (CCD). This means that the high precision measurement in optical interferometry is now both hardware and software based. As a result there has been a significant interests in the development of both. Optical interferometry has, in effect, become a multi-disciplinary technology employing optics, electronics and computer science for high precision measurement of many physical quantities.

In this thesis, two new approaches and their applications in optical interferometry are presented. Chapter 1 introduces some background knowledge of optical interferometry and relevant techniques which will be used in the following chapters. Chapter 2 presents a technique of phase difference determination by fringe pattern matching with subpixel resolution. The methods of linear interpolation and polynomial curve fitting for achieving subpixel resolution in phase difference measurement are introduced. The effects of image resolutions are also discussed based on computer simulation. Chapter 3 discusses the effect of image patch size on phase difference determination by fringe pattern matching. The standard deviation equations for fringe pattern matching are obtained from the statistical analysis of fringe pattern matching process and they clearly explain the reason that the larger image patches provide a more accurate measurement of phase difference by fringe pattern matching. Chapter 4 discusses the measurement of electrostatic force displacement by fringe pattern matching technique. The experimental result shows that the method is suitable for measurement in harsh environmental conditions. In chapter 5, a method of displacement measurement based on Young's experiment is described in detail. The method provides a possible way to measure displacement in a machine vision system. The method of phase-shifting interferometry with arbitrary phase steps is studied in chapter 6. Fringe pattern matching is proved to be an effective method for determining the phase steps directly from the interferograms without worrying about the phase shift errors in phase-shifting interferometry. Chapter 7 presents an algorithm of spatial phase-shifting interferometry. The method of interpolation is used for numerically shifting the fringes. The general conclusions and further research suggestions are given in chapter 8. In the section of further work, a new idea for determining phase differences in optical interferometry, which is a knowledge-based fitting, is presented and it is expected to achieve a better accuracy compared with fringe pattern matching.

1.1 Basic Principles of Optical Interference

The two principles of optical interference, interference of light and Young's experiment, are briefly introduced in this section. They are the basics of optical interferometry.

1.1.1 Interference of Light

The interference of light is the process by which two or more light waves of the same frequency or wavelength combine at a point in space to form a new light wave whose amplitude is the vector sum of the individual constituent disturbances. It may be considered as an interaction of two or more light waves and the result of the interaction obeys the principle of superposition [2].

The two-beam interference equation, which is often used in optical interferometry, can be derived from adding two light waves. Assume that two light waves of the same frequency are described by [3]

$$u_1 = U_1 e^{i\phi_1} \tag{1.1}$$

$$u_2 = U_2 e^{i\phi_2} \tag{1.2}$$

where U_1 and U_2 are the peak amplitudes. ϕ_1 and ϕ_2 are the initial phase angles. In equations 1.1 and 1.2, i is the imaginary unit ($i=\sqrt{-1}$). The sum of the two light waves is

$$u = u_1 + u_2 \tag{1.3}$$

The light intensity I, which is the observable quantity in the interference, can be written as

$$I = |u|^2 = U_1^2 + U_2^2 + 2U_1U_2\cos(\phi_1 - \phi_2) \tag{1.4}$$

where |u| is the magnitude of u and $(\phi_1 - \phi_2)$ is the phase difference between the two light waves. The expression $2U_1U_2\cos(\phi_1 - \phi_2)$ is known as the interference term.

Substituting I_{01} and I_{02} for U_1^2 and U_2^2, equation 1.4 can be rewritten as

$$I = I_{01} + I_{02} + 2\sqrt{I_{01}I_{02}}\cos(\phi_1 - \phi_2) \tag{1.5}$$

where I_{01} and I_{02} are the light intensities of u_1 and u_2, respectively. The interference term becomes $2\sqrt{I_{01}I_{02}}\cos(\phi_1 - \phi_2)$ in equation 1.5. At various points in space, the light intensity can be greater, less than, or equal to $I_{01} + I_{02}$, depending on the value of the interference term. $0 < \cos(\phi_1 - \phi_2) < 1$ is considered as the condition of constructive interference, and $-1 < \cos(\phi_1 - \phi_2) < 0$ is the condition of destructive interference. It can be seen that the light intensity I reaches its maximum I_{max}, that is

$$I = I_{01} + I_{02} + 2\sqrt{I_{01}I_{02}} \tag{1.6}$$

when

$$\phi_1 - \phi_2 = 2n\pi, \quad \text{for } n = 0, \pm1, \pm2, ... \tag{1.7}$$

and I reaches its minimum I_{min}, that is

$$I = I_{01} + I_{02} - 2\sqrt{I_{01}I_{02}} \tag{1.8}$$

when

$$\phi_1 - \phi_2 = (2n + 1)\pi, \quad \text{for } n = 0, \pm1, \pm2, ... \tag{1.9}$$

$\cos(\phi_1 - \phi_2) = 1$ means the two waves are in phase and it is referred to be total constructive interference. For $\cos(\phi_1 - \phi_2) = -1$, it is the case of 180^o out of phase and referred to be total destructive interference.

For two waves of equal intensity, i.e. $I_{01} = I_{02} = I_{00}$, equation 1.5 can be simplified

as

$$I = 2I_{00}[1 + \cos(\phi_1 - \phi_2)] \tag{1.10}$$

or

$$I = 4I_{00}\cos^2\frac{(\phi_1 - \phi_2)}{2} \tag{1.11}$$

where the intensity I varies between 0 and $4I_{00}$ with the phase difference $\phi_1 - \phi_2$.

1.1.2 Young's Experiment

The first experiment to observe the interference of light was made by Thomas Young in 1801 [4]. In the experiment as shown in figure 1.1, a narrow slit A is illuminated by a monochromatic light source of wavelength λ, and the light from slit A illuminates the two adjacent slits B and C which are separated by a distance d_0. The light waves from slits B and C interferes in space and the interference fringes can be seen on the screen which is a distance of D from the two slits.

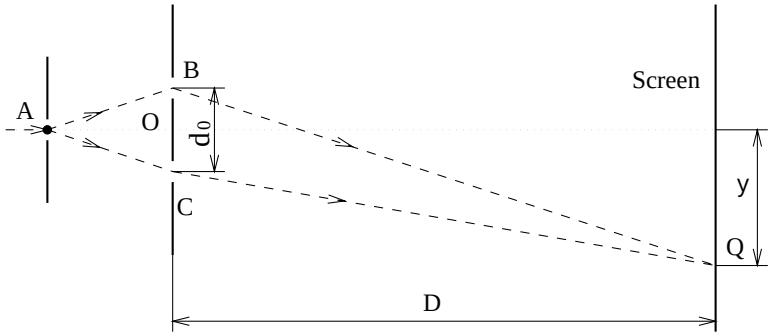

Figure 1.1: Young's experiment

In figure 1.1, the path difference of the two interfering beams from A to Q, ΔL, is

$$\Delta L = (AB + BQ) - (AC + CQ) \tag{1.12}$$

If slits B and C are symmetrical to the optical axis, i.e. AB=AC, the path difference ΔL can be expressed as

$$\Delta L = BQ - CQ \tag{1.13}$$

Assuming that point O is the origin of co-ordinates in figure 1.1, BQ and CQ can be calculated by

$$(BQ)^2 = D^2 + (y - \frac{d_0}{2})^2 \tag{1.14}$$

$$(CQ)^2 = D^2 + (y + \frac{d_0}{2})^2 \tag{1.15}$$

The difference of equations 1.14 and 1.15 is

$$(BQ)^2 - (CQ)^2 = (BQ + CQ)(BQ - CQ) = -2d_0y \tag{1.16}$$

or

$$\Delta L = BQ - CQ = \frac{-2d_0y}{BQ + CQ} \tag{1.17}$$

As a result of $D \gg d_0$, BQ+CQ$\approx$2D. Equation 1.17 is then simplified as

$$\Delta L = \frac{-d_0y}{D} \tag{1.18}$$

The phase difference at Q, $\Delta\phi$, can be computed by

$$\Delta\phi = \frac{2\pi\Delta L}{\lambda} = \frac{-2\pi d_0y}{D\lambda} \tag{1.19}$$

The maxima of light intensity, which are the bright bands, can be observed on the screen at the points where

$$y = \frac{m_0D\lambda}{d_0}, \quad (m_0 = 0, \pm1, \pm2, ...) \tag{1.20}$$

The minima of light intensity, which are the dark bands, can be observed at the points where

$$y = \frac{n_0 D\lambda}{d_0}, \quad (n_0 = \pm\frac{1}{2}, \pm\frac{3}{2}, \pm\frac{5}{2}, ...) \tag{1.21}$$

The fringe period or spacing P is the difference of two neighbouring maxima or minima of light intensity and it can be computed by

$$P = \frac{D\lambda}{d_0} \tag{1.22}$$

In fringe pattern analysis, equation 1.22 describes the basic relationship among the fringe period, wavelength, distance between the light source and screen, and distance between the two beams.

1.2 Phase-Shifting Interferometry

High accurate fringe pattern analysis is now based on phase-shifting interferometry (PSI) [5, 6, 7]. In phase-shifting interferometry, the physical quantity to be measured changes the optical path length, and the optical path difference gives rise to the interference pattern. A CCD camera is used to detect the intensity distribution of the interference pattern. The intensity distribution is read into computer and the phase can be determined numerically to a fraction of a degree.

The intensity distribution of the interference pattern I(x,y), which is from the interference of two light beams, can be described by

$$I(x, y) = a(x, y) + b(x, y)\cos[\phi(x, y) + \phi_r] \tag{1.23}$$

where a(x,y) and b(x,y) are background illumination and modulation terms respectively. The phase $\phi(x, y)$ is related to the quantity to be measured, and ϕ_r is a reference phase.

The types of phase-shifting interferometry are often identified according to the phase-shifting methods by which the phase steps are introduced. Basically, phase-shifting interferometry includes the techniques of temporal phase-shifting interferometry (temporal PSI) [8, 9, 10, 11, 12, 13], parallel phase-shifting interferometry (parallel PSI) [14], and spatial phase-shifting interferometry (spatial PSI or one-step method) [15, 16, 17, 18, 19]. Each of the techniques has its own advantages and disadvantages compared with others.

In this section, the three types of phase-shifting interferometry, temporal PSI, parallel PSI and spatial PSI are briefly described. The technique of phase unwrapping is also introduced as it is directly related to phase-shifting interferometry. In the last subsection, some errors in phase-shifting interferometry are discussed.

1.2.1 Temporal PSI

Temporal PSI, which captures a temporal sequence of interferograms with different phase shifts, has the advantages of high resolution and high accuracy of measurement. It is now the most widely used technique for high accurate fringe pattern analysis. In temporal PSI, the phase of the reference beam is made to vary in a known manner. This can be achieved, for example, by PZT (piezoelectric transducer) displacing a mirror.

From equation 1.23, it can be seen that at least three interference patterns with different reference phases are needed to find the phase $\phi(x, y)$ in temporal PSI. The most often used algorithms of temporal PSI include Carré [5, 8], three-step [9], four-step [10], five-step [11], and multi-step [12, 13] algorithms, which are mainly identified by the number of captured interferograms with different reference phases for the phase calculation.

1.2.1.1 Carré Algorithm

In Carré algorithm, the phase is shifted by a constant step of α between the captured interferograms, but the amount of phase shift is unknown. The phase steps are $-\frac{3\alpha}{2}$, $-\frac{\alpha}{2}$, $\frac{\alpha}{2}$, and $\frac{3\alpha}{2}$. The four light intensity distributions can be expressed as

$$\mathrm{I}_1(\mathrm{x},\mathrm{y}) = \mathrm{a}(\mathrm{x},\mathrm{y}) + \mathrm{b}(\mathrm{x},\mathrm{y})\cos[\phi(\mathrm{x},\mathrm{y}) - \frac{3\alpha}{2}] \tag{1.24}$$

$$\mathrm{I}_2(\mathrm{x},\mathrm{y}) = \mathrm{a}(\mathrm{x},\mathrm{y}) + \mathrm{b}(\mathrm{x},\mathrm{y})\cos[\phi(\mathrm{x},\mathrm{y}) - \frac{\alpha}{2}] \tag{1.25}$$

$$\mathrm{I}_3(\mathrm{x},\mathrm{y}) = \mathrm{a}(\mathrm{x},\mathrm{y}) + \mathrm{b}(\mathrm{x},\mathrm{y})\cos[\phi(\mathrm{x},\mathrm{y}) + \frac{\alpha}{2}] \tag{1.26}$$

$$\mathrm{I}_4(\mathrm{x},\mathrm{y}) = \mathrm{a}(\mathrm{x},\mathrm{y}) + \mathrm{b}(\mathrm{x},\mathrm{y})\cos[\phi(\mathrm{x},\mathrm{y}) + \frac{3\alpha}{2}] \tag{1.27}$$

where the phase shifts are assumed to be linear. From equations 1.24, 1.25, 1.26 and 1.27 the phase step α can be determined by

$$\alpha = 2\arctan\sqrt{\frac{3(\mathrm{I}_2 - \mathrm{I}_3) - (\mathrm{I}_1 - \mathrm{I}_4)}{(\mathrm{I}_2 - \mathrm{I}_3) + (\mathrm{I}_1 - \mathrm{I}_4)}} \tag{1.28}$$

The phase ϕ can be calculated by

$$\phi = \arctan\sqrt{\frac{[(\mathrm{I}_1 - \mathrm{I}_4) + (\mathrm{I}_2 - \mathrm{I}_3)][3(\mathrm{I}_2 - \mathrm{I}_3) - (\mathrm{I}_1 - \mathrm{I}_4)]}{(\mathrm{I}_2 + \mathrm{I}_3) - (\mathrm{I}_1 + \mathrm{I}_4)}} \tag{1.29}$$

It can be seen that the liner phase shifts are needed in Carré algorithm, and it has the advantage of achieving the phase without worrying about the error resulting from the phase shifter miscalibration.

1.2.1.2 Three-Step Algorithm

It is known that three recorded interferograms with different phase steps are basically needed to calculate the phase in the general equation of interference fringe pattern. There are many different expressions for three-step algorithm as the phase step is arbitrary. For the three recorded intensity distributions with

the phase shifts of α_1, α_2 and α_3, the equations are

$$\mathrm{I}_1(\mathrm{x},\mathrm{y}) = \mathrm{a}(\mathrm{x},\mathrm{y}) + \mathrm{b}(\mathrm{x},\mathrm{y})\cos[\phi(\mathrm{x},\mathrm{y}) + \alpha_1] \tag{1.30}$$

$$\mathrm{I}_2(\mathrm{x},\mathrm{y}) = \mathrm{a}(\mathrm{x},\mathrm{y}) + \mathrm{b}(\mathrm{x},\mathrm{y})\cos[\phi(\mathrm{x},\mathrm{y}) + \alpha_2] \tag{1.31}$$

$$\mathrm{I}_3(\mathrm{x},\mathrm{y}) = \mathrm{a}(\mathrm{x},\mathrm{y}) + \mathrm{b}(\mathrm{x},\mathrm{y})\cos[\phi(\mathrm{x},\mathrm{y}) + \alpha_3] \tag{1.32}$$

The phase ϕ can be computed by

$$\phi = \arctan\frac{(\mathrm{I}_3 - \mathrm{I}_1)(\cos\alpha_2 - \cos\alpha_1) - (\mathrm{I}_2 - \mathrm{I}_1)(\cos\alpha_3 - \cos\alpha_1)}{(\mathrm{I}_3 - \mathrm{I}_1)(\sin\alpha_2 - \sin\alpha_1) - (\mathrm{I}_2 - \mathrm{I}_1)(\sin\alpha_3 - \sin\alpha_1)} \tag{1.33}$$

This algorithm has the advantages of minimising the acquisition time and the memory space required for storing data. The disadvantage for this method is that it is most sensitive to the phase shift and intensity errors [20].

1.2.1.3 Four-Step Algorithm

In a case of four-step algorithm, the phase shifts are 0, $\frac{\pi}{2}$, π and $\frac{3\pi}{2}$. The four recorded fringe patterns can be written as

$$\mathrm{I}_1(\mathrm{x},\mathrm{y}) = \mathrm{a}(\mathrm{x},\mathrm{y}) + \mathrm{b}(\mathrm{x},\mathrm{y})\cos[\phi(\mathrm{x},\mathrm{y}) + 0] \tag{1.34}$$

$$\mathrm{I}_2(\mathrm{x},\mathrm{y}) = \mathrm{a}(\mathrm{x},\mathrm{y}) + \mathrm{b}(\mathrm{x},\mathrm{y})\cos[\phi(\mathrm{x},\mathrm{y}) + \frac{\pi}{2}] \tag{1.35}$$

$$\mathrm{I}_3(\mathrm{x},\mathrm{y}) = \mathrm{a}(\mathrm{x},\mathrm{y}) + \mathrm{b}(\mathrm{x},\mathrm{y})\cos[\phi(\mathrm{x},\mathrm{y}) + \pi] \tag{1.36}$$

$$\mathrm{I}_4(\mathrm{x},\mathrm{y}) = \mathrm{a}(\mathrm{x},\mathrm{y}) + \mathrm{b}(\mathrm{x},\mathrm{y})\cos[\phi(\mathrm{x},\mathrm{y}) + \frac{3\pi}{2}] \tag{1.37}$$

The phase ϕ can be calculated by

$$\phi = \arctan\frac{\mathrm{I}_4 - \mathrm{I}_2}{\mathrm{I}_1 - \mathrm{I}_3} \tag{1.38}$$

This algorithm increases the data acquisition time, but reduces the sensitivity to the phase shift errors [20].

1.2.1.4 Five-Step Algorithm

For a five-step algorithm with the phase shifts of $-\pi$, $-\frac{\pi}{2}$, 0, $\frac{\pi}{2}$ and π, the intensity distributions are

$$\mathrm{I_1(x,y) = a(x,y) + b(x,y)\cos[\phi(x,y) - \pi]} \tag{1.39}$$

$$\mathrm{I_2(x,y) = a(x,y) + b(x,y)\cos[\phi(x,y) - \frac{\pi}{2}]} \tag{1.40}$$

$$\mathrm{I_3(x,y) = a(x,y) + b(x,y)\cos[\phi(x,y) + 0]} \tag{1.41}$$

$$\mathrm{I_4(x,y) = a(x,y) + b(x,y)\cos[\phi(x,y) + \frac{\pi}{2}]} \tag{1.42}$$

$$\mathrm{I_5(x,y) = a(x,y) + b(x,y)\cos[\phi(x,y) + \pi]} \tag{1.43}$$

The phase ϕ can be calculated by

$$\phi = \arctan\frac{7(\mathrm{I_2 - I_4})}{-4\mathrm{I_1} + \mathrm{I_2} + 6\mathrm{I_3} + \mathrm{I_4} - 4\mathrm{I_5}} \tag{1.44}$$

This algorithm may get a high accuracy of phase measurement, but it needs more acquisition time and it may cause stronger influence of random environmental errors [20].

1.2.1.5 Multi-Step Algorithm

The multi-step algorithm uses the arbitrary number of equi-stepped interferograms to obtain the phase. The kth recorded intensity can be expressed as

$$\mathrm{I_k(x,y) = a(x,y) + b(x,y)\cos[\phi(x,y) - \phi_k]}, \quad \mathrm{k = 1, 2, 3, ..., N} \tag{1.45}$$

The phase ϕ can be computed by

$$\phi = \arctan\frac{\sum_{k=1}^{N} I_k \sin\phi_k}{\sum_{k=1}^{N} I_k \cos\phi_k} \tag{1.46}$$

where

$$\phi_k = \frac{2(k-1)\pi}{N}, \quad k = 1, 2, 3, ..., N \tag{1.47}$$

This is a general case of temporal PSI algorithm. Compared with five-step algorithm, multi-step algorithm uses more acquisition time for capturing the required number of equi-stepped interferograms in the calculation of phase.

1.2.2 Parallel PSI

Parallel PSI that allows phase measurement in vibration and dynamic environments is based on the acquisition of three or four phase shifted interferograms with three or four cameras simultaneously or in parallel. In a case of employing four cameras [14], the four phase shifted fringe patterns are given by

$$I_1(x, y) = a(x, y) + b(x, y)\cos\phi(x, y), \quad \text{for camera 1} \tag{1.48}$$

$$I_2(x, y) = a(x, y) - b(x, y)\sin\phi(x, y), \quad \text{for camera 2} \tag{1.49}$$

$$I_3(x, y) = a(x, y) - b(x, y)\cos\phi(x, y), \quad \text{for camera 3} \tag{1.50}$$

$$I_4(x, y) = a(x, y) + b(x, y)\sin\phi(x, y), \quad \text{for camera 4} \tag{1.51}$$

The phase ϕ can be then calculated by a standard formula of four-step PSI. This technique is useful for dynamic measurement, but the optical system is complicated, and it is very difficult to align the system.

1.2.3 Spatial PSI

Spatial PSI, which uses only one interferogram captured with a large number of tilt fringes to calculate the phase, is a relatively new technique for fringe pattern analysis. In spatial PSI, the phase shifted fringe patterns are obtained by special image processing techniques from one captured interferogram under some assumptions. This technique is therefore inherently free from the phase shift error which is a big problem in temporal PSI, and it is particularly appropriate for dynamic measurement. Several algorithms of spatial PSI such as four-pixel algorithm [15, 16, 17] and multi-pixel algorithm [18, 19] have been developed in recent years.

1.2.3.1 Four-Pixel Algorithm

In the four-pixel algorithm, one fringe period is adjusted on four pixels of an array detector so that the horizontal adjacent pixels record the fringe intensity distributions with a phase shift of $\frac{\pi}{2}$. The light intensity distributions can be therefore expressed as

$$I_1(x, y) = I(x, y) \tag{1.52}$$

$$I_2(x, y) = I(x + \frac{P}{4}, y) \tag{1.53}$$

$$I_3(x, y) = I(x + \frac{P}{2}, y) \tag{1.54}$$

where I(x,y) is the captured fringe pattern and the fringe period P is equal to four pixels. Since P=4 pixels equations 1.53 and 1.54 can be simplified as

$$I_2(x, y) = I(x + 1, y) \tag{1.55}$$

$$I_3(x, y) = I(x + 2, y) \tag{1.56}$$

It is clear that the fringe patterns $I_2(x, y)$ and $I_3(x, y)$ are here generated by computer. The phase ϕ can be then calculated by a formula of three-step PSI,

that is

$$\phi = \arctan\frac{I_3 - I_1}{I_2 - I_1} \tag{1.57}$$

This algorithm assumes that the objective phases change slowly over a 3/4 fringe period and that the fringe period is constant in the phase calculations.

1.2.3.2 Multi-Pixel Algorithm

For the multi-pixel algorithm, unlike the four-pixel algorithm of spatial PSI, the pixel number per fringe period is not fixed. In the algorithm, an interferogram with the size of N×N pixels, I(x,y), is split into three fringe patterns by computer. The three split fringe patterns are expressed as

$$I_1(m, n) = I[mP, n] \tag{1.58}$$

$$I_2(m, n) = I[\text{int}(\frac{P}{3}) + mP, n] \tag{1.59}$$

$$I_3(m, n) = I[\text{int}(\frac{2P}{3}) + mP, n] \tag{1.60}$$

where m=0, 1, 2, 3,..., int$[\frac{N-1-\text{int}(\frac{2P}{3})}{P}]$, n=0, 1, 2, 3,..., N-1. The function int(x) returns the integer value of x. The phase shift between the successive fringe patterns, β, is

$$\beta = \frac{2\pi}{P}\text{int}(\frac{P}{3}) \tag{1.61}$$

The phase can be then calculated by a standard formula of three-step PSI. In this algorithm, the objective phases are assumed to be constant over a fringe period range of $2/3 \sim 1$ and the fringe period is also assumed to be constant in the phase calculations. By comparison with the four-pixel algorithm, this algorithm has the advantage of using arbitrary number of pixels in one fringe period to acquire the phase-shifted interferograms. The disadvantage of this algorithm is that the fringe pattern size in the horizontal direction is reduced by a factor of about P of its original size.

1.2.4 Phase Unwrapping

The equations described above for phase calculations in phase-shifting interferometry can be generally expressed in the following form

$$\phi = \arctan(\frac{I_\alpha}{I_\beta}) \tag{1.62}$$

where I_α and I_β are the functions of the recorded light intensities. Equation 1.62 gives the principle phase values ranging from -π to π due to the feature of arctangent function, so that the phase distribution is wrapped and has 2π phase jumps. The result from the direct calculation of arctangent function is called wrapped phase.

The wrapped phase is a sawtooth-like function and the discontinuities occur when it changes by 2π. The discontinuities can be theoretically corrected by adding or subtracting 2π according to the direction of the phase jump and the result is called unwrapped phase. Phase unwrapping arises because the final step in fringe pattern analysis is to unwrap or integrate the phase along a line or path. 2π is added to the result when the phase jumps from π to -π and 2π is subtracted when the change is from -π to π. In practice, the phase jumps are not exactly equal to 2π due to the errors caused by imager resolutions and noise. The threshold $2k_u\pi$ ($k_u < 1$) is therefore used to detect the phase jumps.

Figures 1.2 and 1.3 show an example of phase unwrapping process. In figure 1.2, the 2π phase jumps occur at points 1, 3, 5 and 7. At point 1, the phase change is from π to -π so that 2π is added to the phase from point 2 to the end of the line. The same process as point 1 should be repeated at point 3. At point 5, the phase jump is from -π to π and 2π should be subtracted from the phase along the path from point 6 to the end of the line. In the same way, the unwrapping process should be repeated at point 7. The unwrapped phase obtained from the wrapped phase data in figure 1.2 is shown in figure 1.3. It is clear that the unwrapped

phase distribution is a continuos function.

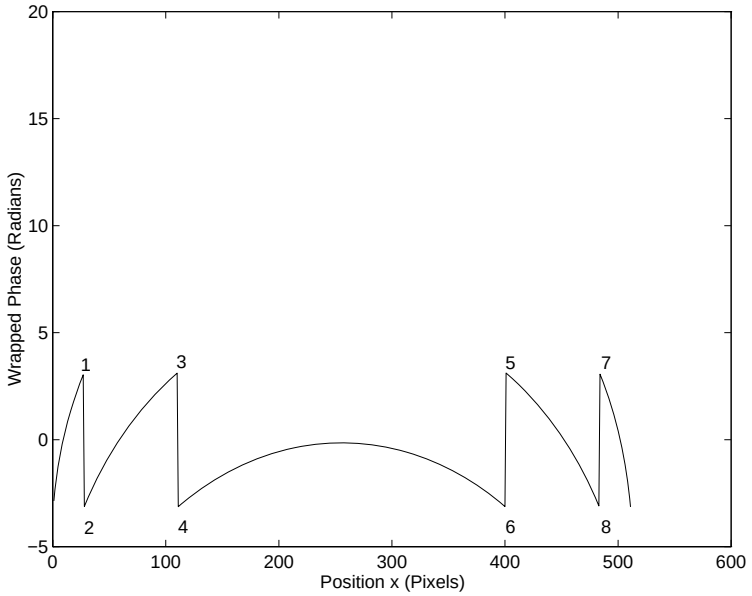

Figure 1.2: Wrapped phase distribution in one line

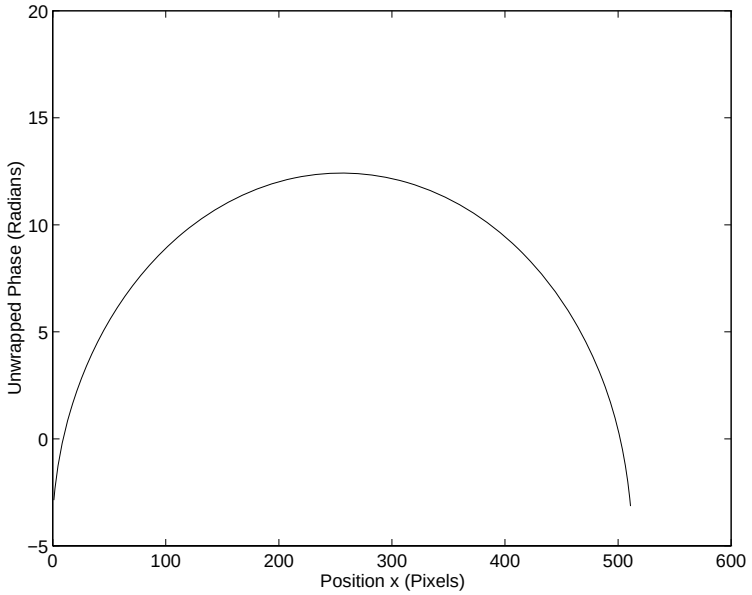

Figure 1.3: Unwrapped phase distribution obtained from the wrapped phase data

It can be seen that, for the noise-free phase data, phase unwrapping can be done by a sequential scan through the wrapped phase distribution and adding or subtracting 2π. In the phase unwrapping process, it is assumed that the light intensity is adequately sampled or, in other words, the phase gradient is significantly less than 2π between adjacent pixels. It should be noted that the phase data cannot be easily unwrapped in the presence of noise. The detailed discussion can be seen in the review by Judge and Bryanston-Cross [21].

1.2.5 Error Analysis in PSI

From the phase equations of PSI, the general phase equation may be written as

$$\phi = \arctan\frac{\sum_{k=1}^{N} c_{sk} I_k \sin\phi_k}{\sum_{k=1}^{N} c_{ck} I_k \cos\phi_k} \tag{1.63}$$

where c_{sk} and c_{ck} are constants. I_k is the kth recorded light intensity and ϕ_k is the kth introduced phase step.

It can be seen, from equation 1.63, that the accuracy of phase measurement can be degraded by the errors such as the phase shift error, intensity error, distortion error and sampling error. In this subsection, the four types of errors and their sources are briefly introduced.

1.2.5.1 Phase Shift Error

The phase shift error is a big problem in temporal PSI. The expected phase steps cannot be achieved in many cases due to the errors from the phase shifter, vibration, thermal drift and mechanical drift. For the real phase step ϕ'_k introduced in PSI, the general phase equation can be expressed as

$$\phi' = \arctan\frac{\sum_{k=1}^{N} c_{sk} I_k \sin\phi'_k}{\sum_{k=1}^{N} c_{ck} I_k \cos\phi'_k} \tag{1.64}$$

where

$$\phi'_{\mathrm{k}} = \phi_{\mathrm{k}} + \phi_{\mathrm{errork}}, \quad \mathrm{k} = 1, 2, 3, ..., \mathrm{N} \tag{1.65}$$

where ϕ_{errork} is the error which is added to the expected phase step ϕ_{k} in capturing the phase shifted fringe patterns.

The phase error $\Delta\phi$ can be evaluated by

$$\Delta\phi = \phi - \phi' \tag{1.66}$$

or

$$\Delta\phi = \arctan\frac{\sum_{\mathrm{k}=1}^{\mathrm{N}} \mathrm{c_{sk}} \mathrm{I_k} \sin\phi_{\mathrm{k}}}{\sum_{\mathrm{k}=1}^{\mathrm{N}} \mathrm{c_{ck}} \mathrm{I_k} \cos\phi_{\mathrm{k}}} - \arctan\frac{\sum_{\mathrm{k}=1}^{\mathrm{N}} \mathrm{c_{sk}} \mathrm{I_k} \sin\phi'_{\mathrm{k}}}{\sum_{\mathrm{k}=1}^{\mathrm{N}} \mathrm{c_{ck}} \mathrm{I_k} \cos\phi'_{\mathrm{k}}} \tag{1.67}$$

The sensitivities to the phase shift error vary with different algorithms. In recent years, great effort has been made to determine the phase shifts from the phase shifted fringe patterns to reduce the error or eliminate it [22, 23, 24, 25, 26, 27, 28].

1.2.5.2 Intensity Error

Intensity error changes the light intensity distributions of the phase shifted fringe patterns apart from their ideal values. This error is mainly from the intensity quantisation, nonlinearities of photosensitive cells and random intensity fluctuation in an imaging system for PSI.

It is known, from equation 1.63, that the phase is a function of the recorded light intensities. Therefore, the phase error caused by intensity error can be expressed by

$$\mathrm{d}\phi = \sum_{\mathrm{k}=1}^{\mathrm{N}} \frac{\partial\phi}{\partial \mathrm{I_k}} \mathrm{dI_k} \tag{1.68}$$

If the intensity differences are small, the phase error can be estimated by

$$\Delta\phi \approx \sum_{\mathrm{k}=1}^{\mathrm{N}} \frac{\partial\phi}{\partial \mathrm{I_k}} \Delta\mathrm{I_k} \tag{1.69}$$

The error from intensity quantisation or the rounding of the grey scale values to integer values [29] can be reduced by increasing the grey level resolution, and the error from imager nonlinearity may be decreased by calibration. In the case of random intensity fluctuation, averaging interferograms can reduce the intensity error [30].

1.2.5.3 Distortion Error

The distortion error is mainly from the non-ideal reference surface and aberrations in the optics of the PSI system. In a PSI system, each surface of optical components introduces aberrations as the beam passes through it. The interferograms with distortion are therefore obtained from the non-ideal reference surface and optical components. In this case, the PSI system has a departure from its ideal behaviour and it fails to obtain the objective phase without distortion.

The distortion error from the non-ideal reference surface and optical components can be reduced by careful calibration in experiments and correction in image processing [5, 31].

1.2.5.4 Sampling Error

A fringe pattern, which is recorded from an array of photo sensing elements, is stored in the form of a matrix in a computer. Image processing is therefore always related to matrix operations. This means that the object captured by camera is expressed by a sampled fringe pattern or matrix with a size of M×N picture elements or pixels.

In an imaging system, the sampling interval determines in a basic way whether all the information in the fringe pattern is represented. This can be explained by Nyquist sampling theorem that the underlying continuous fringe pattern is unambiguously represented by its samples if the fringe pattern contains no spatial

frequencies greater than one-half the sampling frequency [32].

Since the pixel number in a particular imaging system is fixed, the objective resolution is limited. The larger objects captured by the imaging system have a lower resolution in its dimensions and the sampling frequency is in effect decreased. There are two basic ways to reduce the sampling error. One is to increase the spatial resolution of the imaging system, which is limited by its cost and the size of a picture element. The other way is to use an image matching technique by which subpixel resolution can be expected. The technique of image matching will be introduced in the following section.

1.3 Image Matching

Image matching [32, 33, 34, 35, 36, 37, 38] is a technique which establishes an interpretation of images and the interpretation is the correspondence or similarity between a measured intensity distribution and its numerically generated equivalent in a computer. In this technique, two or more than two images are normally needed to obtain a high resolution of measurement or a whole view of 3-D (three-dimensional) object. Figure 1.4 illustrates an example of matching four images together to get a whole view of a large object with a high resolution.

There are two basic techniques of image matching, feature-based and region-based image matching. These two techniques are briefly introduced in the following two subsections.

1.3.1 Feature-Based Image Matching

In feature-based image matching, the image features such as points, edges and lines are extracted separately from the images using image processing techniques, and they are matched in a further step. This technique is less rigorously required

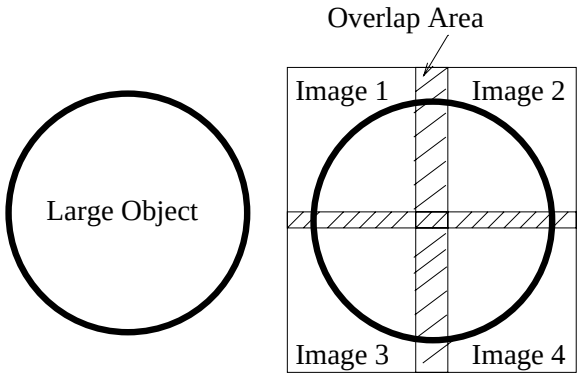

Figure 1.4: An example of image matching

in matching prediction, but it is not suitable for the matching with subpixel accuracy, compared with the region-based image matching.

1.3.2 Region-Based Image Matching

Unlike feature-based image matching, in region-based or area-based image matching, the image intensity values of different images are matched directly. The region-based image matching is a useful technique to find similar structures in two corresponding image patches, the reference image patch and a search image patch. The search image patch is transferred upon the reference image patch such that the squared sum of grey level differences is minimised.

Assuming that the input is a pair of image patches, the reference image patch E and the search image patch $E^{'}$, the output of 'mismatch' between the neighbourhood Q surrounding each pixel (x,y) in the first image E and a similar neighbourhood in the second image $E^{'}$ displaced by an offset $(\Delta x, \Delta y)$ in the matching region can be expressed as [36]

$$m(x, y; \Delta x, \Delta y) = \sum_{ij \in Q} [E(x + i, y + j) - E'(x + \Delta x + i, y + \Delta y + j)]^2 \qquad (1.70)$$

where the i and j are integers.

It can be seen that the mismatch is zero when the shifted neighbourhood of the second image is perfectly correlated with the initial neighbourhood of the first image. In practical applications, this technique can reach subpixel accuracy, but it is sensitive to image scale difference and relative rotation.

Bibliography

[1] C. Morris, *Academic Press Dictionary of Science and Technology*, Academic Press, London (1992).

[2] E. Hecht, *Optics*, Addison-Wesley Publishing Company, USA (1987).

[3] K.J. Gasvik, *Optical Metrology*, John Wiley & Sons, Chichester (1995).

[4] J. Sladkova, *Interference of Light*, Iliffe Books Ltd., London (1968).

[5] K. Creath, "Phase-measurement interferometry techniques," *Prog. Opt.* **26**, 349-393 (1988).

[6] D. Shough, "Beyond fringe analysis," *Proc. SPIE* **2003**, 208-223 (1993).

[7] C. Joenathan, "Phase-measuring interferometry : new methods and error analysis," *Appl. Opt.* **33** (19), 4147-4155 (1994).

[8] P. Carré, "Installation et utilisation du comparateur photoélectrique et interférential du Bureau International des Poids et Measures," *Metrologia* **2**, 13-23 (1966).

[9] J.C. Wyant, B.F. Oreb, and P. Hariharan, "Testing aspherics using two-wavelength holography : use of digital electronic techniques," *Appl. Opt.* **23** (22), 4020-4023 (1984).

[10] J.C. Wyant, "Use of an ac heterodyne lateral shear interferometer with real-time wavefront correction systems," *Appl. Opt.* **14** (11), 2622-2626 (1975).

[11] J. Schwider, R. Burow, K -E, Elssner, J. Grzanna, R. Spolaczyk, and K. Merkel, "Digital wave-front measuring interferometry : some systematic error sources," *Appl. Opt.* **22** (21), 3421-3432 (1983).

[12] J.H. Bruning, D.R. Herriott, J.E. Gallagher, D.P. Rosenfeld, A.D. White, and D.J. Brangaccio, "Digital wavefront measuring interferometer for testing optical surfaces and lenses," *Appl. Opt.* **13** (11), 2693-2703 (1974).

[13] J.E. Greivenkamp, "Generalized data reduction for heterodyne interferometry," *Opt. Eng.* **23** (4), 350-352 (1984).

[14] C.L. Koliopoulos and M. Jensen, "Real-time video rate phase processor," *Proc. SPIE* **2003**, 264-268 (1993).

[15] D.M. Shough, O.Y. Kwon, and D.F. Leary, "High-speed interferometric measurement of aerodynamic phenomena," *Proc. SPIE* **1221**, 394-403 (1990).

[16] M. Kujawińska and J. Wójciak, "Spatial-carrier phase shifting technique of fringe pattern analysis," *Proc. SPIE* **1508**, 61-67 (1991).

[17] R. Gu and T. Yoshizawa, "Talbot projected 3-D profilometry by means of one step phase-shift algorithms," *Proc. SPIE* **1720**, 470-477 (1992).

[18] P.H. Chan, P.J. Bryanston-Cross, and S.C. Parker, "Spatial phase stepping method of fringe pattern analysis," *Opt. Lasers Eng.* **23**, 343-354 (1995).

[19] P.H. Chan, P.J. Bryanston-Cross, and S.C. Parker, "Analysis of fringe pattern using a spatial phase stepping method with automatic phase unwrapping," *Meas. Sci. Technol.* **6**, 1250-1259 (1995).

[20] M. Kujawinska and K. Patorski, "New trends in optical methods for experimental mechanics. Part I: Moire and grating projection techniques for shape and deformation measurement," *Journal of Theoretical and Applied Mechanics* **31** (3), 539-561 (1993).

[21] T.R. Judge and P.J. Bryanston-Cross, "A review of phase unwrapping techniques in fringe analysis," *Opt. Lasers Eng.* **21** (4), 199-239 (1994).

[22] J. Schwider, "Phase shifting interferometry: reference phase error reduction," *Appl. Opt.* **28** (18), 3889-3892 (1989).

[23] K. Kinnstaetter, A.W. Lohmann, J. Schwider, and N. Streibl, "Accuracy of phase shifting interferometry," *Appl. Opt.* **27**(24), 5082-5089 (1988).

[24] G. Lai and T. Yatagai, "Generalized phase-shifting interferometry," *J. Opt. Soc. Am. A* **8**, 822-827 (1991).

[25] C.T. Farrell and M.A. Player, "Phase step measurement and variable step algorithms in phase-shifting interferometry," *Meas. Sci. Technol.* **3**, 953-958 (1992).

[26] C.T. Farrell and M.A. Player, "Phase-step insensitive algorithms for phase-shifting interferometry," *Meas. Sci. Technol.* **5**, 648-654 (1994).

[27] G.S. Han and S.W. Kim, "Numerical correction of reference phases in phase-shifting interferometry by iterative least-squares fitting," *Appl. Opt.* **33** (31), 7321-7325 (1994).

[28] I.B. Kong and S.W. Kim, "General algorithm of phase-shifting Interferometry by iterative least-squares fitting," *Opt. Eng.* **34** (1), 183-188 (1995).

[29] L.J. Galbiati, *Machine vision and digital image processing fundamentals*, Prentice-Hall, Englewood Cliffs, New Jersey and London (1990).

[30] K.R. Castleman, *Digital image processing,* Prentice-Hall, Englewood Cliffs and London (1979).

[31] T.R. Judge, C. Quan, and P.J. Bryanston-Cross, "Holographic Deformation Measurements by Fourier Transform Technique with Automatic Phase Unwrapping", *Opt. Eng.* **31** (3), 533-543 (1992).

[32] D.H. Ballard and C.M. Brown, *Computer vision*, Prentice-Hall, Englewood Cliffs, New Jersey (1982).

[33] M. James, *Pattern recognition*, BSP Professional Books, Oxford (1987).

[34] L. Chen, L. Lee, and J. Hsia, "Automated relative orientation modelling using feature matching," *Proc. SPIE* **1395**, 932-939 (1990).

[35] A. Goshtasby, G.C. Stockman, and C.V. Page, "A region-based approach to digital image registration with subpixel accuracy," *IEEE Trans. Geoscience and Remote Sensing* **GE-24** (3), 390-399 (1986).

[36] A. Kashko, H. Buxton, B.F. Buxton, and D.A. Castelow, 'Parallel matching and reconstruction algorithms in computer vision," *Parallel Computing* **8** (1-3), 3-17 (1988).

[37] G. He and K. Novak, "On line data capture by image matching on the mobile mapping system," *Proc. SPIE* **1820**, 50-56 (1992).

[38] A. Gruen and D. Stallmann, "High-accuracy matching of object edges', *Proc. SPIE* **1820**, 70-82 (1992).

Chapter 2

Phase Difference Determination by Fringe Pattern Matching

2.1 Introduction

The determination of phase difference in optical interferometry is directly related to the physical quantity to be measured. Many techniques [1] such as fringe counting [2, 3, 4], heterodyning [5, 6, 7, 8] and homodyning [9, 10, 11] interferometry have been developed in this field for precision phase difference measurement. Each of the techniques has its own fundamental features in accuracy, range of measurement, and the type of object that can be measured. It has been found that the conventional techniques have a common feature of using only a small part of the fringe pattern to achieve the information of phase difference, and their accuracies are easily affected by the non-ideal fringe patterns with background noise levels.

In this chapter, fringe pattern matching, which is a region-based image matching [12, 13, 14, 15], is used to determine the phase difference between two interferograms. A reference image patch in one interferogram, and a search or shifted image patch in the other with the same size as the reference image patch are

selected for the matching. The phase curves with the phase difference between the two interferograms are produced by shifting the image patches with respect to each other pixel by pixel, and at the same time calculating the mean-square-difference values for each shift. The phase difference can be decided from the matching point at which the mean-square-difference value is a minimum.

The method of phase difference determination by fringe pattern matching was examined in an experiment. The phase curves were obtained from different sizes of image patches of captured interferograms. The signal to noise ratio of the captured interferograms was significantly improved by fringe pattern matching, and an accuracy of 1.2^o was achieved from 100×252 pixel image patches of the interferograms using the matching together with linear interpolation.

In section 2.2, the principle of fringe pattern matching for phase difference measurement is described. Section 2.3 introduces two useful methods of achieving subpixel resolution, linear interpolation and polynomial curve fitting. The experimental results are illustrated in section 2.4. Section 2.5 discusses the effect of imager resolutions based on computer simulation. The discussion and conclusion of this chapter are given in sections 2.6 and 2.7 respectively.

2.2 Principle

In optical interferometry, the intensity distribution of the nth fringe pattern to be recorded $\mathrm{I_n(x,y)}$, which is from the interference of two light beams as introduced in chapter 1, can be expressed as

$$\mathrm{I_n(x,y)} = \mathrm{a(x,y)} + \mathrm{b(x,y)}\cos\phi_{\mathrm{n}}(\mathrm{x,y}), \quad \mathrm{n} = 0,1,2,... \tag{2.1}$$

where a(x,y) is the background illumination and b(x,y) is the modulation of the fringes. The phase $\phi_{\mathrm{n}}(\mathrm{x,y})$ is normally related to the physical quantity to be

measured.

It is known that any two fringe patterns with the same fringe spacing, which are shifted in sequence in an experiment, contain the information of phase difference in optical path, but it is often difficult to measure the phase difference directly from the two interferograms to achieve high resolution because of the presence of optical and electrical noise. Choosing a fixed image patch in the first fringe pattern as a reference image patch, shifting the image patch in the second fringe pattern back step by step, and at the same time calculating the mean-square-difference values for each shift in the computer can find the real shift distance from the matching point at which the mean-square-difference value is a minimum, and the shift distance represents the phase difference between the two fringe patterns. Figure 2.1 illustrates the principle of fringe pattern matching for determining the phase difference between the fringe patterns.

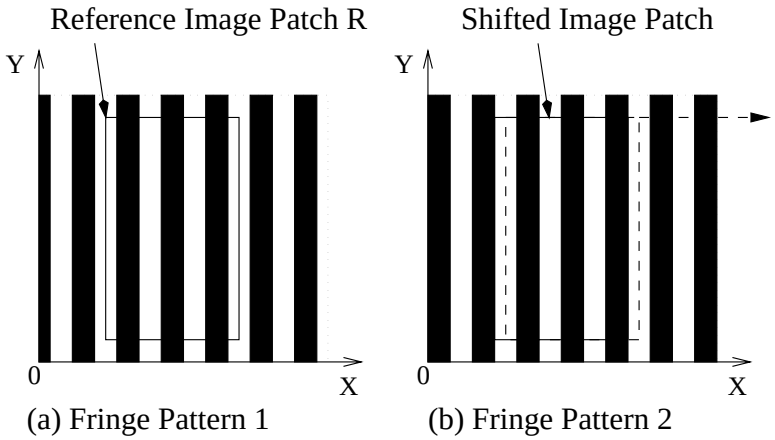

Figure 2.1: Principle of matching two fringe patterns

In figure 2.1, the reference image patch in fringe pattern 1 is fixed in the matching, and the image patch in fringe pattern 2 with the same area as the reference image patch is shifted step by step to find the matching point from the calculations of mean-square-difference. The phase curves with the phase difference between the fringe patterns can also be produced by the calculations.

Assuming that the fringes are vertical in the fringe patterns, the mismatch function $f_n(t)$ can be written as [13]

$$f_n(t) = \frac{1}{A}\int\int_R [I_0(x,y) - I_n(x \pm t, y)]^2 dxdy, \quad n = 0, 1, 2, ... \tag{2.2}$$

where t is the shifted distance that depends on the phase difference between the fringe patterns and the phase curves required for the calculation of the phase difference, R is the region of the reference image patch, and A is the area of the region R. The sign before t defines the fringe shifting direction. For the fringes shifted in the left direction the mismatch function $f_n(t)$ is

$$f_n(t) = \frac{1}{A}\int\int_R [I_0(x,y) - I_n(x - t, y)]^2 dxdy, \quad n = 0, 1, 2, ... \tag{2.3}$$

and for the fringes shifted in the right direction the mismatch function $f_n(t)$ is

$$f_n(t) = \frac{1}{A}\int\int_R [I_0(x,y) - I_n(x + t, y)]^2 dxdy, \quad n = 0, 1, 2, ... \tag{2.4}$$

Equations 2.2, 2.3 and 2.4 are the general expressions for the continuous light intensity distributions of interference fringe patterns. In theory, the phase difference between two fringe patterns can be found from the mismatch functions without any error if the fringe patterns are ideal and their intensity distributions are continuous. From equation 1.10 and the discussion of Young's experiment in chapter 1, the light intensity distributions of the ideal fringe patterns can be expressed as

$$I_0(x,y) = I'_0[1 + \cos(\frac{2\pi}{P}x)] \tag{2.5}$$

$$I_n(x \pm t, y) = I'_0\{1 + \cos[\frac{2\pi}{P}(x \pm t) - \alpha_n]\} \tag{2.6}$$

where I'_0 is the light intensity of the two interference beams, P is the fringe period, and α_n is the phase difference between fringe patterns $I_0(x,y)$ and $I_n(x,y)$.

Substituting equations 2.5 and 2.6 into equation 2.2 can find the mismatch func-

tion in the form

$$f_n(t) = I'^2_0[1 - \cos(\pm\frac{2\pi}{P}t - \alpha_n)] \tag{2.7}$$

It is now clear, from equation 2.7, that fringe pattern matching is theoretically right for the determination of phase difference without any error.

In the above, the light intensity distributions are continuous. For the sampled light intensity distributions that are captured by the CCD camera, the equations can be written as

$$f_n(t) = k_0 \sum_{(i,j)\in R} [I_0(i,j) - I_n(i \pm t, j)]^2, \quad n = 0, 1, 2, ... \tag{2.8}$$

$$f_n(t) = k_0 \sum_{(i,j)\in R} [I_0(i,j) - I_n(i - t, j)]^2, \quad n = 0, 1, 2, ... \tag{2.9}$$

$$f_n(t) = k_0 \sum_{(i,j)\in R} [I_0(i,j) - I_n(i + t, j)]^2, \quad n = 0, 1, 2, ... \tag{2.10}$$

where k_0 is the inverse of the element number in the calculations. i and j are integers in equations 2.8, 2.9 and 2.10.

In figure 2.1, the two ideal fringe patterns have a phase shift of 90^o, and a fringe period of 40 pixels. The fringes are shifted in the right direction, so that the mismatch functions are

$$f_0(t) = k_0 \sum_{(i,j)\in R} [I_0(i,j) - I_0(i + t, j)]^2 \tag{2.11}$$

$$f_1(t) = k_0 \sum_{(i,j)\in R} [I_0(i,j) - I_1(i + t, j)]^2 \tag{2.12}$$

where $I_0(i,j)$ is the light intensity distribution of fringe pattern 1, and $I_1(i,j)$ is the light intensity distribution of fringe pattern 2. The phase curves calculated from equations 2.11 and 2.12 are shown in figure 2.2. The computer can find the phase values from the phase curves without difficulty. The accuracy is not influenced by the size of the image patch used in the matching for the ideal fringe

patterns.

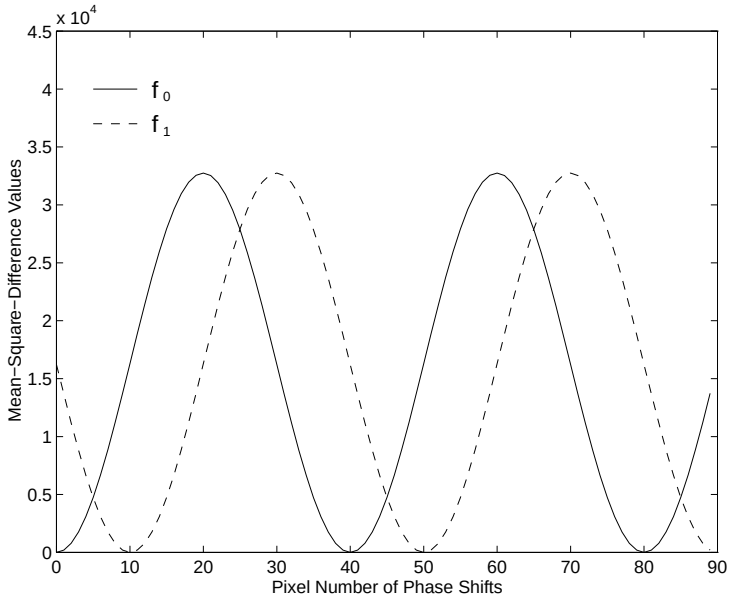

Figure 2.2: Phase curves of the two ideal fringe patterns with a phase shift of 90°

2.3 Methods for Achieving Subpixel Resolution

The exact phase difference can be theoretically determined by detecting the minimum of the mismatch function or the peak points from the phase curves. In practice, however, it is difficult, or impossible to find the minimum or peak points with subpixel resolution from the direct fringe pattern matching due to the resolution of the imaging sensor and the presence of noise. In this case, the methods of linear interpolation and polynomial curve fitting can be used to achieve subpixel resolution from the phase curves.

2.3.1 Linear Interpolation

Figure 2.3 shows the phase curves for calculating phase differences between two fringe patterns by linear interpolation.

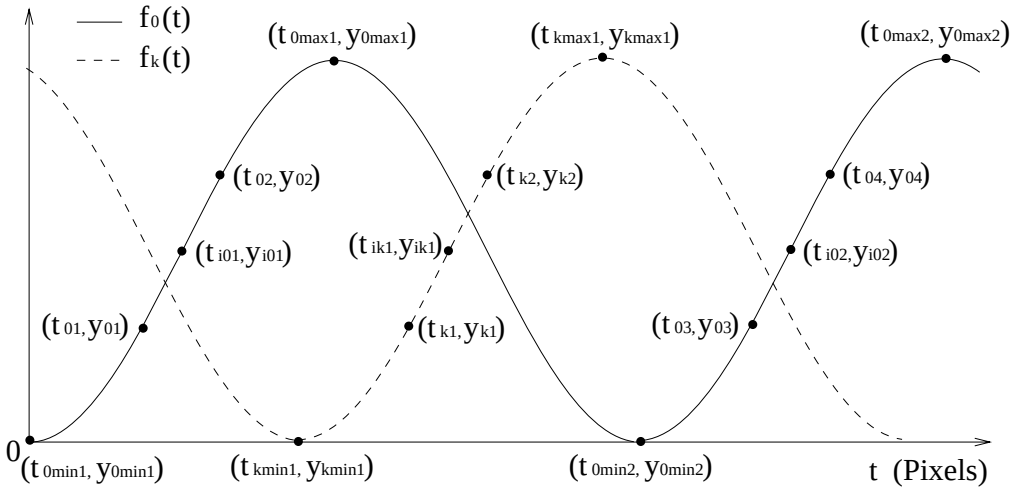

Figure 2.3: Phase curves for calculating phase differences

As shown in figure 2.3, the co-ordinates (t_{0max1}, y_{0max1}), (t_{kmax1}, y_{kmax1}) and (t_{0max2}, y_{0max2}) are the peak points, and (t_{0min1}, y_{0min1}), (t_{kmin1}, y_{kmin1}) and (t_{0min2}, y_{0min2}) are the valley points. The matching point of $f_0(t)$ is located at the origin of co-ordinates, so that $t_{0min1}=0$ and $y_{0min1}=0$. The matching point of $f_k(t)$ is at location (t_{kmin1}, y_{kmin1}). In practice, y_{kmin1} and y_{0min2} may not be zero for non-ideal fringe patterns. The co-ordinates (t_{i01}, y_{i01}), (t_{ik1}, y_{ik1}) and (t_{i02}, y_{i02}) are the interpolation points, and (t_{01}, y_{01}), (t_{02}, y_{02}), (t_{k1}, y_{k1}), (t_{k2}, y_{k2}), (t_{03}, y_{03}), and (t_{04}, y_{04}) are the nearest neighbours on the left and right sides of the interpolation points. The phase shifts t_{01}, t_{02}, t_{k1}, t_{k2}, t_{03} and t_{04} are integers. In this method, the interpolation points are selected within the regions where the phase curves have a better linearity and $\frac{\Delta f_n(t)}{\Delta t}$ reaches its maximum. These two features are useful in the determination of phase difference for achieving subpixel resolution.

The mismatch function is a cosinusoidal function of the phase shift number t, so that its peak and valley points can be determined by detecting the sign change of $\frac{\Delta f_n(t)}{\Delta t}$. Let the mismatch function $f_n(t)$ be a linear function on $[t_{01} t_{02}]$, $[t_{03}\ t_{04}]$ and $[t_{k1} t_{k2}]$. The interpolated co-ordinates as shown in figure 2.3 can be calculated using

$$y_{i01} = \frac{y_{0max1}}{2} \tag{2.13}$$

$$y_{ik1} = \frac{y_{kmax1} + y_{kmin1}}{2}, \quad k = 1, 2, 3, ... \tag{2.14}$$

$$y_{i02} = \frac{y_{0max2} + y_{0min2}}{2} \tag{2.15}$$

$$t_{i01} = \frac{y_{i01} - y_{01}}{y_{02} - y_{01}}(t_{02} - t_{01}) + t_{01} \tag{2.16}$$

$$t_{ik1} = \frac{y_{ik1} - y_{k1}}{y_{k2} - y_{k1}}(t_{k2} - t_{k1}) + t_{k1}, \quad k = 1, 2, 3, ... \tag{2.17}$$

$$t_{i02} = \frac{y_{i02} - y_{03}}{y_{04} - y_{03}}(t_{04} - t_{03}) + t_{03} \tag{2.18}$$

In the calculations of interpolating values, $t_{02} - t_{01}$=1, $t_{04} - t_{03}$=1 and $t_{k2} - t_{k1}$=1 as the interpolation points are always located between two neighbouring pixels. Therefore, the equations 2.16, 2.17 and 2.18 can be simplified as

$$t_{i01} = \frac{y_{i01} - y_{01}}{y_{02} - y_{01}} + t_{01} \tag{2.19}$$

$$t_{ik1} = \frac{y_{ik1} - y_{k1}}{y_{k2} - y_{k1}} + t_{k1}, \quad k = 1, 2, 3, ... \tag{2.20}$$

$$t_{i02} = \frac{y_{i02} - y_{03}}{y_{04} - y_{03}} + t_{03} \tag{2.21}$$

The fringe spacing P, the phase shift t_{kmin1} and the phase difference between the reference fringe pattern and the kth fringe pattern $\Delta\phi_k$ can be then determined by

$$P = t_{i02} - t_{i01} \tag{2.22}$$

$$t_{kmin1} = t_{ik1} - t_{i01}, \quad k = 1, 2, 3, ... \tag{2.23}$$

$$\Delta\phi_k = \frac{t_{kmin1}}{P} \times 360^o, \quad k = 1, 2, 3, ... \tag{2.24}$$

In the above, the phase changes are assumed in one fringe spacing. For the measurement of the phase difference greater than one fringe spacing, the periodic constant must be added in the measurement. In addition, the method of phase difference determination by fringe pattern matching is also valid for the fringe patterns in which the fringes are horizontal, oblique or curved, but the fringe spacing obtained from equation 2.22 is not the actual one in the case of oblique or curved fringes if the measurement is carried out in the horizontal or vertical directions.

2.3.2 Polynomial Curve Fitting

Figure 2.4 shows an ideal phase curve obtained from mean-square-difference calculations of an ideal fringe pattern. In figure 2.4, the fringe period P, for example, can be easily determined from the direct matching process with a resolution of one pixel, but it cannot find P with subpixel resolution from that. In this subsection, the method of polynomial curve fitting [16] is described to achieve subpixel resolution from the phase curve.

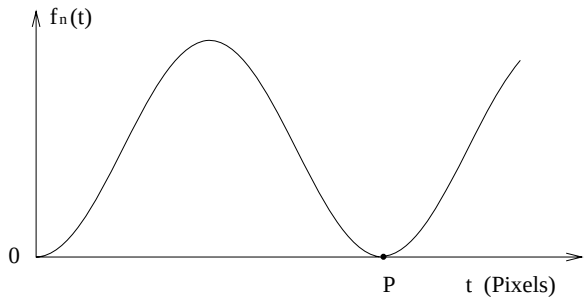

Figure 2.4: An ideal phase curve from mean-square-difference calculations

The method of polynomial curve fitting can provide an mth-order polynomial

$g_n(x)$ in the form

$$g_n(x) = \sum_{k=0}^{m} c_{nk} x^k, \quad n = 0, 1, 2, ... \tag{2.25}$$

where $g_n(x)$ is a function of the variable x and c_{nk} is a coefficient.

In a least-squares sense, the values of the coefficients in equation 2.25 can be obtained by setting the following m+1 partial derivatives to zero

$$\frac{\partial}{\partial c_{nk}} \{\sum_{t=0}^{N_t} [f_n(t) - g_n(t)]^2\} = 0, \quad k = 0, 1, 2, ..., m; \; n = 0, 1, 2, ... \tag{2.26}$$

where N_t is the shifted pixel number in the calculations of mean-square-difference, and it must be larger than the fringe spacing in this method. If $m \leq N_t$ there is a unique polynomial $g_n(x)$ for which the sum of squared deviations is minimised [16, 17]. In general, fit orders of about 10 are usually practical. Note that higher-order polynomial fits do not always converge to the input data since the fitting process is not numerically stable for high fit orders in many cases.

The maximums and minimums of the polynomial $g_n(x)$ are at the peak and valley points of the phase curve in a least-squares sense. Therefore, the fringe spacing P can be found by setting the derivative of the polynomial $g_n(x)$ to zero, that is

$$\frac{dg_n(x)}{dx} = 0, \quad n = 0, 1, 2, ... \tag{2.27}$$

The polynomial roots, which are obtained from equation 2.27, contain the values of the variable x at the peak and valley points of the phase curve, and the phase shifts t_{kmin1} and t_{0min2} in figure 2.3 are two of the roots. Therefore, the fringe spacing P can be computed by

$$P = t_{0min2} \tag{2.28}$$

and the phase difference between the reference fringe pattern and the kth fringe pattern $\Delta\phi_k$ can be calculated by equation 2.24.

2.3.3 Comparison between Linear Interpolation and Polynomial Curve Fitting

The interpolation values of phase differences can be theoretically achieved by the methods of linear interpolation and polynomial curve fitting, but the calculation of polynomial curve fitting is mathematically more complicated than that of linear interpolation in the determination of phase difference. Therefore, linear interpolation is useful for dynamic measurement as its calculation is very simple and needs less time.

In addition, it can be seen in the computer simulation in section 2.5 that with the method of linear interpolation it is easier to achieve a better accuracy compared with polynomial curve fitting.

2.4 Experimentation

The method of phase difference determination by fringe pattern matching was examined in the interferometer system for introducing phase shifts shown in figure 2.5. A phase shift of 90^o between fringe patterns was given by PZT(piezo-electric transducer) displacing a mirror. The PZT had a resolution of 1 nm and the wavelength of the He-Ne laser, employed in the experiment, was 0.6328 μm.

Two interferograms, captured in sequence by a CCD camera in the experiment, are shown in figure 2.6. The interferograms are 8-bit grey-level images with the size of 512×512 pixels. Figure 2.7 shows the light intensity distributions of the interferograms in row 255. The phase curves obtained from different sizes of image patches are shown in figure 2.8. Figure 2.8(a) shows the phase curves computed from the image patches with 1×252 pixels, and figure 2.8(b) shows the phase curves from the image patches with 100×252 pixels. The phase curves shown in figure 2.8 have a clear picture of phase differences between the two interferograms

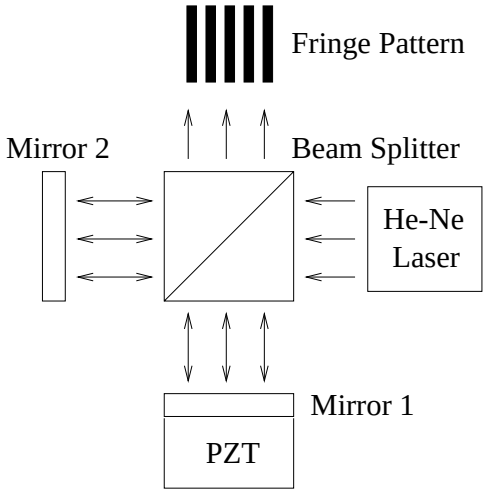

Figure 2.5: Schematic of the interferometer system

although the noise can be seen clearly from the intensity distributions in figure 2.7. The phase difference in figure 2.8(a), achieved by linear interpolation, is 92.5^o, and the phase difference in figure 2.8(b) is 91.2^o. The flow chart of MATLAB software for phase difference determination by fringe pattern matching is shown in figure 2.9, and two examples of the MATLAB M-files for determining the phase difference between two fringe patterns are given in appendices A.1 and A.2.

In the experiment, each of the images used in the matching was obtained by averaging 10 interferograms to improve the quality of image. The reference and shifted image patches with the sizes of 1×252 and 100×252 pixels were used for the calculations of mean-square-difference to obtain the phase curves. The accuracy was better than 2.6^o for 1×252 pixel image patches, and 1.2^o for 100×252 pixel image patches.

It can be seen, from the experimental results, that the accuracy is affected by the size of the image patch for the captured interferograms. The larger image patches have achieved a better accuracy in the presence of noise.

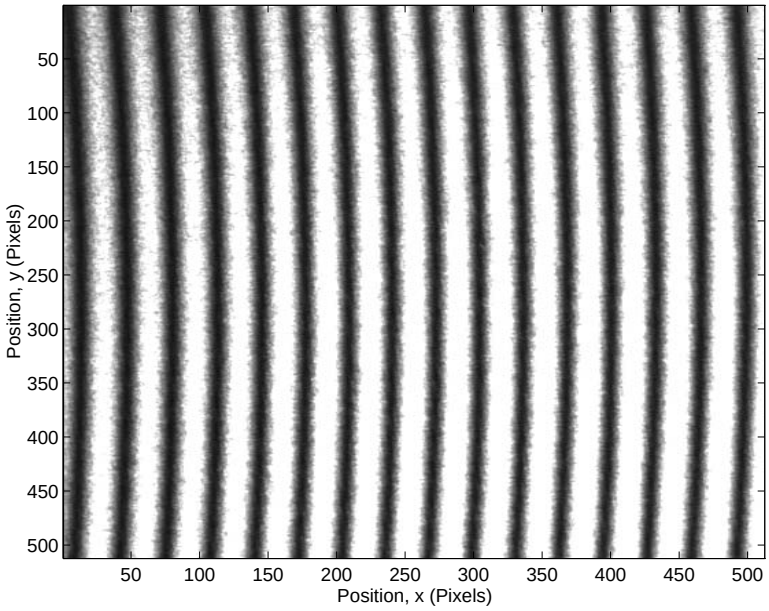

(a) Interferogram 1

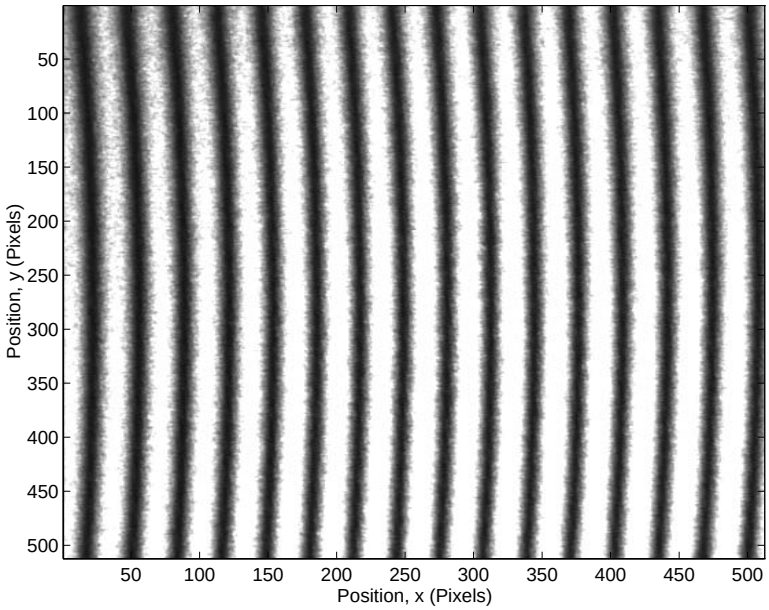

(b) Interferogram 2

Figure 2.6: Two interferograms captured by a CCD camera

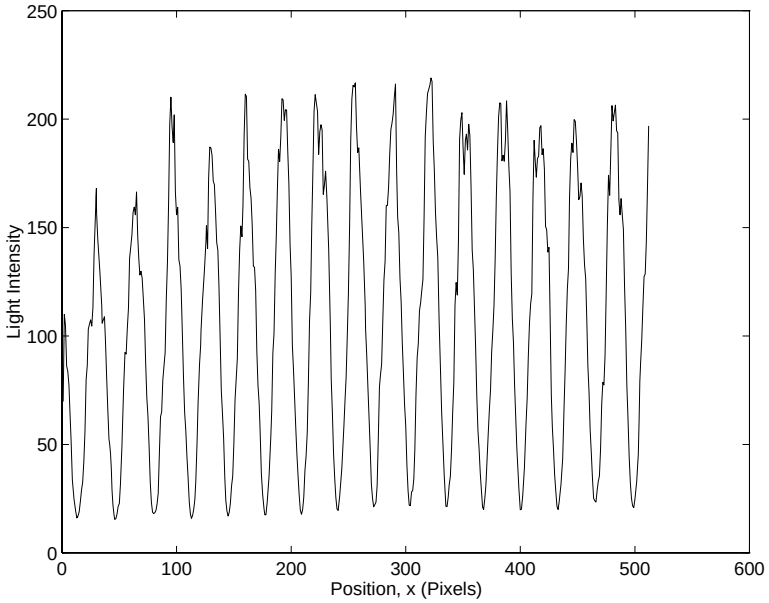

(a) Light intensity in row 255 of interferogram 1

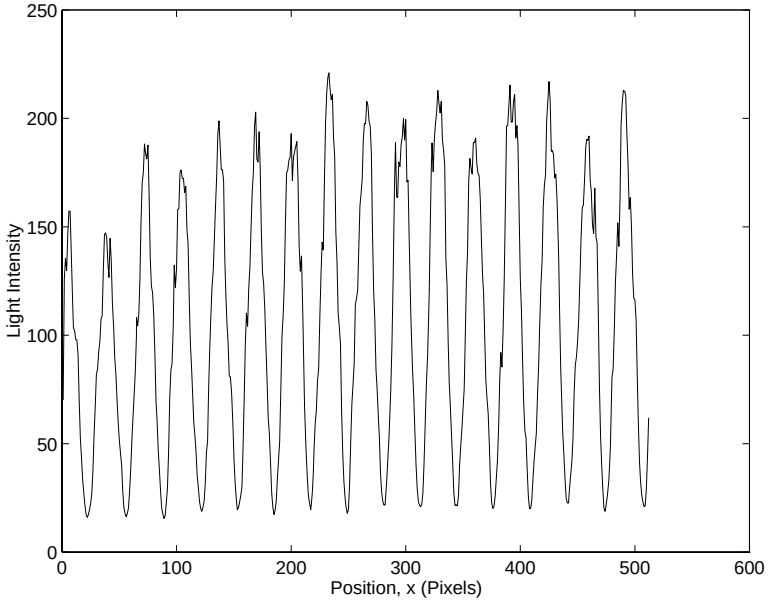

(b) Light intensity in row 255 of interferogram 2

Figure 2.7: Light intensity distributions in row 255 of the captured interferograms

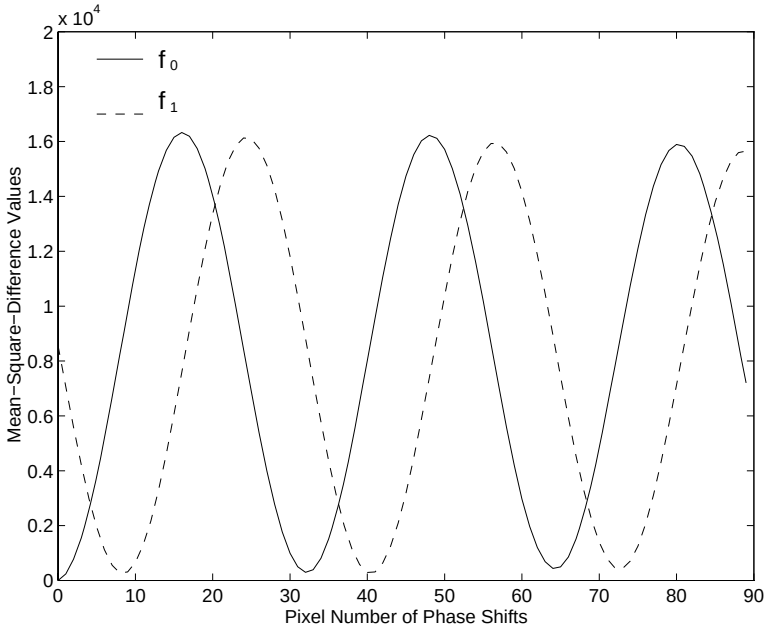

(a) Phase curves from the image patch of 1×252 pixels

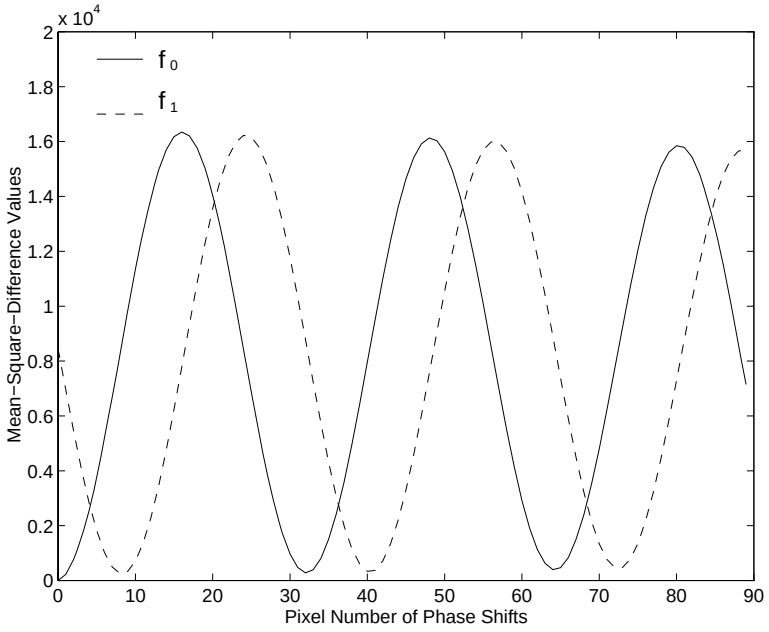

(b) Phase curves from the image patch of 100×252 pixels

Figure 2.8: Phase curves from different sizes of image patches of the two captured interferograms

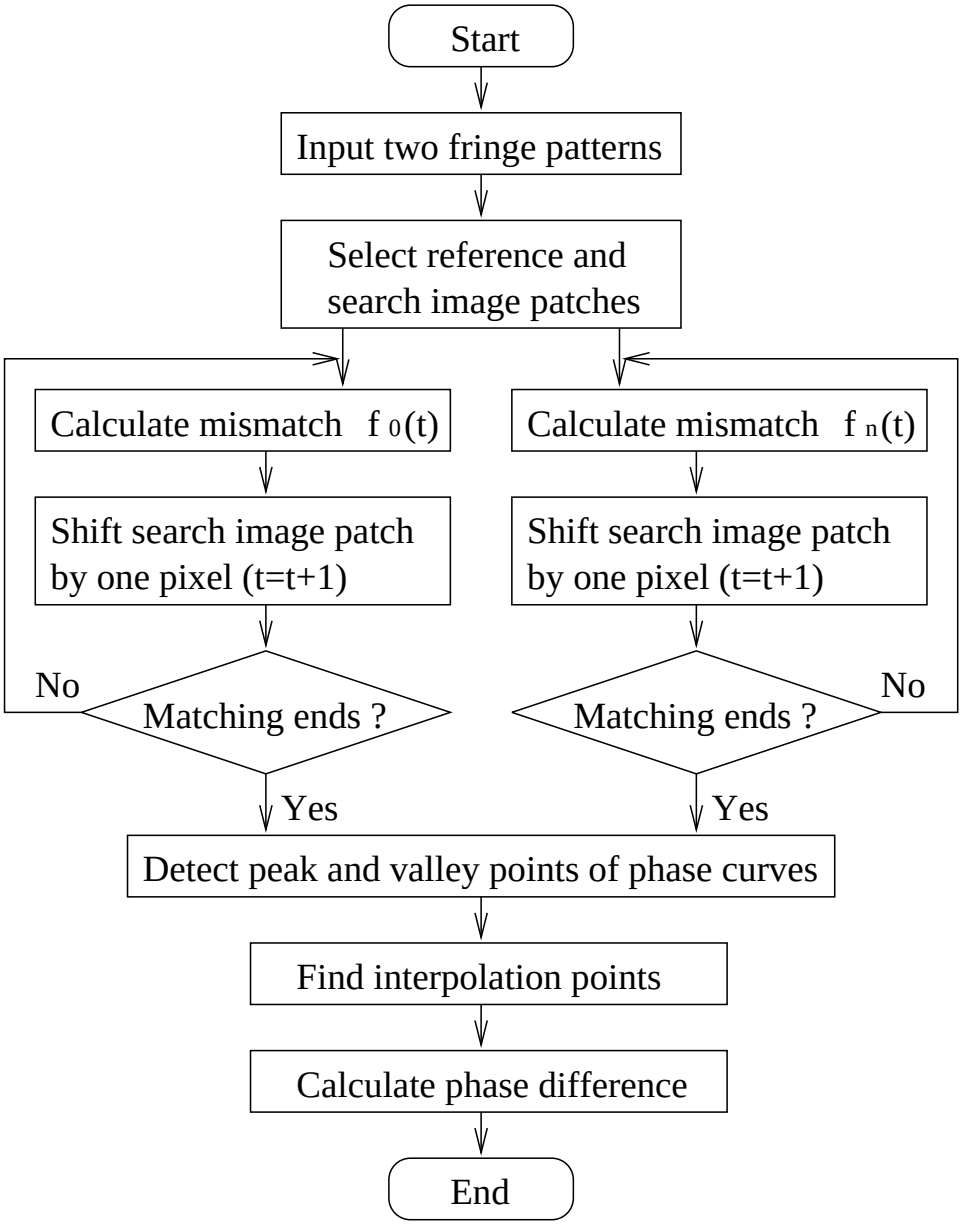

Figure 2.9: Flow chart of phase difference determination

2.5 Effect of Imager Resolutions

In order to be in a form suitable for computer processing, the fringe patterns are digitised both spatially and in amplitude. Digitisation of the spatial co-ordinates is referred to as fringe pattern sampling, while amplitude digitisation is called grey-level quantisation. Therefore, the quality of the digitised fringe pattern is dependent on both spatial resolution and grey-level resolution. In practice, the numbers of samples and grey levels are selected for a required approximation to a continuous fringe pattern. In this section, the errors of phase difference measurement due to the approximation are simulated by computer, and the methods of linear interpolation and polynomial curve fitting, as a comparison, are both used for the calculations of phase differences in the following two subsections.

2.5.1 Effect of Grey Level Resolution

The number of discrete grey levels for the measured light intensity distributions of fringe patterns is normally defined as the integer powers of two, which is a binary code obtained from an analogue to digital converter (ADC). In this subsection, the effect of grey level resolution on phase difference determination by fringe pattern matching is discussed based on computer simulation.

In the simulation, the fringe period was kept in constant with the pixel number of 40 and the fringe pattern size was 512×512 pixels. The intensity distribution was

$$\mathrm{I_n(i,j)} = \mathrm{round}[\frac{2^{\mathrm{K}}-1}{2} + \frac{2^{\mathrm{K}}-1}{2}\cos(\frac{\pi \mathrm{i}}{20} - \phi_{\mathrm{n}})], \quad \mathrm{n} = 0, 1, 2, ... \tag{2.29}$$

where i=0, 1, 2, ..., 511 and j=0, 1, 2, ..., 511. K is the bit number of discrete grey levels and ϕ_{n} (ϕ_0=0) is the phase shift. The function round(x) rounds x to the nearest integer to obtain the quantised fringe pattern.

Figure 2.10(a) shows the error curve of phase difference measurement made by linear interpolation for 8-bit grey-level fringe patterns, and the error curve by polynomial curve fitting is shown in figure 2.10(b). Figure 2.11 shows the computer simulation results from 10-bit grey-level fringe patterns, and the computer simulation results from 12-bit grey-level fringe patterns are shown as in figure 2.12. The computer simulation results of the effect of grey level resolution is given in table 2.1, and the MATLAB programme for the determination of phase difference by polynomial curve fitting is given in appendix A.3.

In the simulation, the maximum error of phase difference measurement made by linear interpolation for 8-bit grey levels was 0.0392^{o}, that for 10-bit grey levels was 0.0216^{o}, and that for 12-bit grey levels was 0.0051^{o}. As a result of comparison, the maximum error of phase difference measurement made by polynomial curve fitting for 8-bit grey levels was 0.0586^{o}, that for 10-bit grey levels was 0.0440^{o}, and that for 12-bit grey levels was 0.0180^{o}.

It can be seen, from the computer simulation results, that the higher grey-level resolution has obtained a better accuracy from both linear interpolation and polynomial curve fitting in the determination of phase difference by fringe pattern matching.

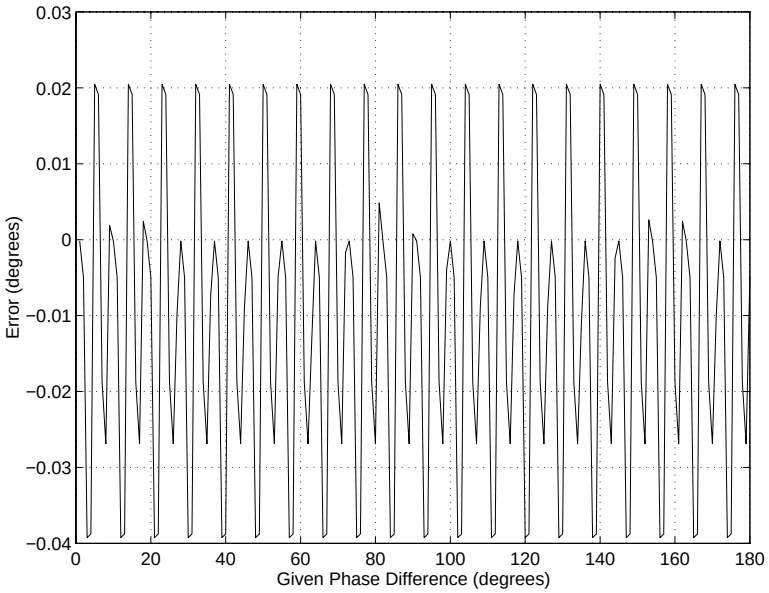

(a) Error curve from linear interpolation

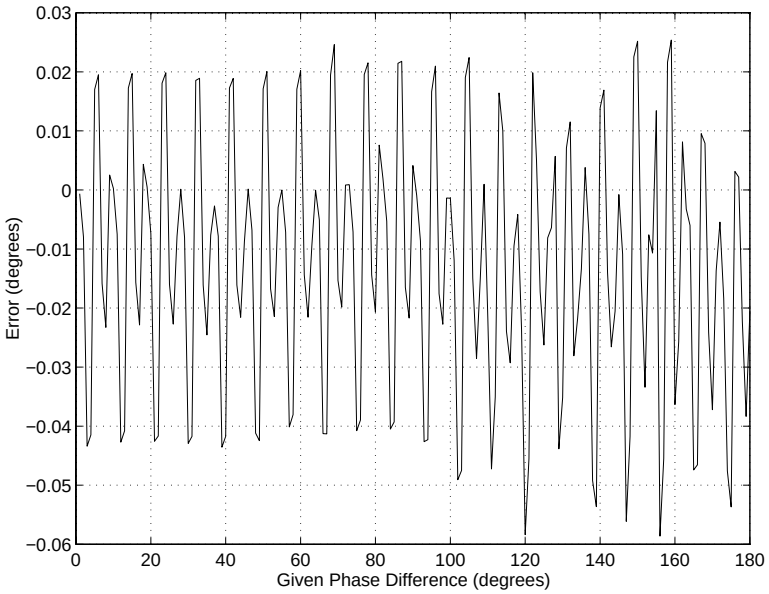

(b) Error curve from polynomial curve fitting

Figure 2.10: Error curves of phase differences from 8-bit grey-level fringe patterns

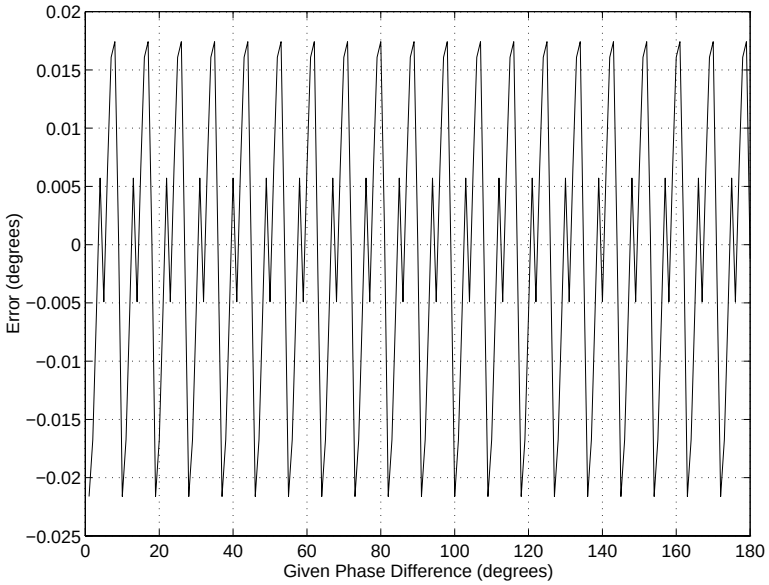

(a) Error curve from linear interpolation

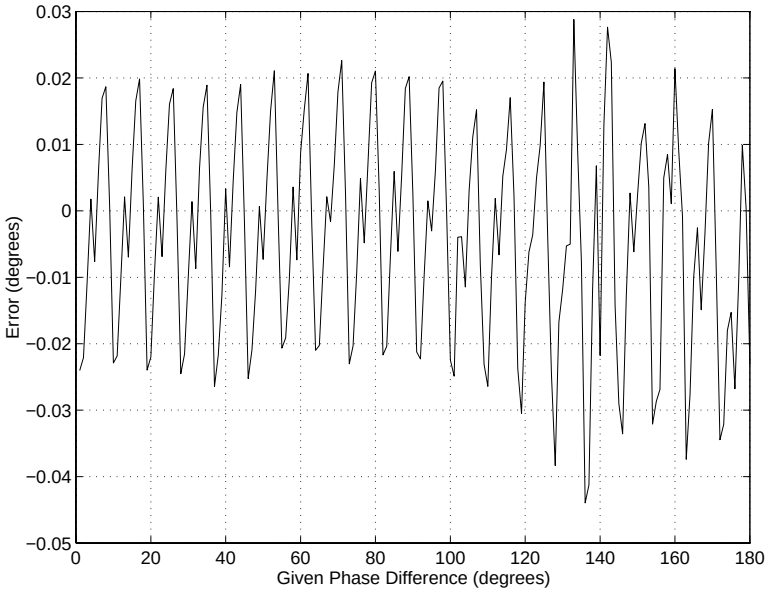

(b) Error curve from polynomial curve fitting

Figure 2.11: Error curves of phase differences from 10-bit grey-level fringe patterns

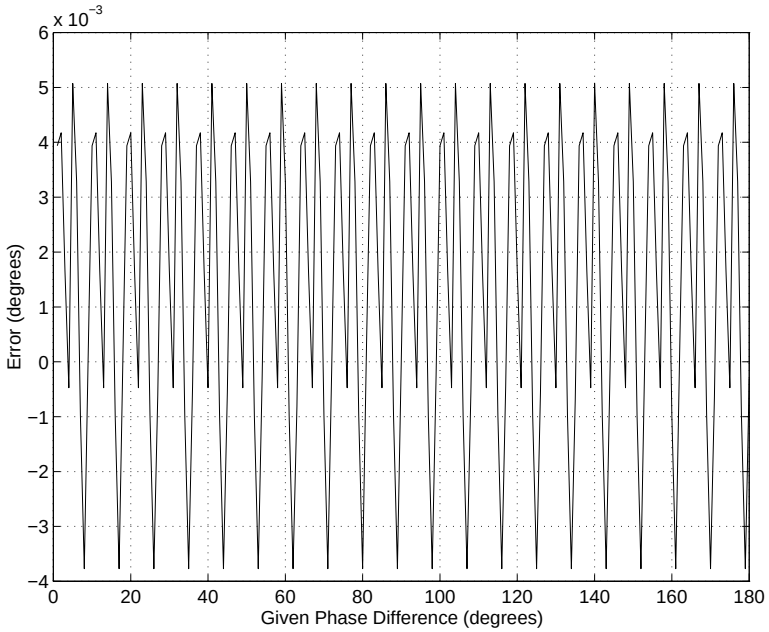

(a) Error curve from linear interpolation

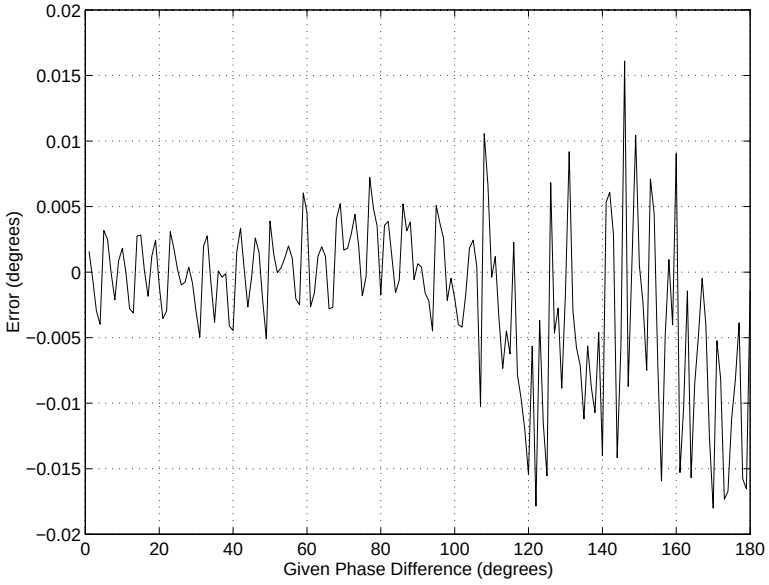

(b) Error curve from polynomial curve fitting

Figure 2.12: Error curves of phase differences from 12-bit grey-level fringe patterns

Table 2.1: Computer simulation results of the effect of grey-level resolution

Fringe period : 40 pixels

Grey levels (bits)	Maximum errors (degrees)		RMS values(degrees)	
	L.I.	P.C.F.	L.I.	P.C.F.
8	0.0392	0.0586	0.0236	0.0258
10	0.0216	0.0440	0.0127	0.0165
12	0.0051	0.0180	0.0031	0.0064

RMS=root-mean-square;

L.I.=linear interpolation;

P.C.F.=polynomial curve fitting.

2.5.2 Effect of Spatial Resolution

It has been known that a digital fringe pattern in a computer is expressed as an equi-spaced samples in the form of an array, and each element of the array is referred to as an picture element or pixel. In practice, the sampling number in one fringe period for the fringe pattern is required not only by the Nyquist frequency that fringe pattern is sampled at a frequency twice that of the highest spatial frequency presented in the fringe pattern but also by the accuracy of phase difference measurement since the accuracy of intensity values is limited by some factors such as the grey level resolution, detector nonlinearity and noise. In this subsection, the effect of spatial resolution on phase difference determination by fringe pattern matching is illustrated by computer simulation.

In the simulation, the fringe pattern size was kept in constant with 512×512 pixels and the measured intensity for each pixel was 8-bit grey levels. The intensity distribution was

$$\mathrm{I_n(i,j)} = \mathrm{round}[127.5 + 127.5\cos(\frac{2\pi \mathrm{i}}{\mathrm{P}} - \phi_\mathrm{n})], \quad \mathrm{n} = 0, 1, 2, ... \tag{2.30}$$

where i=0, 1, 2, ..., 511 and j=0, 1, 2, ..., 511. ϕ_n (ϕ_0=0) is the phase shift and P is the fringe period. The function round(x) rounds x to the nearest integer to obtain the quantised fringe pattern.

Figure 2.13(a) shows the error curve of phase difference measurement computed by linear interpolation for a sampling number of 20 pixels per fringe period, and the error curve by polynomial curve fitting is shown in figure 2.13(b). Figure 2.14 shows the computer simulation results from the fringe patterns with the sampling number of 30 pixels, and the computer simulation results from the sampling number of 40 pixels are shown as in figure 2.15. The computer simulation results of the effect of spatial resolution on phase difference determination are given in table 2.2.

In the simulation, the maximum error of phase difference measurement made by linear interpolation for the sampling number of 20 pixels per fringe period was 0.0764°, that for the sampling number of 30 pixels was 0.0536°, and that for the sampling number of 40 pixels was 0.0392°. As a result of comparison, the maximum error of phase difference measurement made by polynomial curve fitting for the sampling number of 20 pixels per fringe period was 0.1552°, that for the sampling number of 30 pixels was 0.0792°, and that for the sampling number of 40 pixels was 0.0586°.

It can be seen that the higher spatial resolution or sampling frequency has obtained a better accuracy from both linear interpolation and polynomial curve fitting in the measurement of phase difference by fringe pattern matching.

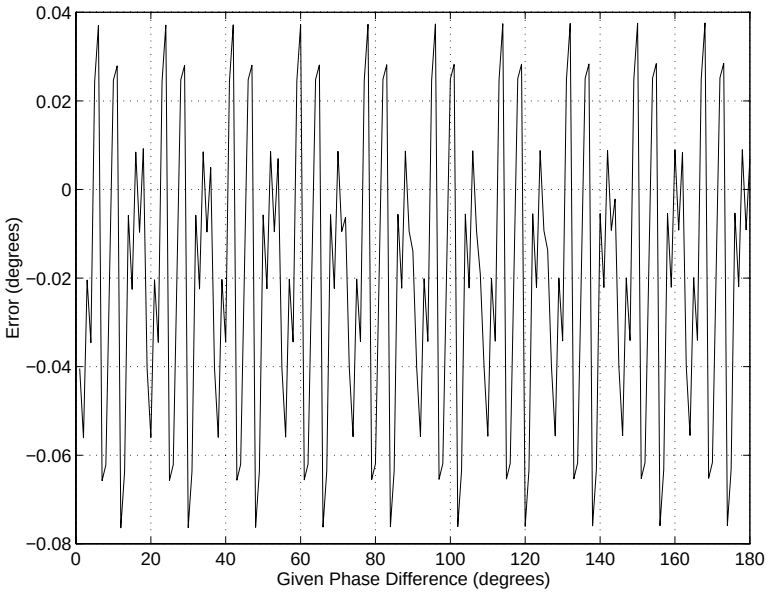

(a) Error curve from linear interpolation

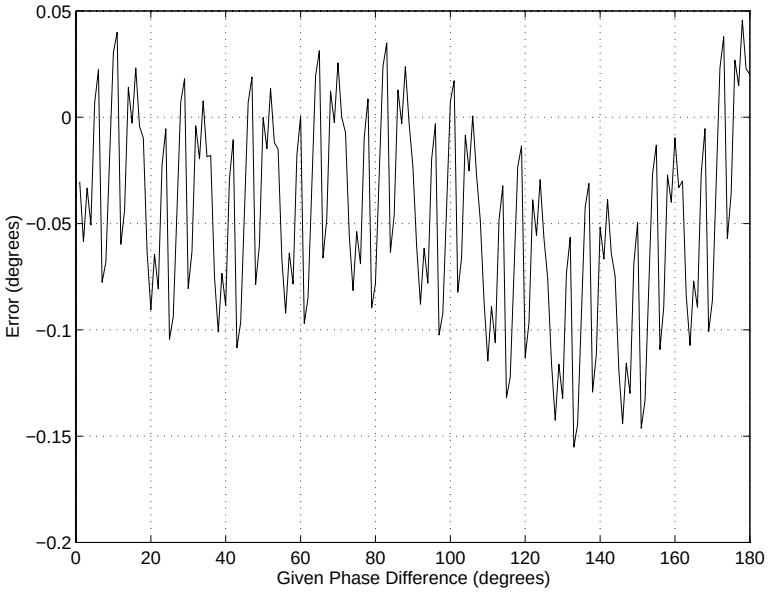

(b) Error curve from polynomial curve fitting

Figure 2.13: Error curves of phase differences from the sampling number of 20 pixels per fringe period

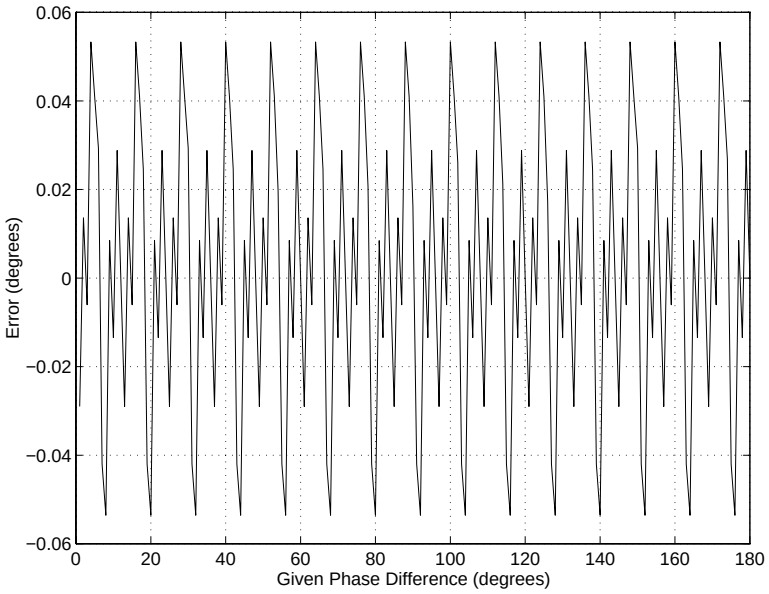

(a) Error curve from linear interpolation

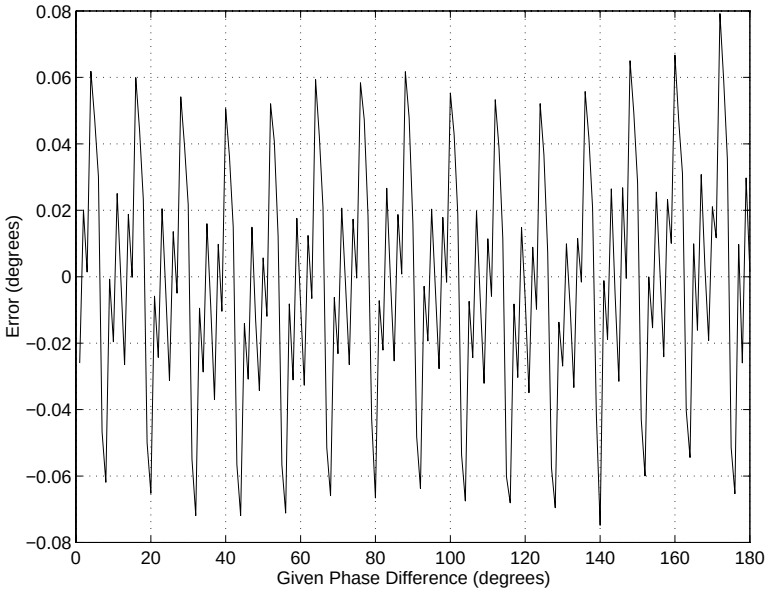

(b) Error curve from polynomial curve fitting

Figure 2.14: Error curves of phase differences from the sampling number of 30 pixels per fringe period

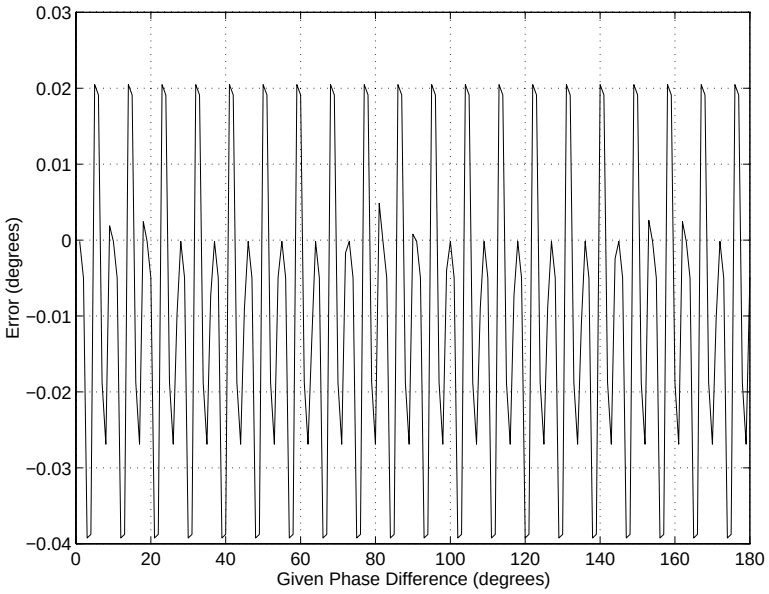

(a) Error curve from linear interpolation

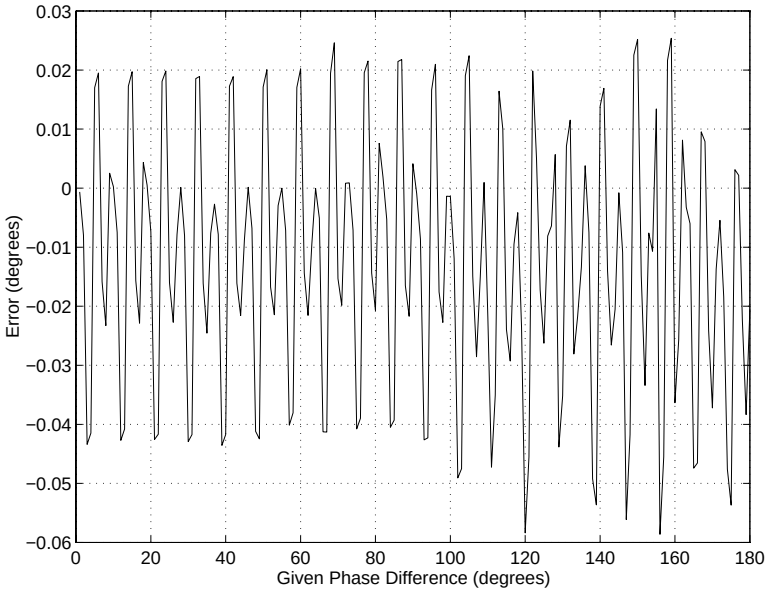

(b) Error curve from polynomial curve fitting

Figure 2.15: Error curves of phase differences from the sampling number of 40 pixels per fringe period

Table 2.2: Computer simulation results of the effect of spatial resolution

Grey-level resolution: 8 bits

Fringe period (pixels)	Maximum errors (degrees)		RMS values(degrees)	
	L.I.	P.C.F.	L.I.	P.C.F.
20	0.0764	0.1552	0.0401	0.0668
30	0.0536	0.0792	0.0316	0.0359
40	0.0392	0.0586	0.0236	0.0258

RMS=root-mean-square;

L.I.=linear interpolation;

P.C.F.=polynomial curve fitting.

2.6 Discussion

The region-based fringe pattern matching, which is expressed by the mismatch function, is powerful in the determination of phase difference from the interferograms. The mismatch function $f_n(t)$ is in effect the structure function of the fringe pattern $I_n(x, y, t)$. As such it can be written

$$E[I_0(x, y) - I_n(x \pm t, y)]^2 = 2\sigma^2[1 - \rho(t)] \tag{2.31}$$

where $\rho(t)$ is the autocorrelation function of I, σ^2 is the variance, and E is the expectation. Thus the structure function preserves the ability of the correlation function to improve the signal to noise ratio: the signal being the cosine pattern of the fringes. At the same time dependence on the background level is reduced because each value of the mismatch function $f_n(t)$ is obtained via a difference procedure [18].

It can be seen that the phase curves shown in figure 2.8 are different from the ideal phase curves shown in figure 2.2. In theory if the shifted image patch in a

fringe pattern is perfectly matched with the reference image patch in the reference fringe pattern the mismatch function is zero, as shown in figure 2.2. In practice it is not always true due to the presence of noise, the change of the fringe spacing, and the variations of the background illumination and the modulation of the fringes, as shown in figure 2.8.

From the computer simulation results shown in tables 2.1 and 2.2, it has been known that the accuracy of phase difference measurement is slightly influenced by imager resolutions. Therefore, the errors from the noise-free 8-bit grey-level fringe patterns with the size of 512×512 pixels can be neglected in many cases.

In the experiment, the rows from the top part of fringe pattern were used for obtaining the phase curves. For high precision measurement, the rows in the middle part of fringe pattern should be used for the calculation as the middle part of fringe pattern theoretically has less distortion in an interferometer system. In practice the phase errors are small and the inherent resolution of the PZT actuator may be contributing significantly, so the choice of position is less critical.

In addition, the experimental results indicate that the larger image patches have less distortion of the phase curves and higher signal to noise ratio in the presence of noise, but they need more processing time. In the application of this method, the size of image patch can be selected according to the shifting range of the image patch in the matching, the required accuracy and processing time. It should be noted that the achievable accuracy in the determination of phase difference is basically dependent on the quality of the image. The effect of image patch size on phase difference determination by fringe pattern matching will be discussed in detail in the following chapter.

2.7 Conclusion

The computer simulation and experiment have shown that fringe pattern matching is effective in the determination of phase difference between two interferograms with equi-spaced fringe patterns. The signal to noise ratio of the captured interferograms in the measurement is significantly improved due to the region-based matching and its effect of averaging noise. Subpixel accuracy can be achieved by linear interpolation or polynomial curve fitting from the phase curves. The method of linear interpolation is easier to achieve a better accuracy compared with polynomial curve fitting. Fringe pattern matching is useful in the measurement of the physical quantities that are related to optical phase changes such as length and displacement. The advantage of high tolerance to noise of this method makes it suitable to measurement in the presence of noise.

Bibliography

[1] P. Hariharn, "Interferometry with lasers," *Prog. Opt.* **24**, 105-164 (1987).

[2] M.J. Downs and K.W. Raine, "An unmodulated bi-directional fringe-counting interferometer system for measuring displacement," *Precision Eng.* **1**, 85-88 (1979).

[3] N. Hagiwara, Y. Nishitani, M. Yanase, and T. Saegusa, "A phase encoding method for improving the resolution and reliability of laser interferometers," *IEEE Trans. Instrum. Meas.* **38**(2), 548-551 (1989).

[4] S. Hosoe, "Laser interferometric system for displacement measurement with high precision," *Nanotechnology* **2**, 88-95 (1991)

[5] R. Crane, "Interference phase measurement," *Appl. Opt.* **8**(3), 538-542 (1969).

[6] M.J. Lavan, W.K. Cadwallender, and T.F. Deyoung, "Heterodyne interferometer to determine relative optical phase changes," *Rev. Sci. Instrum.* **46**(5), 525-527 (1975).

[7] P.G. Charette, I.W. Hunter, and C.J.H. Brenan, "A complete high performance heterodyne interferometer displacement transducer for microactuator control', *Rev. Sci. Instrum.* **63**(1), 241-248 (1992).

[8] M. Sasaki, K. Hane, S. Okuma, M. Hino, and Y. Bessho, "Improved differential heterodyne interferometer for atomic force microscopy," *Rev. Sci.*

Instrum. **65**(12), 3697-3701 (1994).

[9] D. Rugar, H.J. Mamin, R. Erlandsson, J.E. Stern, and B.D. Terris, "Force microscope using a fiber-optic displacement sensor," *Rev. Sci. Instrum.* **59**(11), 2337-2340 (1988).

[10] C. Schonenberger and S.F. Alarado, "A differential interferometer for force microscopy," *Rev. Sci. Instrum.* **60**(10), 3131-3134 (1989).

[11] D. Rugar, H.J. Mamin, and P. Guethner, "Improve fiber-optic interferometer for atomic force microscopy," *Appl. Phys. Lett.* **55**(25), 2588-2590 (1989).

[12] A. Goshtasby, G.C. Stockman, and C.V. Page, "A region-based approach to digital image registration with subpixel accuracy," *IEEE Trans. Geoscience and Remote Sensing* **GE-24**(3), 390-399 (1986).

[13] A. Kashko, H. Buxton, B.F. Buxton, and D.A. Castelow, 'Parallel matching and reconstruction algorithms in computer vision," *Parallel Computing* **8**(1-3), 3-17 (1988).

[14] G. He and K. Novak, "On line data capture by image matching on the mobile mapping system," *Proc. SPIE* **1820**, 50-56 (1992).

[15] A. Gruen and D. Stallmann, "High-accuracy matching of object edges', *Proc. SPIE* **1820**, 70-82 (1992).

[16] J.W. Dally, W.F. Riley, and K.G. McConnell, *Instrumentation for engineering measurements*, Wiley, New York (1993).

[17] P. Lancaster and K. Salkauskas, *Curve and Surface Fitting*, Academic Press, London (1986).

[18] D.J. Whitehouse, *Handbook of Surface Metrology*, Inst. of Physics Publishing, Bristol (1994).

Chapter 3

Effect of Image Patch Size on Phase Difference Determination by Fringe Pattern Matching

3.1 Introduction

Chapter 2 has described the method of phase difference determination by fringe pattern matching. It has been shown that fringe pattern matching is an optical interferometry method for the accurate determination of phase difference between fringe patterns. The method has the advantage of high resistance to noise due to the region-based matching process and its effect of averaging noise. This enables fringe pattern matching to be made thereby making meaningful measurements of optical phase differences even in harsh environmental conditions. However, the effect of image patch size on phase difference determination by fringe pattern matching is not discussed in chapter 2 from the statistical point of view.

In theory, the accuracy of phase difference measurement is not influenced by the size of the image patches used in the matching of ideal fringe patterns. In practice, however, the fringe patterns captured in an experiment are often inevitably

corrupted by random variations, or types of noise in light intensity values [1, 2]. Several types of noise such as Gaussian noise, salt & pepper noise, and speckle noise, are therefore invariably added to the fringe patterns in the measurement, and fringe pattern matching is, to some extent, limited by the random variations in its performance of detecting phase differences. In an interferometric phase measuring system, the random variations may arise from the CCD array, electronic circuit, light source, imaging surface and optical components.

In this chapter, the relationships between the standard deviations acquired from different sizes of image patches are investigated. The equations are derived based on the measurements made from one pixel, one line and an area of fringe patterns. The effect of image patch size on phase difference determination by fringe pattern matching was firstly examined by computer simulation. In the simulation, the fringe patterns with a phase difference of 90° and background noise level were generated by computer. Gaussian noise, salt & pepper noise, speckle noise and the combination of them were added to the intensity values of the fringe patterns. The phase differences between the fringe patterns were achieved by fringe pattern matching from different sizes of image patches. The experimental results were also achieved from one hundred pairs of captured interferograms. The theoretical analysis, computer simulation and experiment have shown that the larger image patches have achieved a better accuracy in the measurement of phase difference by fringe pattern matching.

In section 3.2, the general equations describing the effect of image patch size on phase difference determination by fringe pattern matching are derived based on statistical analysis. Section 3.3 illustrates the computer simulation results, and the experimental results are illustrated in section 3.4. The discussion and conclusion of this chapter are given in sections 3.5 and 3.6 respectively.

3.2 General Equations

In the method of phase difference determination by fringe pattern matching, any two interferograms with equi-spaced fringes are captured in sequence. A reference image patch in one interferogram, and a shifted image patch in the other with the same size as the reference image patch are selected for the matching process. The phase curves with the phase difference between the two interferograms are produced by shifting the image patches with respect to each other pixel by pixel, and at the same time calculating the mean-square-difference values for each shift. The optical phase difference can be decided from the matching point at which the mean-square-difference value is a minimum.

In the presence of noise, the sampled intensity distribution of the nth fringe pattern $I'_n(i,j)$, can be written as [3]

$$I'_n(i,j) = a(i,j) + b(i,j)\cos\phi_n(i,j) + \nu_n(i,j), \quad n = 0,1,2,... \tag{3.1}$$

where a(i,j) is the background illumination, b(i,j) is the modulation of the fringes, $\phi_n(i,j)$ is the phase related to the physical quantity to be measured, and $\nu_n(i,j)$ is the noise distribution.

The general mismatch function $f_n(t)$ in this case is

$$f_n(t) = k_0 \sum_{(i,j)\in R} [I'_0(i,j) - I'_n(i \pm t, j)]^2, \quad n = 0,1,2,... \tag{3.2}$$

where k_0 is the inverse of the element number in the calculations and the sign before t defines the fringe shifting direction. For the fringes shifted in the left direction the mismatch function is

$$f_n(t) = k_0 \sum_{(i,j)\in R} [I'_0(i,j) - I'_n(i - t, j)]^2, \quad n = 0,1,2,... \tag{3.3}$$

and for the fringes shifted in the right direction the mismatch function is

$$f_n(t) = k_0 \sum_{(i,j)\in R} [I_0^{'}(i,j) - I_n^{'}(i+t,j)]^2, \quad n = 0,1,2,... \tag{3.4}$$

Consider a measurement value of phase difference p_m in a set of phase difference samples, which is formed by the addition of noise η_m to the sample mean value $\bar{p}$. The measured phase difference p_m is

$$p_m = \bar{p} + \eta_m, \quad m = 1,2,3,... \tag{3.5}$$

where η_m denotes a zero mean noise process [4, 5, 6], i.e. the expectation $E(\eta_m) = 0$.

In a measurement of K phase difference samples, the standard deviation σ [7, 8] can be calculated by

$$\sigma = \sqrt{\frac{\sum_{m=1}^{K}(p_m - \bar{p})^2}{K-1}} \tag{3.6}$$

where

$$\bar{p} = \frac{1}{K}\sum_{m=1}^{K} p_m \tag{3.7}$$

To discuss the relationship between the standard deviation achieved from $1 \times N$ pixel image patches and that achieved from $M \times N$ pixel image patches in the measurement, the mismatch function described by equation 3.2 can be rewritten as

$$f_n(t) = k_0 \sum_{j=1}^{M} h_n(t,j), \quad n = 0,1,2,... \tag{3.8}$$

For the fringes shifted in the left direction the mismatch function is

$$f_n(t) = k_0 \sum_{j=1}^{M} h_{ln}(t,j), \quad n = 0,1,2,... \tag{3.9}$$

and for the fringes shifted in the right direction the mismatch function is

$$f_n(t) = k_0 \sum_{j=1}^{M} h_{rn}(t,j), \quad n = 0,1,2,... \tag{3.10}$$

where

$$h_n(t,j) = \sum_{i=1}^{N}[I_0^{'}(i,j) - I_n^{'}(i \pm t,j)]^2, \quad n = 0,1,2,... \tag{3.11}$$

$$h_{ln}(t,j) = \sum_{i=1}^{N}[I_0^{'}(i,j) - I_n^{'}(i - t,j)]^2, \quad n = 0,1,2,... \tag{3.12}$$

$$h_{rn}(t,j) = \sum_{i=1}^{N}[I_0^{'}(i,j) - I_n^{'}(i + t,j)]^2, \quad n = 0,1,2,... \tag{3.13}$$

It can be seen that $h_n(t,j)$, $h_{ln}(t,j)$ and $h_{rn}(t,j)$ are the mismatch functions obtained from the jth line of the image patches, or an image patch of 1×N pixels. This means that the phase curves described by equations 3.8, 3.9, and 3.10 can be achieved by the superposition of all the phase curves obtained from one line measurement or the measurement based on each line of the image patches used in the matching process. In this case, the phase difference achieved from M × N pixel image patches can be considered as the mean of those from 1 × N pixel image patches.

Providing that the line measurements are uncorrelated, the standard deviation σ_M, for the image patches with M×N pixels used in the determination of phase difference by fringe pattern matching, can be calculated by [6, 8, 9]

$$\sigma_M = \frac{\sigma_1}{\sqrt{M}} \tag{3.14}$$

where M is the number of lines in the image patches used for the matching process, and σ_1 is the standard deviation obtained from one line measurement.

In the same way, to discuss the relationship between the standard deviation achieved from 1 × 1 pixel image patches or one pixel, and that from M × N pixel image patches in the measurement, the general mismatch function described by equation 3.2 can be rewritten as

$$f_n(t) = k_0 \sum_{j=1}^{M}\sum_{i=1}^{N} q_n(t,i,j), \quad n = 0,1,2,... \tag{3.15}$$

For the fringes shifted in the left direction the mismatch function is

$$f_n(t) = k_0 \sum_{j=1}^{M} \sum_{i=1}^{N} q_{ln}(t,i,j), \quad n = 0,1,2,... \tag{3.16}$$

and for the fringes shifted in the right direction the mismatch function is

$$f_n(t) = k_0 \sum_{j=1}^{M} \sum_{i=1}^{N} q_{rn}(t,i,j), \quad n = 0,1,2,... \tag{3.17}$$

where

$$q_n(t,i,j) = [I_0^{'}(i,j) - I_n^{'}(i \pm t,j)]^2, \quad n = 0,1,2,... \tag{3.18}$$

$$q_{ln}(t,i,j) = [I_0^{'}(i,j) - I_n^{'}(i - t,j)]^2, \quad n = 0,1,2,... \tag{3.19}$$

$$q_{rn}(t,i,j) = [I_0^{'}(i,j) - I_n^{'}(i + t,j)]^2, \quad n = 0,1,2,... \tag{3.20}$$

It is clear that $q_n(t,i,j)$, $q_{ln}(t,i,j)$ and $q_{rn}(t,i,j)$ are the mismatch functions obtained from one pixel, or an image patch of 1×1 pixel. This means that the phase curves from the image patches of $M \times N$ pixels can be expressed as the superposition of all the phase curves from one pixel. Therefore, the phase difference achieved from $M \times N$ pixel image patches can be considered as the mean of those from 1×1 pixel image patches. As such the standard deviation σ_M can also be calculated by

$$\sigma_M = \frac{\sigma_0}{\sqrt{M \times N}} \tag{3.21}$$

where $M \times N$ is the number of pixels in the image patches used for the matching process and σ_0 is the standard deviation acquired from the measurements based on one pixel.

In the above, equations 3.14 and 3.21 indicate that the larger image patches have a better accuracy in the measurement of phase difference by fringe pattern matching. It is now clear that the direct measurement of phase difference is based on the data from one pixel, but the measurement made by fringe pattern matching

is based on the data from M×N pixels. Therefore, fringe pattern matching has the advantage of averaging noise in the measurement of phase difference.

3.3 Computer Simulation

The effect of image patch size on phase difference determination by fringe pattern matching was firstly examined in computer simulation. The fringe patterns with Gaussian noise, salt & pepper noise, speckle noise and the combination of them were generated by computer for the quantitative evaluation of errors in the measurement of phase difference. The image patches of 1×382, 10×382 and 100×382 pixels were then used for the determination of phase difference in the matching process.

3.3.1 Fringe Patterns with Gaussian Noise

Gaussian noise is a model for the noise from imaging electronics in a machine vision or imaging system with CCD cameras, and it contains variations in light intensity which are described by normal or Gaussian distribution [10]. There are two noise sources in this case [4]. The conversion of a fringe pattern from optical to electrical form introduces photoelectronic noise, which is a statistical process in nature since each pixel receives a finite number of photons. The electronic circuits that process the signal introduce the electronic noise that is due to the random thermal motion of electrons in resistive circuit elements and is usually modelled as Gaussian noise with zero mean value.

In the simulation of the effect of Gaussian noise, the computer generated fringe patterns were 8-bit grey-level, 512× 512 pixel images with a phase difference of 90° and a fringe period of 40 pixels. The noise distributions were produced using MATLAB command *imnoise(I', 'gaussian', M, V)* [11]. The command added

Gaussian noise of mean M and variance V to the image $I^{'}$. The mean M and variance V were both 20 in the simulation. The light intensity distributions were

$$\mathrm{I}_0^{'}(\mathrm{i},\mathrm{j}) = \mathrm{round}[127.5 + 127.5\cos(\frac{\pi \mathrm{i}}{20}) + \nu_{0(\mathrm{Gaussian})}(\mathrm{i},\mathrm{j})] \tag{3.22}$$

and

$$\mathrm{I}_\mathrm{m}^{'}(\mathrm{i},\mathrm{j}) = \mathrm{round}[127.5 + 127.5\cos(\frac{\pi \mathrm{i}}{20} - \frac{\pi}{2}) + \nu_{\mathrm{m}(\mathrm{Gaussian})}(\mathrm{i},\mathrm{j})] \tag{3.23}$$

where m=1, 2, 3, ..., 100, i=0, 1, 2, ..., 511 and j=0, 1, 2, ..., 511. $\nu_{0(\mathrm{Gaussian})}(\mathrm{i},\mathrm{j})$ and $\nu_{\mathrm{m}(\mathrm{Gaussian})}(\mathrm{i},\mathrm{j})$ are Gaussian noise distributions. The function round(x) rounds x to the nearest integer to obtain the quantised fringe pattern.

Figure 3.1 shows two computer generated fringe patterns with Gaussian noise. The light intensities with Gaussian noise in row 1 of the fringe patterns are shown in figure 3.2. Figure 3.3 shows the Gaussian noise in row 1 of the fringe patterns. The phase curves acquired from the image patches of 1×382, 10×382 and 100×382 pixels are shown in figure 3.4.

One hundred pairs of fringe patterns were used in the simulation for the evaluation of the effect of image patch size on phase difference determination in the presence of Gaussian noise. The standard deviations achieved from the image patches of 1×382, 10×382 and 100×382 pixels, as shown in table 1, were 0.2048°, 0.0688° and 0.0197°. The results calculated from equation 3.14 were $\sigma_{10} \approx 0.0648°$ and $\sigma_{100} \approx 0.0205°$ when σ_1 was 0.2048°.

The MATLAB programme for the computer simulation of the effect of Gaussian noise on phase difference determination by fringe pattern matching is given in appendix B. The three hundred phase difference samples from the different sizes of image patches and the results are shown in appendix C.1.

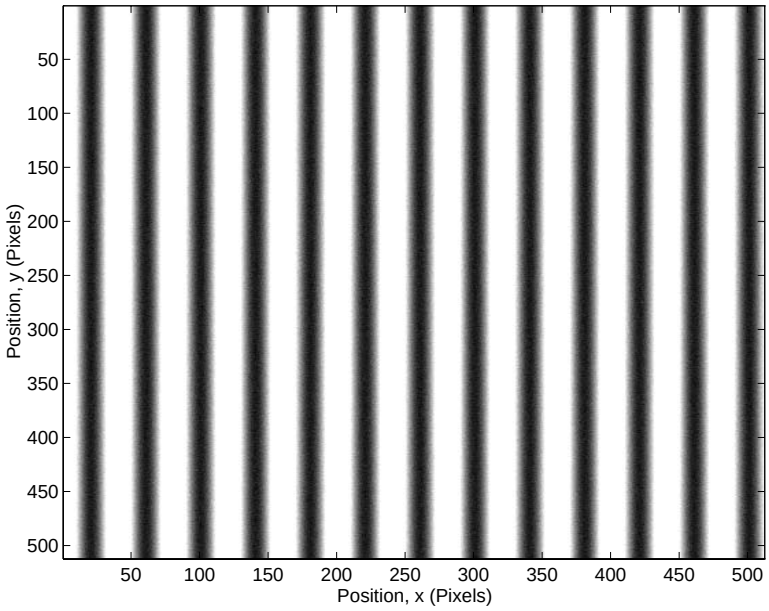

(a) Fringe pattern with a phase shift of 0°

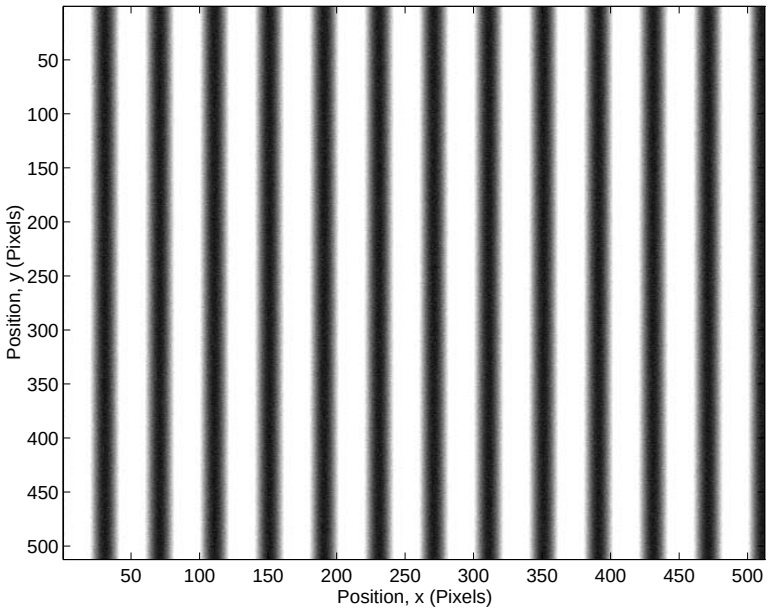

(b) Fringe pattern with a phase shift of 90°

Figure 3.1: Two computer generated fringe patterns with Gaussian noise

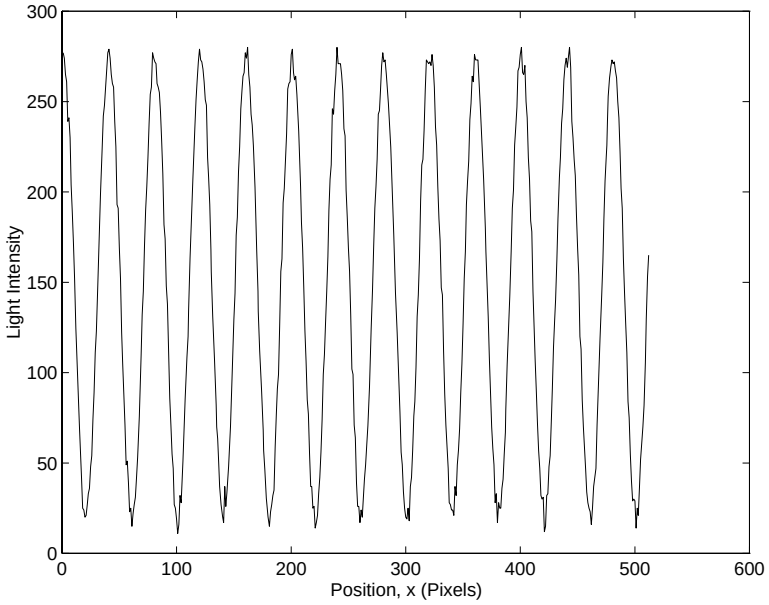

(a) Light intensity from the fringe pattern with a phase shift of 0°

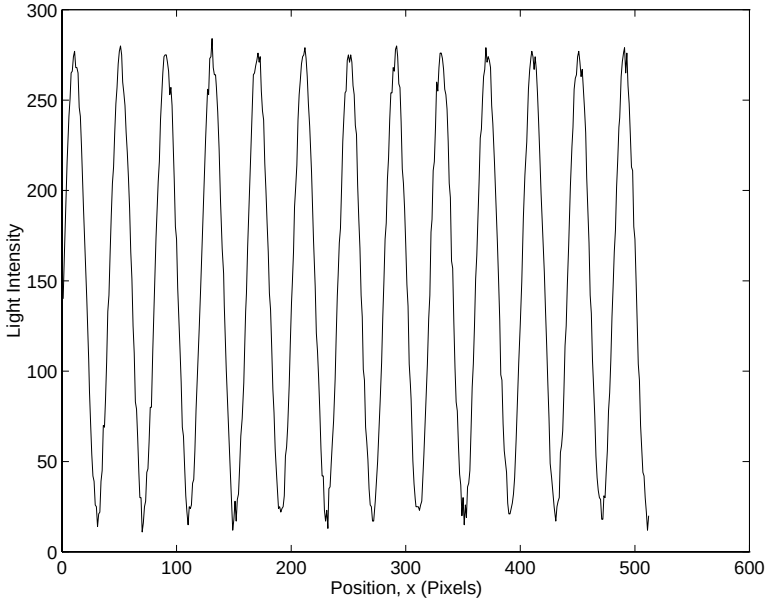

(b) Light intensity from the fringe pattern with a phase shift of 90°

Figure 3.2: Light intensities in row 1 from the fringe patterns with Gaussian noise

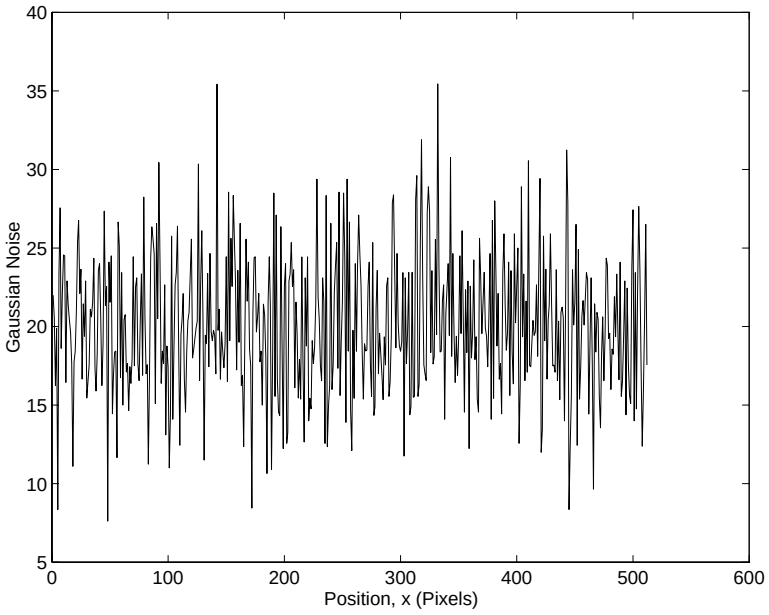

(a) Gaussian noise from the fringe pattern with a phase shift of 0°

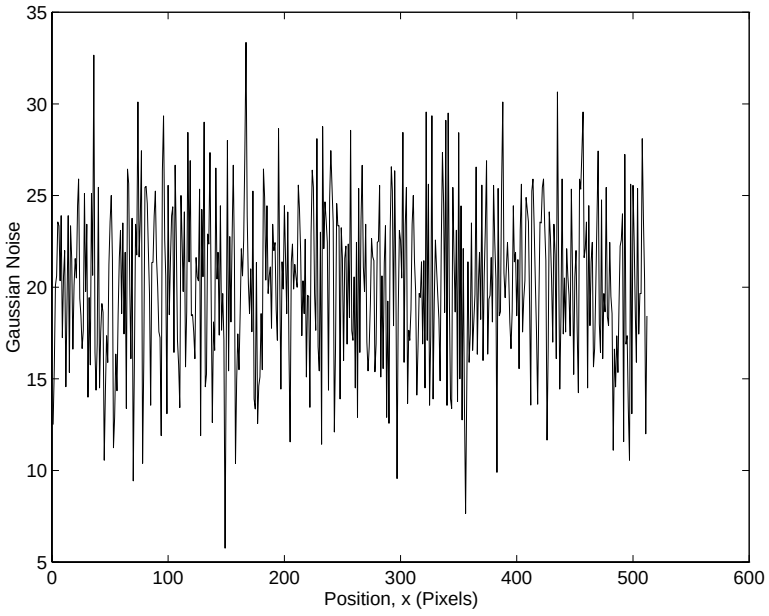

(b) Gaussian noise from the fringe pattern with a phase shift of 90°

Figure 3.3: Gaussian noise in row 1

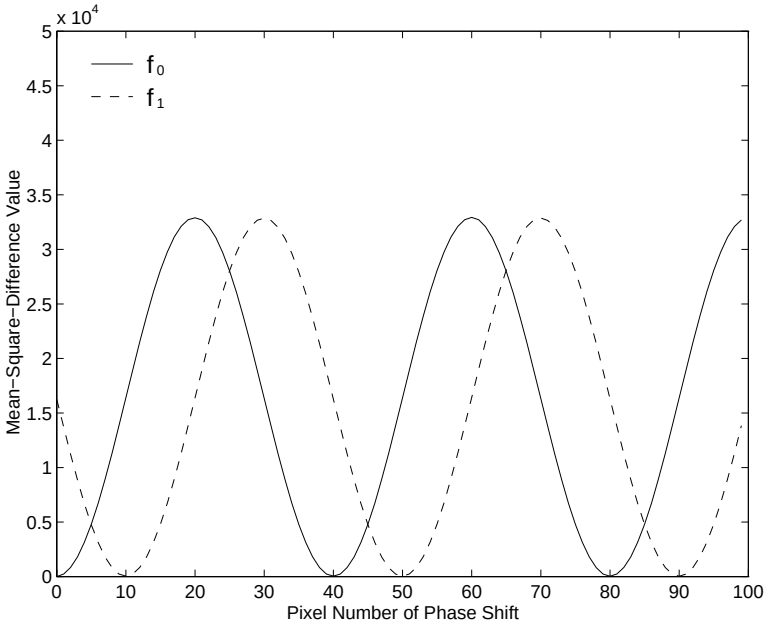

(a) Phase curves from 1×382 pixel image patches

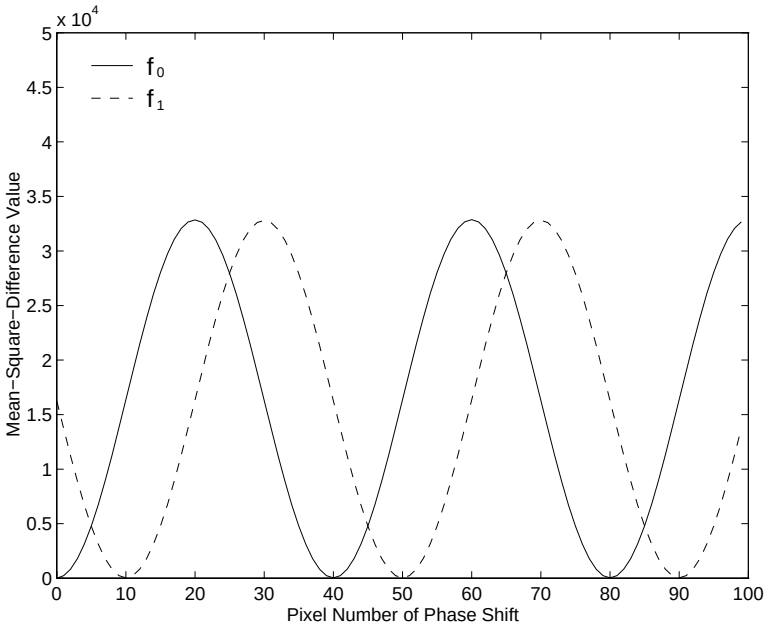

(b) Phase curves from 10×382 pixel image patches

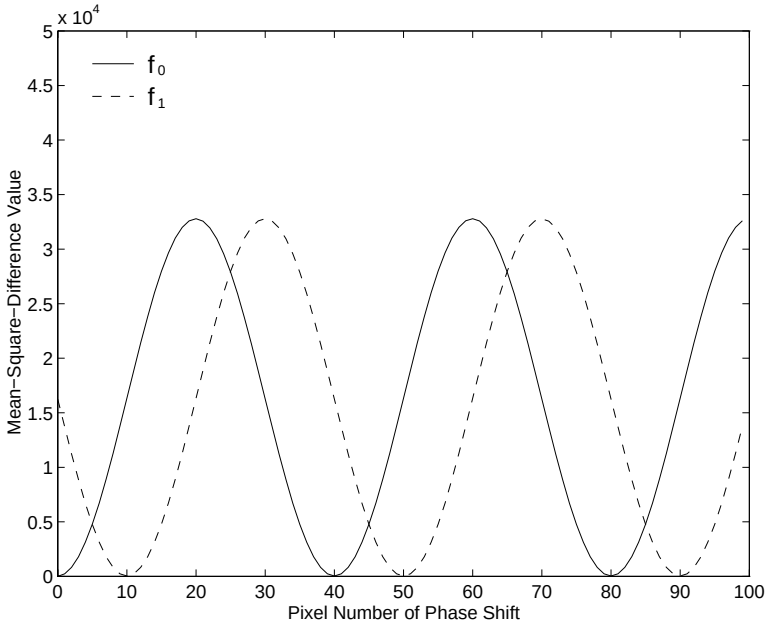

(c) Phase curves from 100×382 pixel image patches

Figure 3.4: Phase curves from the different sizes of image patches with Gaussian noise

Table 3.1: Computer simulation results from the fringe patterns with Gaussian noise

Size of image patch (pixels)	Mean (degrees)	Standard Deviation σ (degrees)	Standard Deviation σ_M (degrees)
1x382	90.0102	0.2048	0.2048
10x382	90.0102	0.0688	0.0648
100x382	90.0022	0.0197	0.0205

Number of Samples K=100

3.3.2 Fringe Patterns with Salt & Pepper Noise

In the light intensity distributions of fringe patterns, salt & pepper noise contains random occurrences of both black and white intensity values [10]. This type of noise may arise from the interference in electronic circuits, uneven sensitivities of imaging pixels, unclean or uneven surfaces of optical components and objects.

In the simulation of the effect of salt & pepper noise, the computer generated fringe patterns were 8-bit grey-level, 512× 512 pixel images with a phase difference of 90° and a fringe period of 40 pixels. The noise distributions were produced using MATLAB command *imnoise(I', 'salt & pepper', D)* [11]. The command added salt & pepper noise to the image I' with the noise density D. The noise density D was 0.06 in the simulation. The light intensity distributions were

$$\mathrm{I}_0'(\mathrm{i},\mathrm{j}) = \mathrm{round}[127.5 + 127.5\cos(\frac{\pi \mathrm{i}}{20}) + \nu_{0(\mathrm{salt\&pepper})}(\mathrm{i},\mathrm{j})] \tag{3.24}$$

and

$$\mathrm{I}_\mathrm{m}'(\mathrm{i},\mathrm{j}) = \mathrm{round}[127.5 + 127.5\cos(\frac{\pi \mathrm{i}}{20} - \frac{\pi}{2}) + \nu_{\mathrm{m}(\mathrm{salt\&pepper})}(\mathrm{i},\mathrm{j})] \tag{3.25}$$

where m=1, 2, 3, ..., 100, i=0, 1, 2, ..., 511 and j=0, 1, 2, ..., 511. $\nu_{0(\mathrm{salt\&pepper})}(\mathrm{i},\mathrm{j})$ and $\nu_{\mathrm{m}(\mathrm{salt\&pepper})}(\mathrm{i},\mathrm{j})$ are salt & pepper noise distributions. The function round(x) rounds x to the nearest integer to acquire the quantised fringe pattern.

Figure 3.5 shows two computer generated fringe patterns with salt & pepper noise. The light intensities with salt & pepper noise in row 1 of the fringe patterns are shown in figure 3.6. Figure 3.7 shows the salt & pepper noise distribution in row 1, and figure 3.8 shows the phase curves obtained from the image patches of 1×382, 10×382 and 100×382 pixels.

In the simulation, one hundred pairs of image patches were used for the evaluation of the effect of image patch size on phase difference determination in the

presence of salt & pepper noise. The standard deviations obtained from the image patches of 1×382, 10×382 and 100×382 pixels, as shown in table 3.2, were 1.6412°, 0.5018° and 0.1441°. The results computed from equation 3.14 were $\sigma_{10} \approx 0.5190°$ and $\sigma_{100} \approx 0.1641°$ when σ_1 was 1.6412°. The phase difference samples used in the simulation and the results are given in appendix C.2.

Table 3.2: Computer simulation results from the fringe patterns with salt & pepper noise

Size of image patch (pixels)	Mean (degrees)	Standard Deviation σ (degrees)	Standard Deviation σ_M (degrees)
1x382	90.1629	1.6412	1.6412
10x382	90.0537	0.5018	0.5190
100x382	90.0138	0.1441	0.1641

Number of Samples K=100

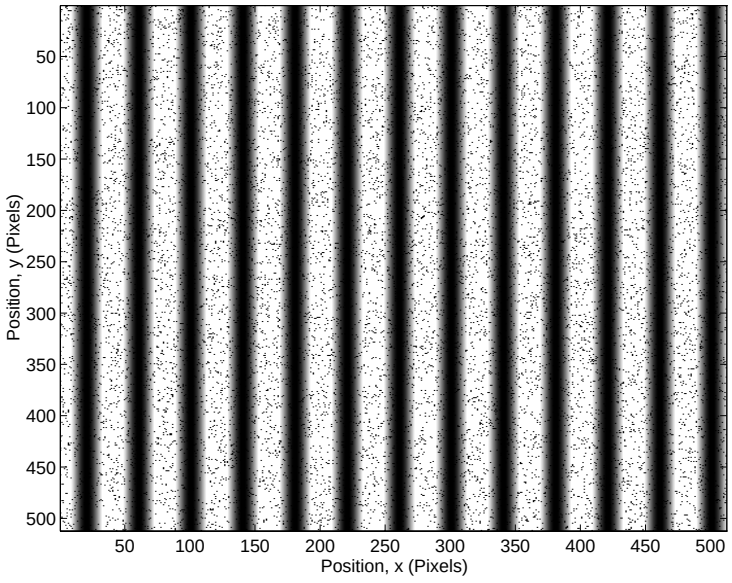

(a) Fringe pattern with a phase shift of 0°

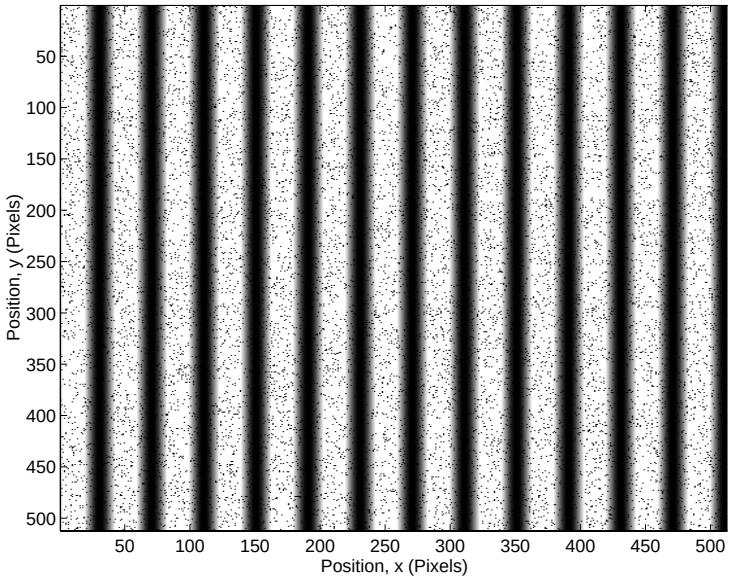

(b) Fringe pattern with a phase shift of 90°

Figure 3.5: Two computer generated fringe patterns with salt & pepper noise

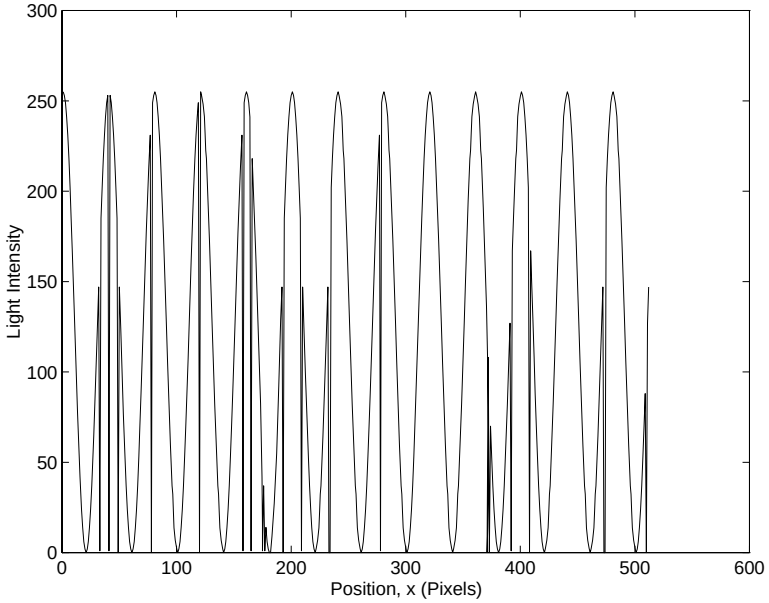

(a) Light intensity from the fringe pattern with a phase shift of 0°

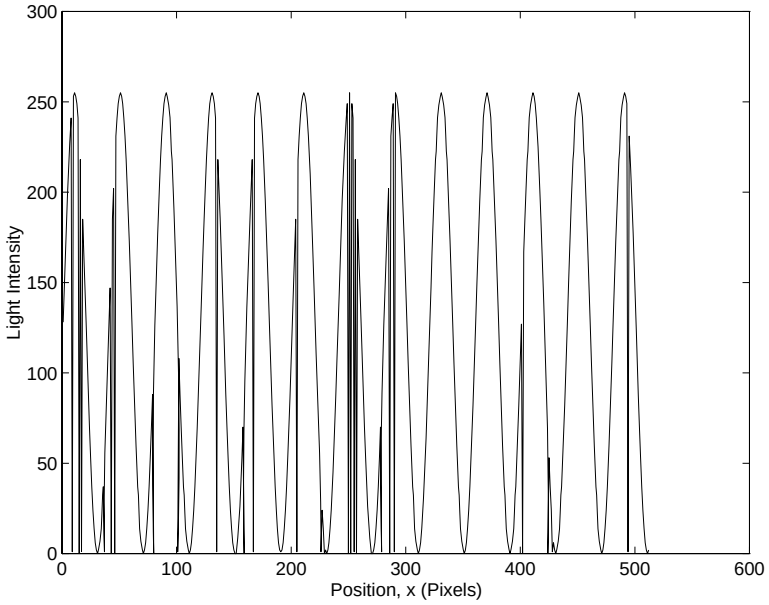

(b) Light intensity from the fringe pattern with a phase shift of 90°

Figure 3.6: Light intensities in row 1 from the fringe patterns with salt & pepper noise

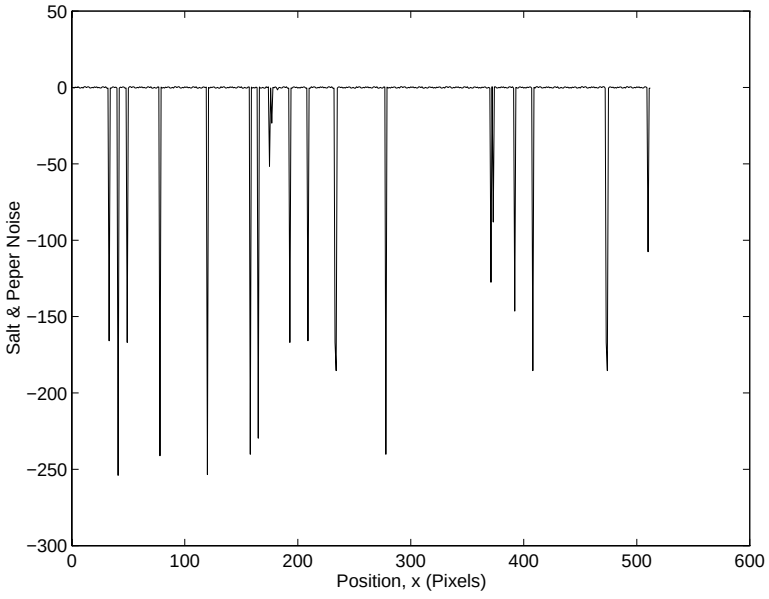

(a) Salt & pepper noise from the fringe pattern with a phase shift of 0°

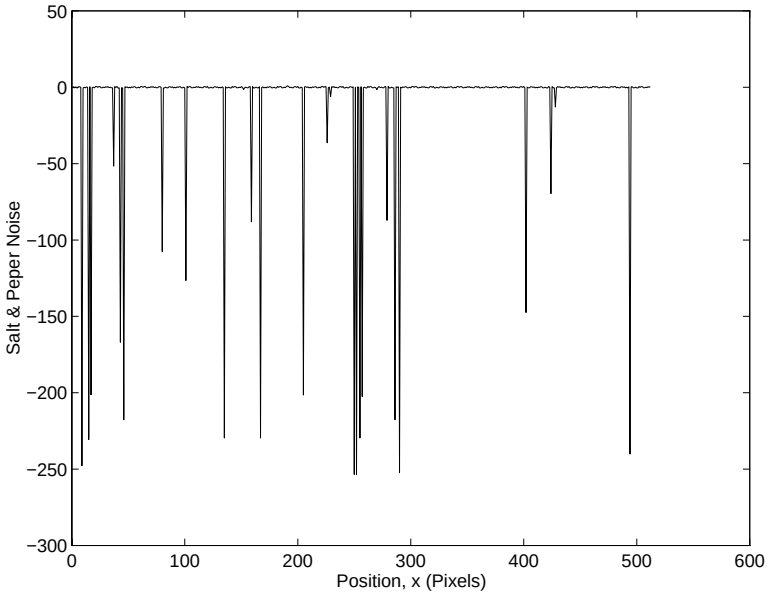

(b) Salt & pepper noise from the fringe pattern with a phase shift of 90°

Figure 3.7: Salt & pepper noise in row 1

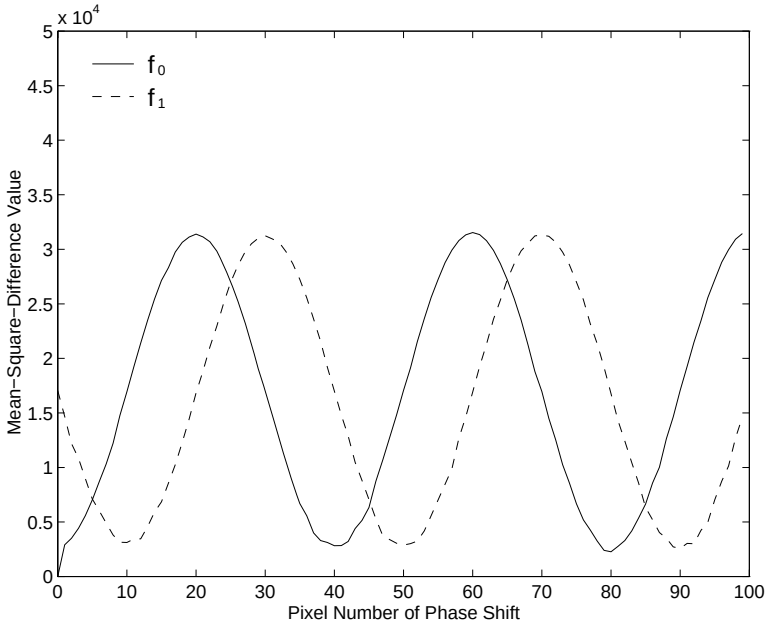

(a) Phase curves from 1×382 pixel image patches

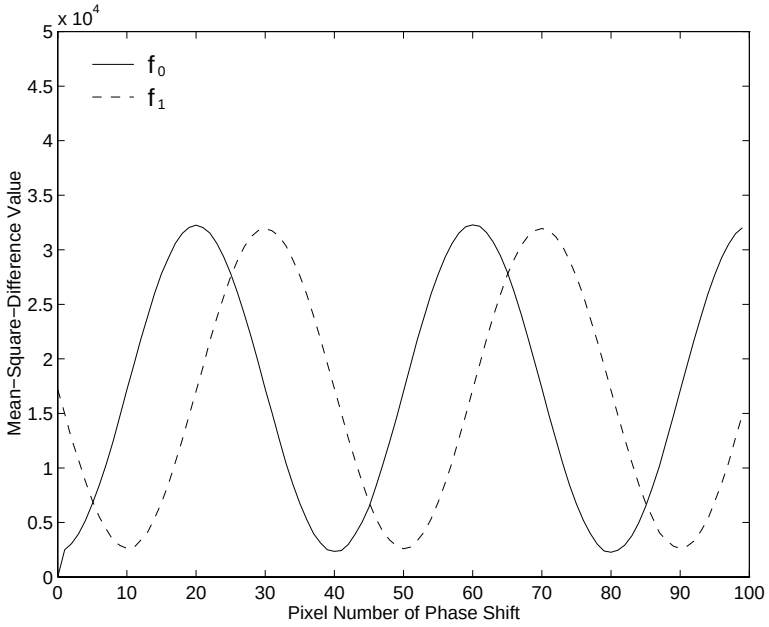

(b) Phase curves from 10×382 pixel image patches

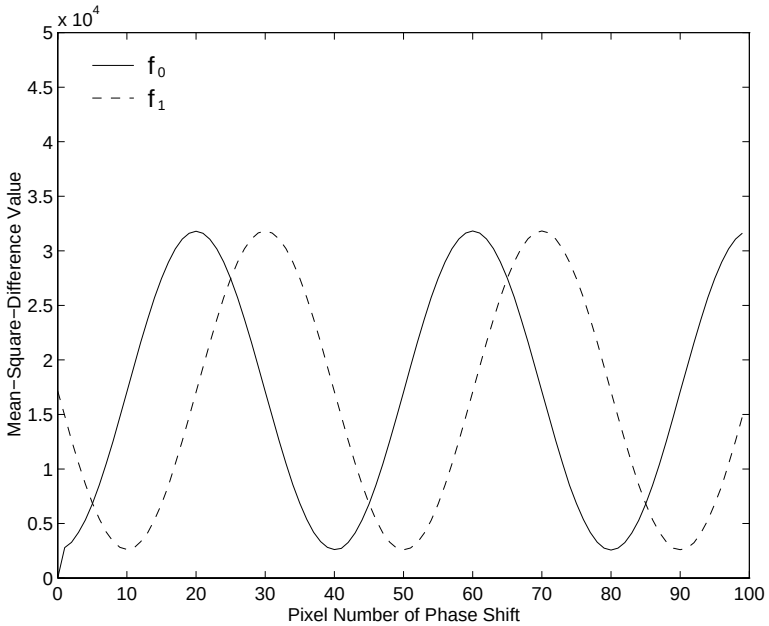

(c) Phase curves from 100×382 pixel image patches

Figure 3.8: Phase curves from the different sizes of image patches with salt & pepper noise

3.3.3 Fringe Patterns with Speckle Noise

Speckle noise, which is often a dominant error source in most of interferometric phase measuring systems, occurs only when the surface is optically rough [5, 12]. This means that the height variation of the surface is of the order of wavelength or greater than the wavelength of the illuminating light. When such a surface is illuminated by a laser beam and an image of the surface is formed, the image shows a random intensity variation with the granular appearance of the surface. It is known that the fully developed speckle field obeys a zero-mean Gaussian process if a large number of statistically independent scatterers contribute to the formation of the speckle field [12].

In the simulation of the effect of speckle noise on phase difference determination by fringe pattern matching, the computer generated fringe patterns were 512× 512 pixel images with a phase difference of 90° and a fringe period of 40 pixels, and their grey-level resolution was about 8 bits. The noise distributions were produced using MATLAB command *imnoise(I', 'speckle', V)* [11]. The command added speckle noise with the variance V to the image I'. The variance V was 0.15 in the simulation. The light intensity distributions of the fringe patterns were

$$\mathrm{I}'_0(\mathrm{i},\mathrm{j}) = \mathrm{round}[127.5 + 127.5\cos(\frac{\pi \mathrm{i}}{20}) + \nu_{0(\mathrm{speckle})}(\mathrm{i},\mathrm{j})] \tag{3.26}$$

and

$$\mathrm{I}'_{\mathrm{m}}(\mathrm{i},\mathrm{j}) = \mathrm{round}[127.5 + 127.5\cos(\frac{\pi \mathrm{i}}{20} - \frac{\pi}{2}) + \nu_{\mathrm{m}(\mathrm{speckle})}(\mathrm{i},\mathrm{j})] \tag{3.27}$$

where m=1, 2, 3, ..., 100, i=0, 1, 2, ..., 511 and j=0, 1, 2, ..., 511. $\nu_{0(\mathrm{speckle})}(\mathrm{i},\mathrm{j})$ and $\nu_{\mathrm{m}(\mathrm{speckle})}(\mathrm{i},\mathrm{j})$ are speckle noise distributions. The function round(x) rounds x to the nearest integer to obtain the quantised fringe pattern.

Figure 3.9 shows two computer generated fringe patterns with speckle noise. The light intensities with speckle noise in row 1 of the fringe patterns are shown

in figure 3.10. Figure 3.11 shows the speckle noise in row 1. The phase curves acquired from the image patches of 1×382, 10×382 and 100×382 pixels are shown in figure 3.12.

One hundred pairs of image patches were used in the simulation for the evaluation of the effect of image patch size on phase difference determination in the presence of speckle noise. The standard deviations obtained from the image patches of 1×382, 10×382 and 100×382 pixels, as shown in table 3.3, were 1.4283°, 0.4830° and 0.1430°. The results computed from equation 3.14 were $\sigma_{10} \approx 0.4517°$ and $\sigma_{100} \approx 0.1428°$ when σ_1 was 1.4283°. The phase difference samples used in the simulation and the results are shown in appendix C.3.

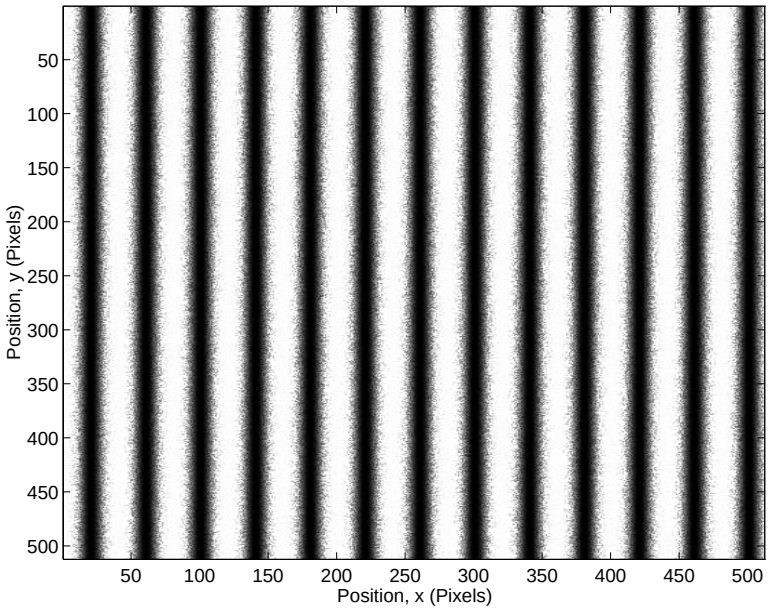

(a) Fringe pattern with a phase shift of 0°

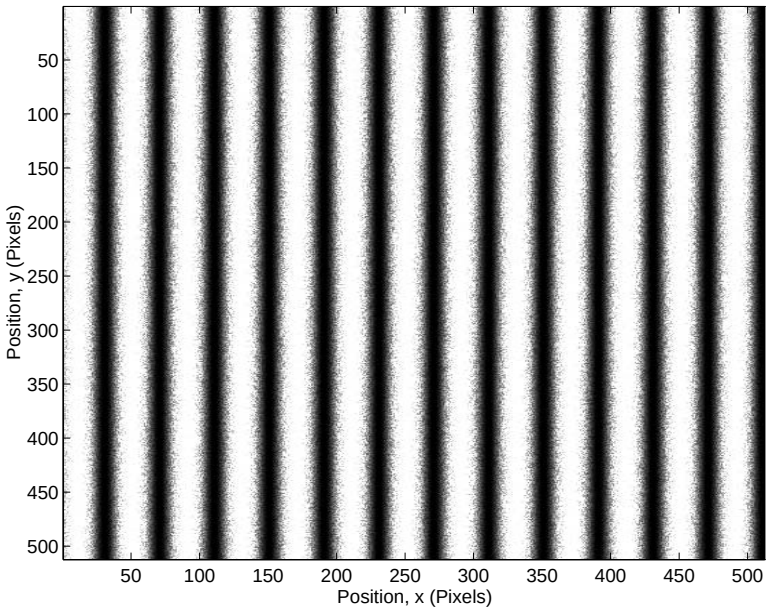

(b) Fringe pattern with a phase shift of 90°

Figure 3.9: Two computer generated fringe patterns with speckle noise

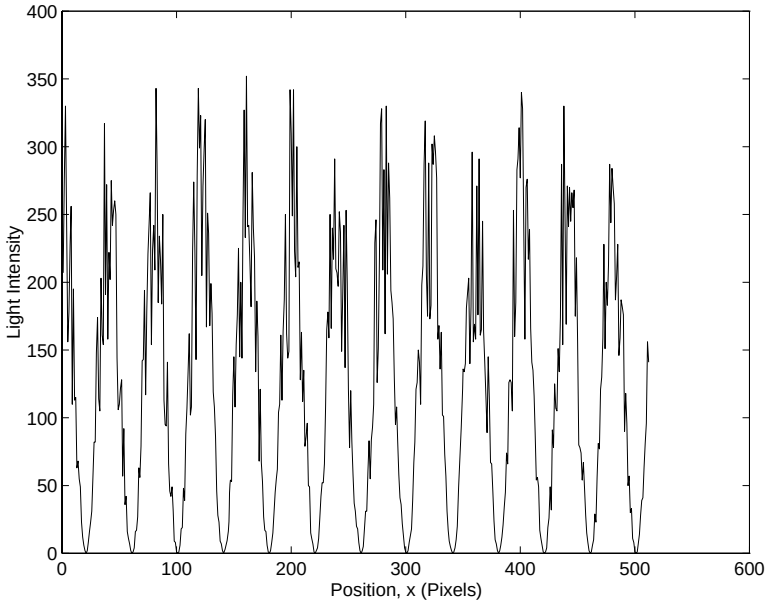

(a) Light intensity from the fringe pattern with a phase shift of 0°

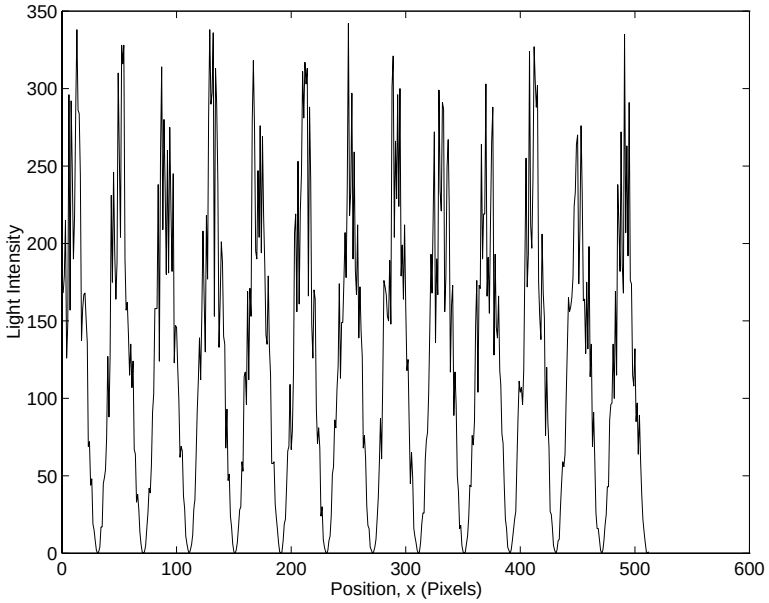

(b) Light intensity from the fringe pattern with a phase shift of 90°

Figure 3.10: Light intensities in row 1 from the fringe patterns with speckle noise

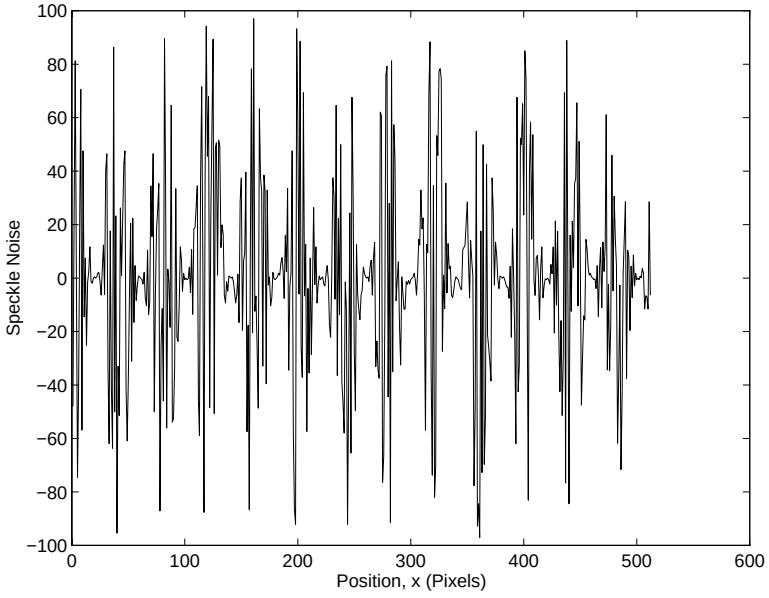

(a) Speckle noise from the fringe pattern with a phase shift of 0°

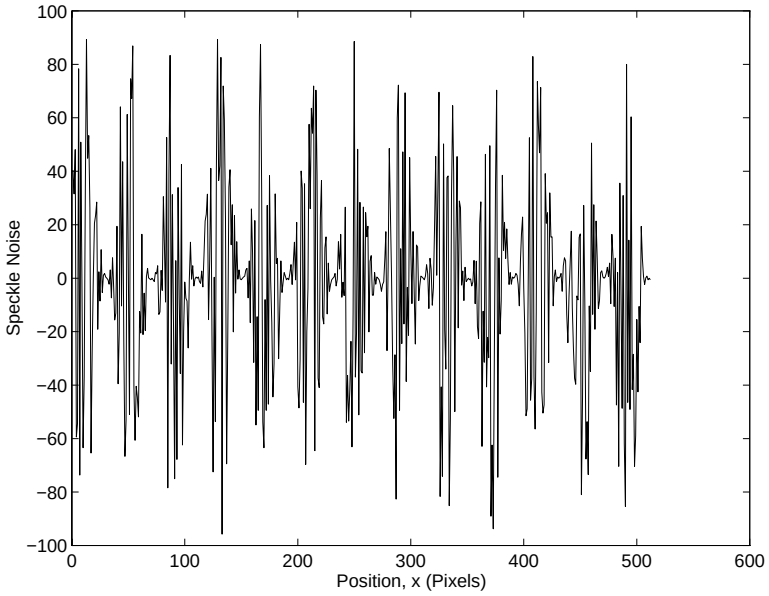

(b) Speckle noise from the fringe pattern with a phase shift of 90°

Figure 3.11: Speckle noise in row 1

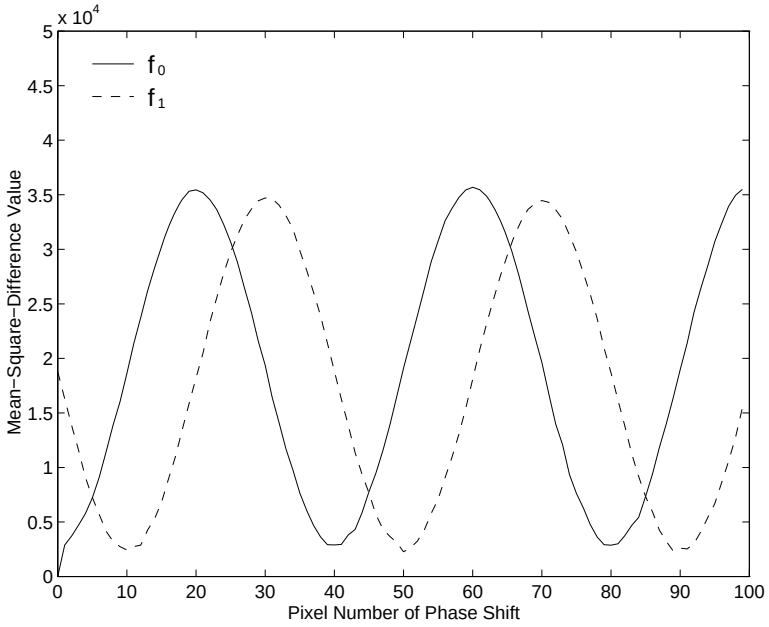

(a) Phase curves from 1×382 pixel image patches

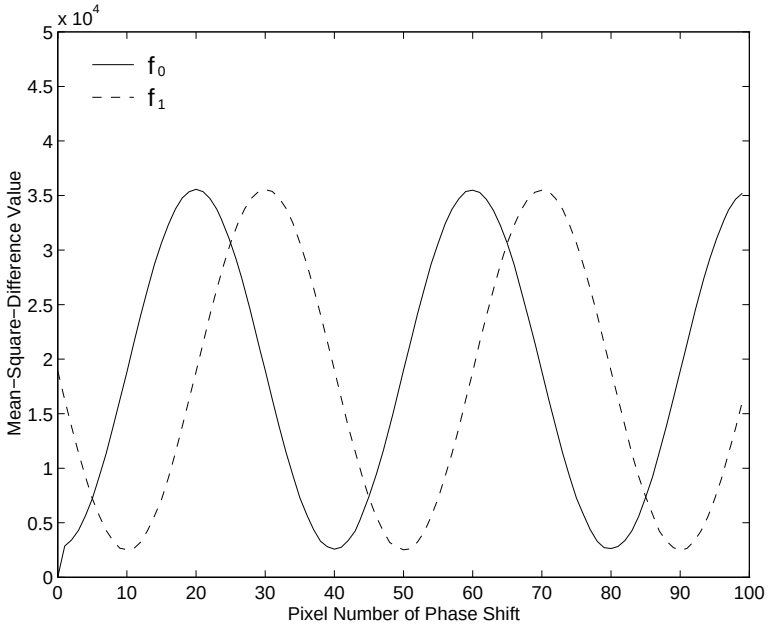

(b) Phase curves from 10×382 pixel image patches

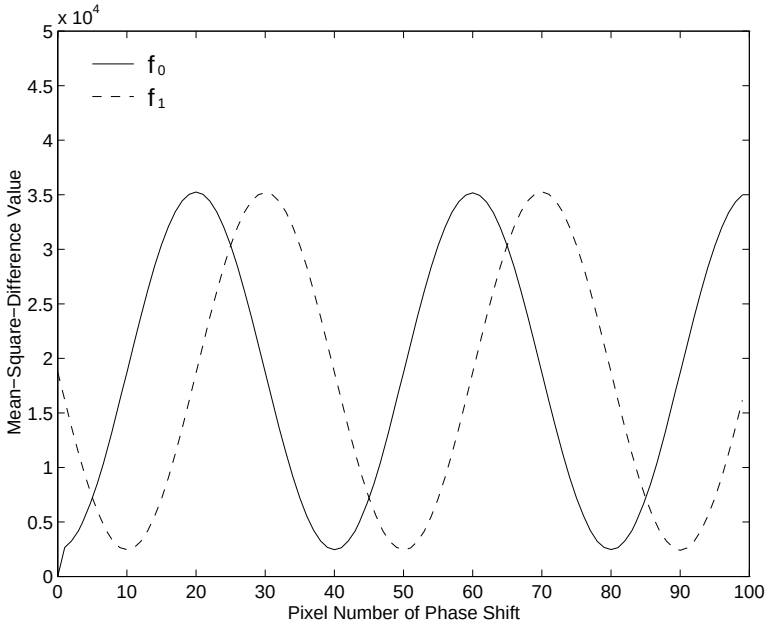

(c) Phase curves from 100×382 pixel image patches

Figure 3.12: Phase curves from the different sizes of image patches with speckle noise

Table 3.3: Computer simulation results from the fringe patterns with speckle noise

Size of image patch (pixels)	Mean (degrees)	Standard Deviation σ (degrees)	Standard Deviation σ_M (degrees)
1x382	89.9826	1.4283	1.4283
10x382	89.9418	0.4830	0.4517
100x382	89.9947	0.1430	0.1428

Number of Samples K=100

3.3.4 Fringe Patterns with the Combined Noise

In the presence of Gaussian noise, salt & pepper noise, and speckle noise, the effect of image patch size on phase difference determination by fringe pattern matching has been discussed separately. In practice, however, the noise effect is the combination of more than one type of noise. Therefore, the combinational effect of the three types of noise on the measurements made from the different sizes of image patches are also discussed in this section.

In the case that the effects of the three types of noise on phase difference measurement are independent, the standard deviation for the combined noise, σ_{combined}, can be then calculated by

$$\sigma_{\text{combined}} = \sqrt{\sigma^2_{\text{Gaussian}} + \sigma^2_{\text{salt\&pepper}} + \sigma^2_{\text{speckle}}} \tag{3.28}$$

where σ_{Gaussian} is the standard deviation obtained from the fringe patterns with Gaussian noise, $\sigma_{\text{salt\&pepper}}$ is that from the fringe patterns with salt & pepper noise, and σ_{speckle} is that from the fringe patterns with speckle noise.

In the simulation, the computer generated fringe patterns were 512× 512 pixel images with a phase difference of 90° and fringe period of 40 pixels, and their grey-level resolution was about 8 bits. The light intensity distributions of the fringe patterns were

$$I_0^{'}(i,j) = \text{round}[127.5 + 127.5\cos(\frac{\pi i}{20}) + \nu_0(i,j)] \tag{3.29}$$

and

$$I_m^{'}(i,j) = \text{round}[127.5 + 127.5\cos(\frac{\pi i}{20} - \frac{\pi}{2}) + \nu_m(i,j)] \tag{3.30}$$

where

$$\nu_0(i,j) = \nu_{0(\text{Gaussian})}(i,j) + \nu_{0(\text{salt\&pepper})}(i,j) + \nu_{0(\text{speckle})}(i,j) \tag{3.31}$$

and

$$\nu_m(i,j) = \nu_{m(\text{Gaussian})}(i,j) + \nu_{m(\text{salt\&pepper})}(i,j) + \nu_{m(\text{speckle})}(i,j) \tag{3.32}$$

In equations 3.29, 3.30, 3.31 and 3.32, m=1, 2, 3, ..., 100, i=0, 1, 2, ..., 511 and j=0, 1, 2, ..., 511. $\nu_0(i,j)$ and $\nu_m(i,j)$ are the combined noise distributions. The function round(x) rounds x to the nearest integer to obtain the quantised fringe pattern.

Figure 3.13 shows two computer generated fringe patterns with the combined noise. The light intensities in row 1 of the fringe patterns are shown in figure 3.14. Figure 3.15 shows the combined noise distribution in row 1, and figure 3.16 shows the phase curves acquired from the image patches of 1×382, 10×382 and

100×382 pixels.

In the simulation, one hundred pairs of image patches were used for the evaluation of the effect of image patch size on phase difference determination in the presence of the combined noise. The results achieved from the image patches of 1×382, 10×382 and 100×382 pixels, as shown in table 3.4, were 2.1831°, 0.7787° and 0.2182°. The results calculated from equation 3.14 were $\sigma_{10} \approx 0.6904°$ and $\sigma_{100} \approx 0.2183°$ when σ_1 was 2.1831°. The standard deviations calculated from equation 3.28 were 2.1853°, 0.6998° and 0.2040° for the image patches of 1×382, 10×382 and 100×382 pixels, respectively. The phase difference samples used in the simulation and the results are given in appendix C.4.

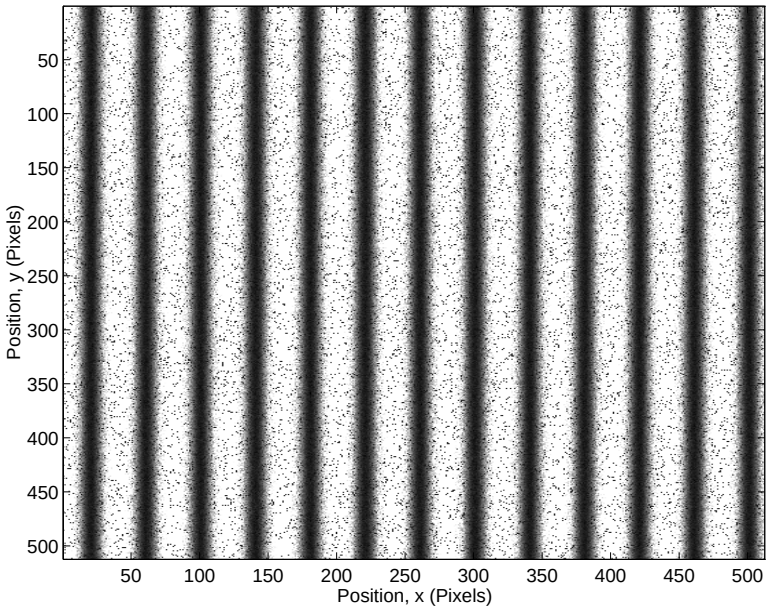

(a) Fringe pattern with a phase shift of 0°

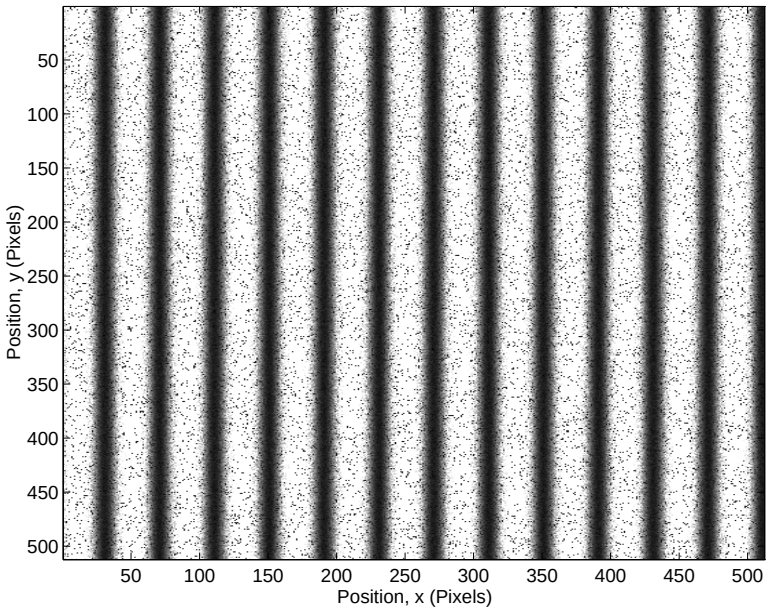

(b) Fringe pattern with a phase shift of 90°

Figure 3.13: Two computer generated fringe patterns with the combined noise

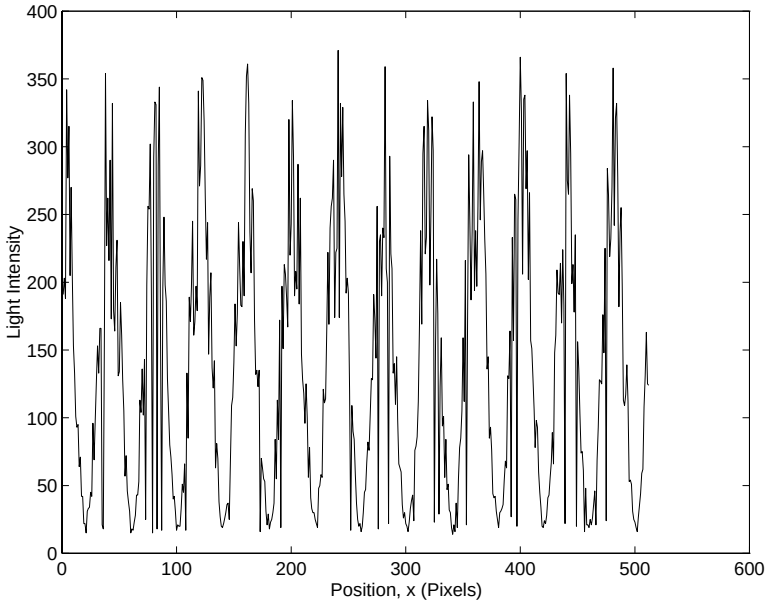

(a) Light intensity from the fringe pattern with a phase shift of 0°

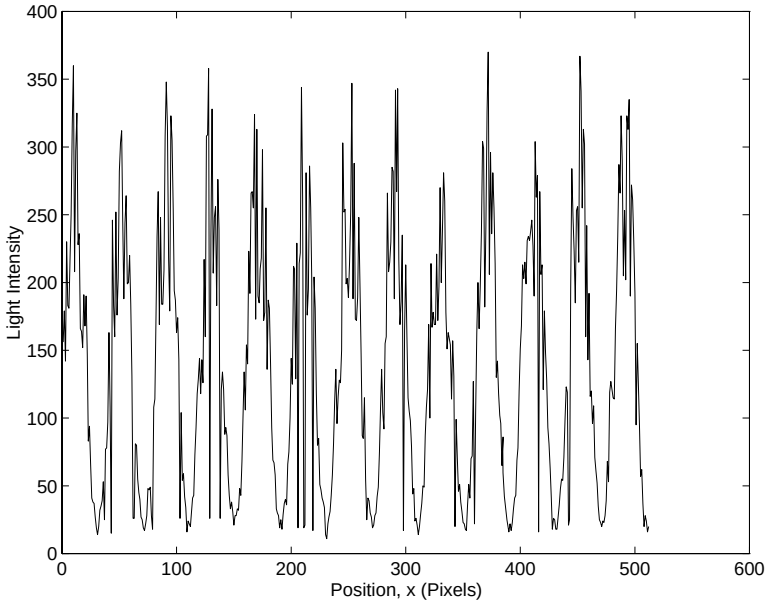

(b) Light intensity from the fringe pattern with a phase shift of 90°

Figure 3.14: Light intensities in row 1 from the fringe patterns with the combined noise

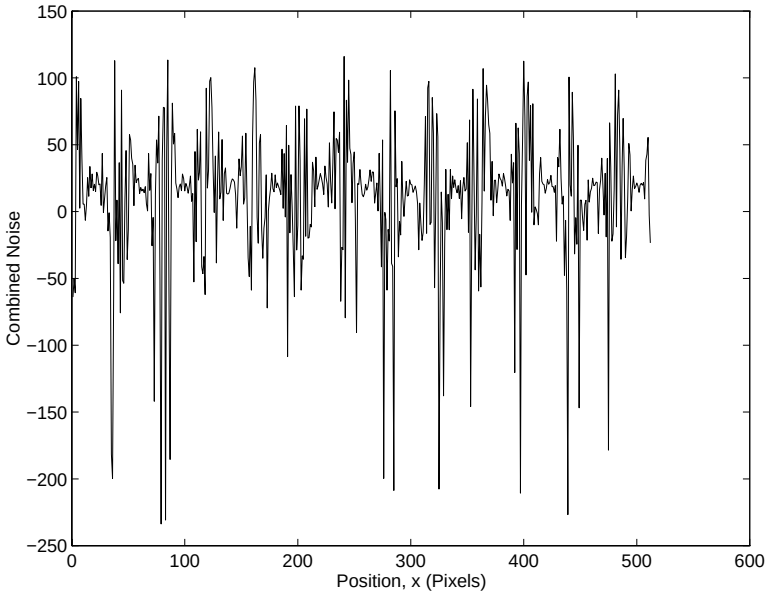

(a) The combined noise from the fringe pattern with a phase shift of 0°

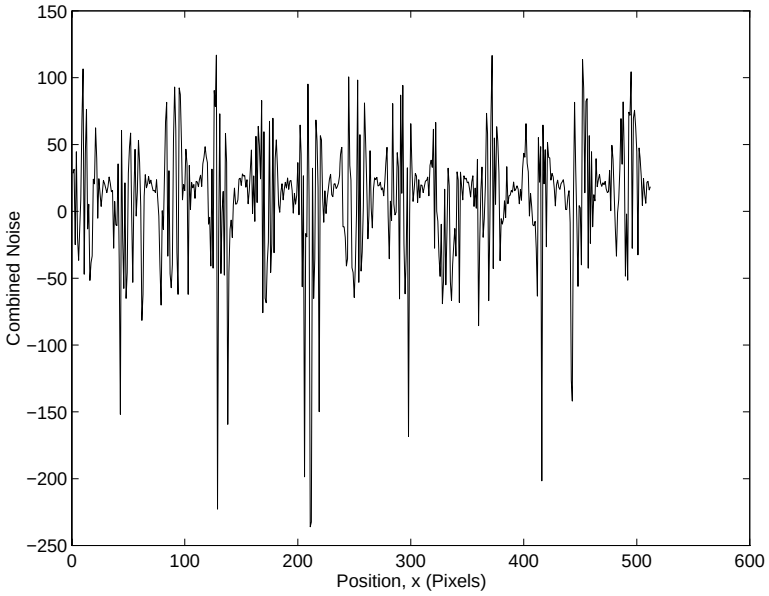

(b) The combined noise from the fringe pattern with a phase shift of 90°

Figure 3.15: The combined noise in row 1

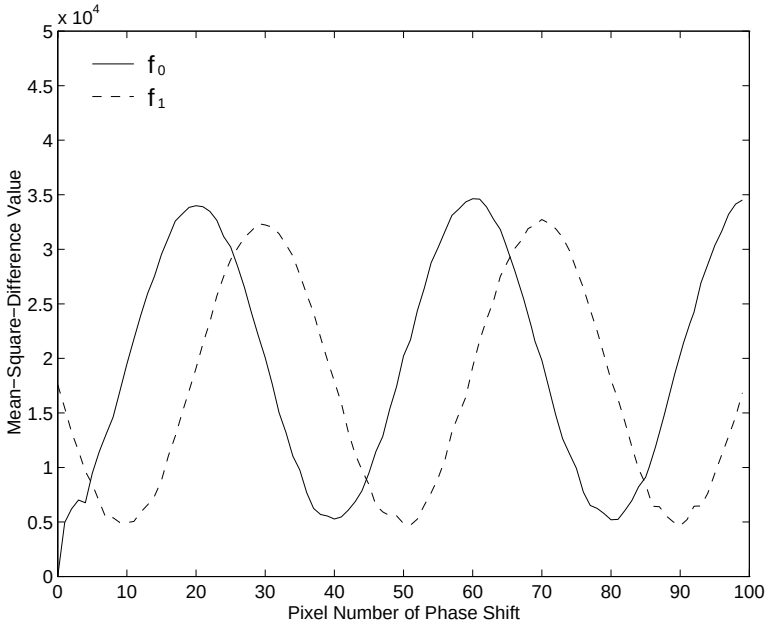

(a) Phase curves from 1×382 pixel image patches

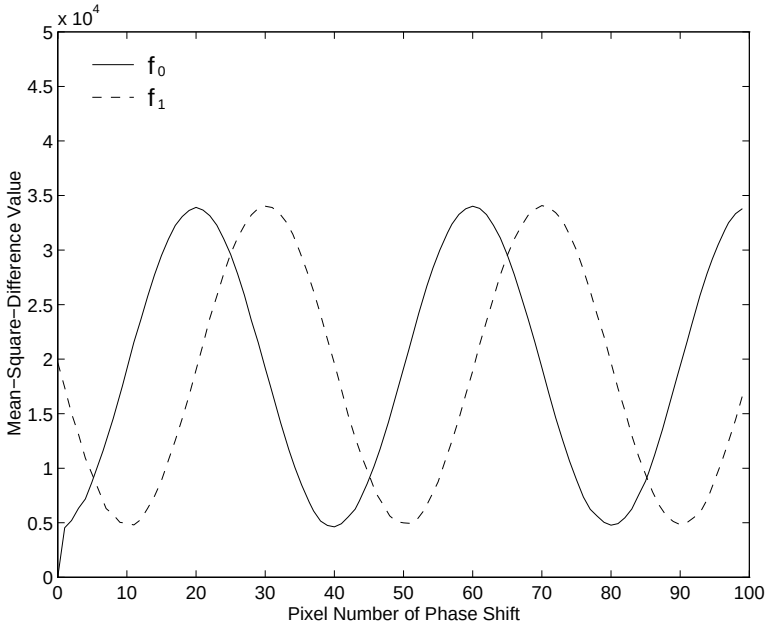

(b) Phase curves from 10×382 pixel image patches

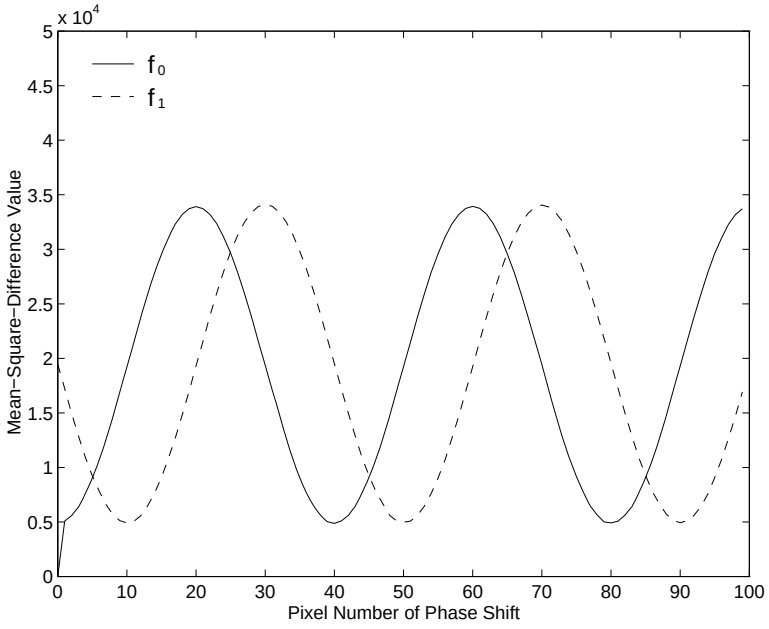

(c) Phase curves from 100×382 pixel image patches

Figure 3.16: Phase curves from the different sizes of image patches with the combined noise

Table 3.4: Computer simulation results from the fringe patterns with the combined noise

Size of image patch (pixels)	Mean (degrees)	Standard Deviation σ (degrees)	Standard Deviation σ_M (degrees)
1x382	90.1499	2.1831	2.1831
10x382	90.1309	0.7787	0.6904
100x382	89.9799	0.2182	0.2183

Number of Samples K=100

3.4 Experimental Results

The effect of image patch size on phase difference determination by fringe pattern matching was also examined in an experiment. One hundred pairs of interferograms, which were 512×512 pixel and 8-bit grey-level fringe patterns, were captured by CCD camera in the interferometer system for introducing phase shifts as shown in figure 2.5 in chapter 2. A phase difference of 90^o between each pair of fringe patterns was introduced by PZT (piezo-electric transducer) creating a displacement of a mirror. The wavelength of the He-Ne laser, employed in the experiment, was 0.6328 μm.

Figure 3.17 shows one pair of the fringe patterns with a phase difference of 90^o. The light intensities in row 1 of the fringe patterns are shown in figure 3.18. Figure 3.19 shows the phase curves acquired from the image patches of 1×382, 10×382 and 100×382 pixels.

The standard deviations achieved from the image patches of 1×382, 10×382 and 100×382 pixels, as shown in table 3.5, were 3.0139^o, 2.4184^o, and 1.4074^o. The results computed from equation 3.14 were $\sigma_{10} \approx 0.9531^o$ and $\sigma_{100} \approx 0.3014^o$ when σ_1 was 3.0139^o. The phase difference samples used in the calculation and the results are given in appendix C.5.

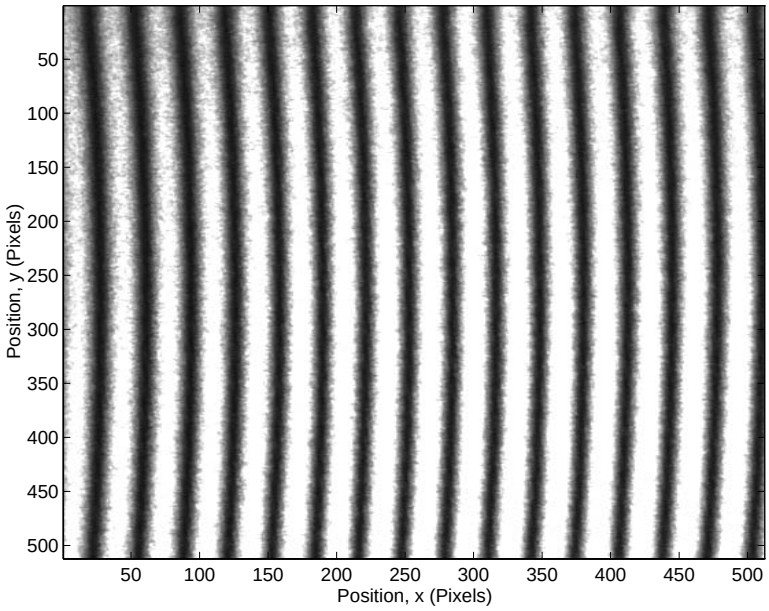

(a) Fringe pattern with a phase shift of 0°

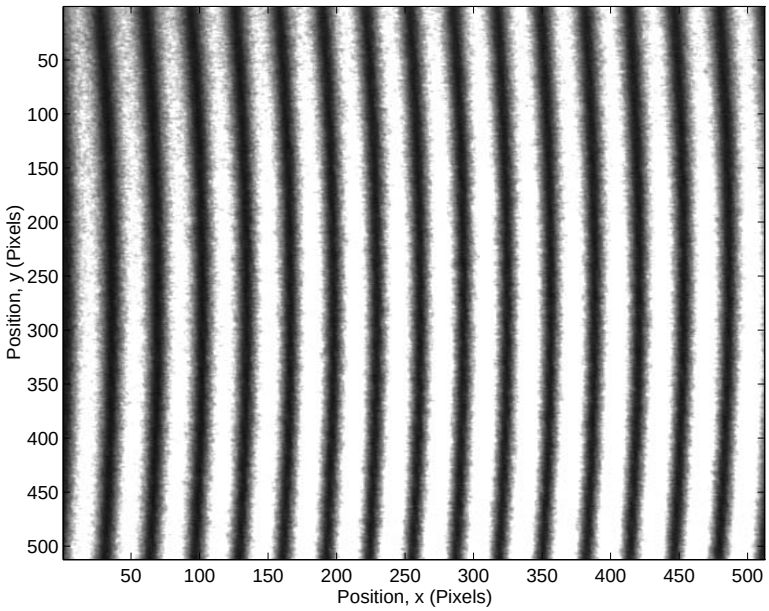

(b) Fringe pattern with a phase shift of 90°

Figure 3.17: Two captured fringe patterns with noise

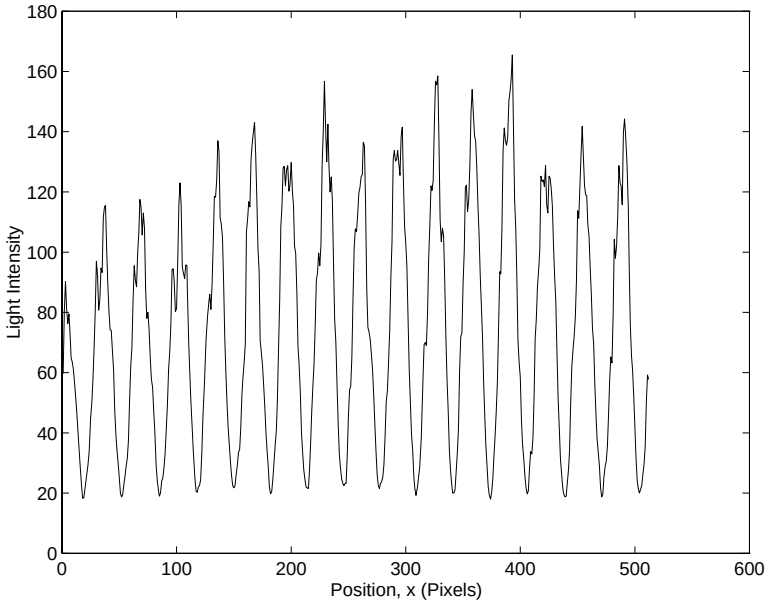

(a) Light intensity from the fringe pattern with a phase shift of 0°

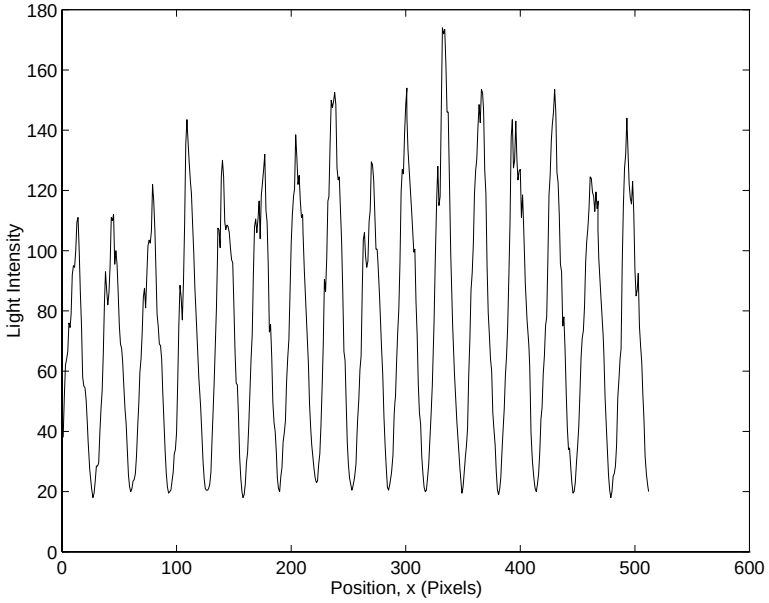

(b) Light intensity from the fringe pattern with a phase shift of 90°

Figure 3.18: Light intensities in row 1 from the two captured fringe patterns

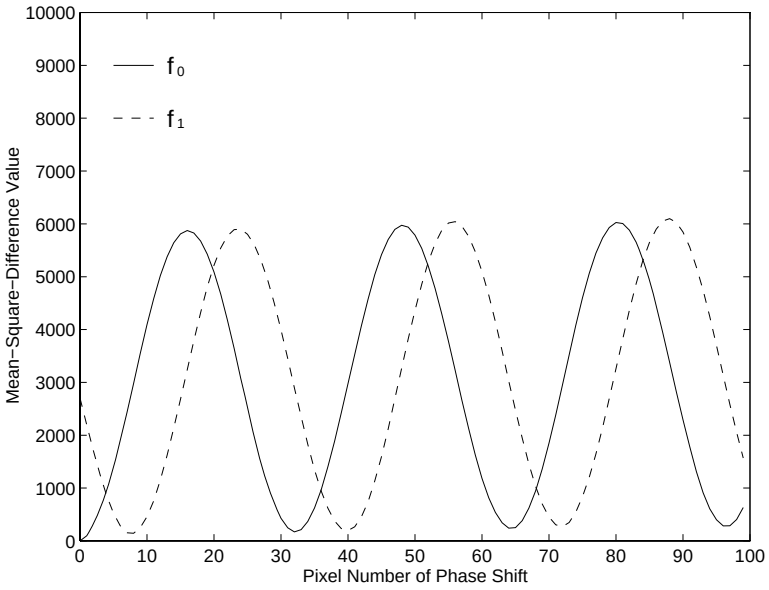

(a) Phase curves from 1×382 pixel image patches

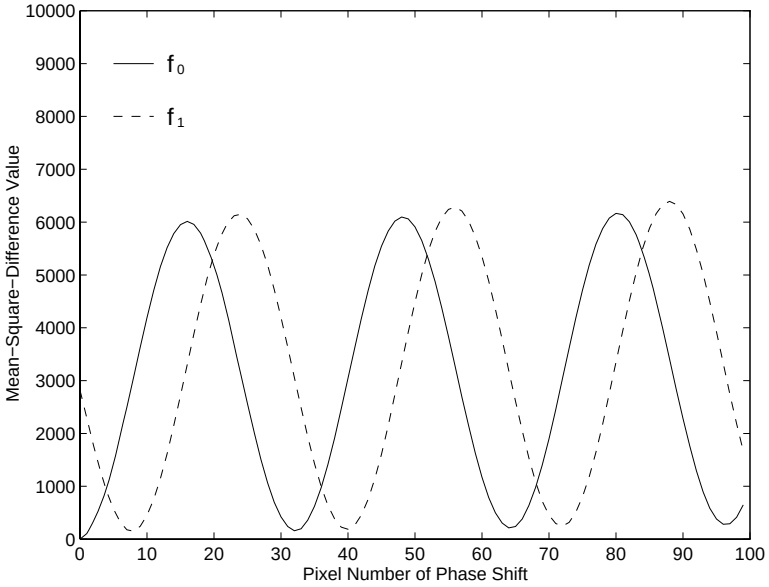

(b) Phase curves from 10×382 pixel image patches

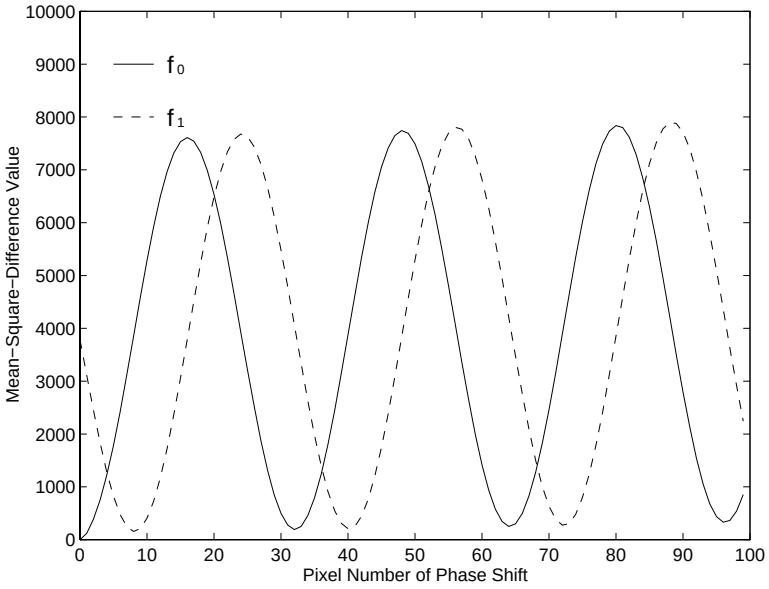

(c) Phase curves from 100×382 pixel image patches

Figure 3.19: Phase curves from the two captured fringe patterns

Table 3.5: Experimental results from the captured fringe patterns

Size of image patch (pixels)	Mean (degrees)	Standard Deviation σ (degrees)	Standard Deviation σ_M (degrees)
1x382	88.6223	3.0139	3.0139
10x382	89.3404	2.4184	0.9531
100x382	89.5313	1.4074	0.3014

Number of Samples K=100

3.5 Discussion

From the computer simulation and experimental results, it can be seen that the larger image patches used for the phase difference determination by fringe pattern matching have achieved a better accuracy in the presence of noise. This feature, which is clearly described by equations 3.14 and 3.21, is in effect based on the fact that the phase curves obtained from M×N pixel image patches can be considered as the superposition of M independent phase curves obtained from 1×N pixel image patches, or the superposition of M×N independent phase curves obtained from 1×1 pixel image patches.

In equations 3.14 and 3.21, the phase difference measurements made by fringe pattern matching are assumed to be uncorrelated in the calculations of the standard deviations based on one line and one pixel. For the practical measurements, that is not the exact case since the phase difference is affected not only by the intensity noise but also by other sources such as the limited imager resolutions, vibration, air turbulence, mechanical drift and thermal drift.

If ρ_1 is the correlation between the lines of image patches then the standard deviation expressed by equation 3.14 is degraded by the correlation, i.e.

$$\sigma_{\mathrm{M}} = \frac{\sigma_1}{\sqrt{\mathrm{M}}}\sqrt{1 + (\mathrm{M}-1)\rho_1}, \quad 0 \leq \rho_1 \leq 1 \tag{3.33}$$

In the same way, for the measurements based on one pixel, the standard deviation is

$$\sigma_{\mathrm{M}} = \frac{\sigma_0}{\sqrt{\mathrm{M}\times\mathrm{N}}}\sqrt{1 + (\mathrm{M}\times\mathrm{N}-1)\rho_0}, \quad 0 \leq \rho_0 \leq 1 \tag{3.34}$$

where ρ_0 is the correlation between the pixels of image patches in the determination of phase difference by fringe pattern matching. In the simulation, the

correlation calculated from the image patches of 1×382 and 10×382 pixels was less than 0.04, and that from the image patches of 1×382 and 100×382 pixels was less than 0.002. In the experiment, the correlation computed from the image patches of 1×382 and 10×382 pixels was 0.60, and that from the image patches of 1×382 and 100×382 pixels was 0.21.

In addition, it should be noted that the expected accuracy of phase difference measurement cannot be achieved by simply increasing the size of image patches used in the matching process since the accuracy, in practice, is also influenced by other factors such as the resolution of imaging sensor and unequally spaced fringes due to the optical aberrations and misalignments. Therefore, the achievable accuracy in the determination of phase difference by fringe pattern matching is basically dependent on the quality of fringe patterns although it has the advantage of high tolerance to noise.

3.6 Conclusion

The computer simulation and experimental results have proved that the larger image patches used in the determination of phase difference by fringe pattern matching have a better accuracy in the presence of noise, which is in accordance with the theoretical results described by equations 3.14 and 3.21. The signal to noise ratio of the fringe patterns in the measurement is significantly improved due to the fact that each value of the mismatch function is obtained from averaging M×N pixels if the image patches with the size of M×N pixels are used in the matching process. The advantage of averaging noise of fringe pattern matching method makes it powerful in the determination of phase difference from noise fringe patterns.

Bibliography

[1] Y. Nishida, J. Koike, H. Ohtake, M. Abe, and S. Yoshikawa, "Design concept for a low-noise CCD image sensor based on subjective evaluation," *IEEE Trans. Electron Devices* **36**(2), 360-366 (1989).

[2] D.S. Snyder and A.M. Hammoud, "Image recovery from data acquired with a charge-coupled-device camera," *J. Opt. Soc. Am. A* **10**(5), 1014-1023 (1993).

[3] M. Chen and Y. Lin, "Gaussian threshold for high fidelity of digital wavefront reconstruction," *Proc. SPIE* **2003**, 348-354 (1993).

[4] K.R. Castleman, *Digital image processing,* Prentice-Hall, Englewood Cliffs and London (1979).

[5] R. Jones, *Holographic and speckle interferometry,* Cambridge University Press, Cambridge (1989).

[6] M.K. Steven, *Fundamentals of statistical signal processing, estimation theory,* Prentice-Hall International Ltd., London (1993).

[7] A. Novini, "Fundamentals of on-line gauging for machine vision," *Proc. SPIE* **1395**, 736-746 (1990).

[8] J.F.W. Galyer and C.R. Shotbolt, *Metrology for engineers,* Cassell, London (1990).

[9] A. Athanasios, *Probability, random variables, and stochastic processes,*

McGraw-Hill, New York, London (1965).

[10] R. Jain, R. Kasturi, and B.G. Schunck, *Machine vision,* McGraw-Hill, New York & London (1995).

[11] C.M. Thompson and L. Shure, *Image processing toolbox user's guide,* The Math Works, Mass. (1995).

[12] H. Kadono and S. Toyooka, "Statistical interferometry based on the statistics of speckle phase," *Opt. Letters* **16**(12), 883-885 (1991).

Chapter 4

Measurement of Electrostatic Force Displacement

4.1 Introduction

The laser interferometer has proved to be a powerful tool for high precision measurement of displacement in terms of the wavelength of light. It is now known that the conventional techniques such as fringe counting [1, 2, 3], heterodyning [4, 5, 6, 7], and homodyning [8, 9, 10] have the disadvantage of using only a small part of the fringe pattern to obtain the displacement information, and their accuracies are easily affected by the fringes with background noise levels.

In this chapter, the technique of fringe pattern matching [12, 12, 13, 14] is used to achieve the displacement information between any two fringe patterns. The measurement of electrostatic force displacement was investigated in a fibre-optic interferometer system. In the experiment, the quality of the fringe pattern was badly affected by the non-ideal optical surface of the cantilever of the capacitive sensor from which several hundreds of noisy interferograms were obtained. Fringe pattern matching was then used for detecting the displacement information from the hundreds of noisy interferograms. The signal to noise ratio in the

measurement was significantly improved by the matching process. A resolution of 1/182 wavelength was achieved from the noisy interferograms using fringe pattern matching together with linear interpolation.

In section 4.2 of this chapter, the principle of the measurement of electrostatic force displacement using an interferometer is introduced. Section 4.3 describes the experimental set-up of the fibre-optic interferometer system and section 4.3 illustrates the experimental results. The discussion and conclusion are given in sections 4.4 and 4.5.

4.2 Principle

A capacitive sensor for detecting electrostatic force displacement is shown in figure 4.1. The two capacitance electrodes are formed on the surfaces of the cantilever and the base. When a dc voltage is applied across the two parallel electrodes, it produces an attractive force between the electrodes and a displacement of the cantilever [15, 16, 17].

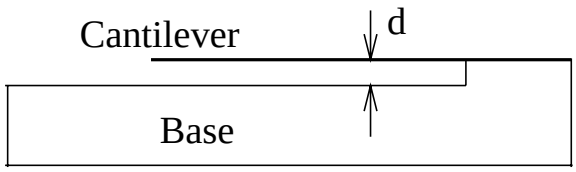

Figure 4.1: Capacitive sensor for detecting electrostatic force displacement

The relationship between the displacement of the cantilever and the voltage across the electrodes is given by [15, 16, 17]

$$\Delta d = \frac{k_1 V^2}{d^2} \tag{4.1}$$

where Δd is the displacement of the cantilever, V is the voltage across the electrodes, d is the distance between the two capacitor plates, and k_1 is a constant.

Figure 4.2 shows the schematic of measuring the displacement of the cantilever of the capacitive sensor using an interferometer system. The displacement of the cantilever varies with the voltage across the electrodes, and at the same time the displacement gives rise to the optical path difference and the interference pattern with a phase shift. Assuming that the displacement is very small in comparison with the length of the cantilever, the bending angle of the cantilever can be neglected in the calculation of displacement. Figure 4.3 shows the principle of calculating the optical path difference.

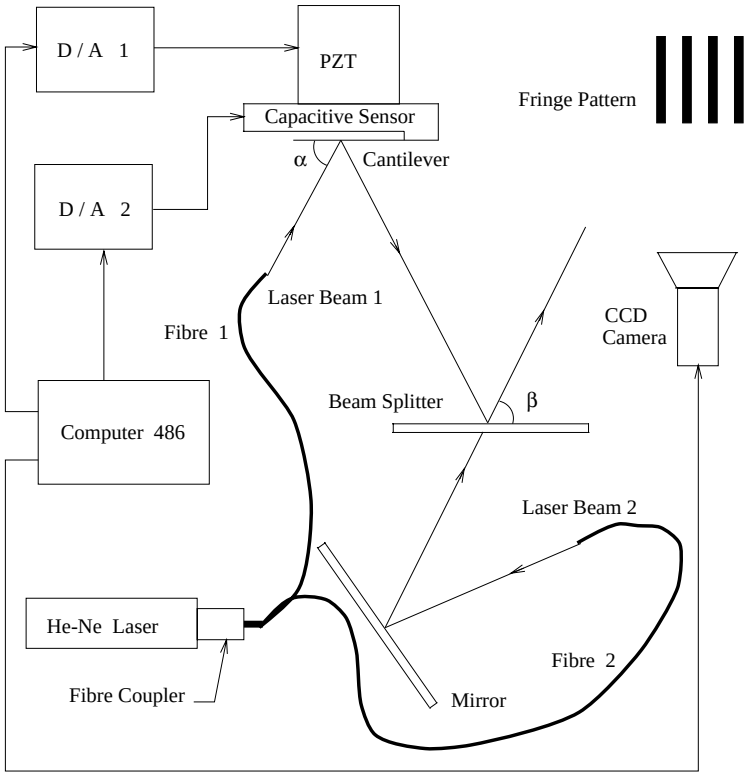

Figure 4.2: Schematic of measuring the displacement of the cantilever using an interferometer system

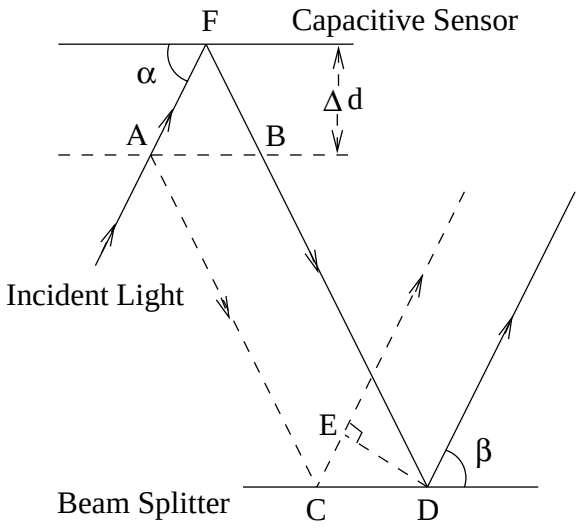

Figure 4.3: Calculation of the optical path difference

In figure 4.3, the optical path difference ΔL can be calculated by

$$\Delta L = (AF + FB + BD) - (AC + CE) \tag{4.2}$$

Since AF=FB and BD=AC, equation 4.2 can be simplified as

$$\Delta L = 2AF - CE \tag{4.3}$$

where

$$AF = \frac{\Delta d}{\sin \alpha} \tag{4.4}$$

and

$$CE = CD \cos \beta = AB \cos \beta = \frac{2\Delta d \cos \beta}{\tan \alpha} \tag{4.5}$$

If $\alpha = \beta$, equation 4.5 can be expressed as

$$CE = \frac{2\Delta d \cos^2 \alpha}{\sin \alpha} \tag{4.6}$$

By substituting AF and CE into equation 4.3, the optical path difference ΔL can be obtained, that is

$$\Delta \mathrm{L} = 2\Delta \mathrm{d} \sin \alpha \tag{4.7}$$

The phase difference $\Delta\phi$ can be therefore expressed as

$$\Delta\phi = \frac{4\pi\Delta \mathrm{d} \sin \alpha}{\lambda} \tag{4.8}$$

and the displacement of the cantilever in one fringe period can be calculated by

$$\Delta \mathrm{d} = \frac{\Delta\phi\lambda}{4\pi \sin \alpha} \tag{4.9}$$

where Δd is the displacement, $\Delta\phi$ is the phase difference, α is the angle between the incident laser beam and the cantilever surface, and λ is the wavelength of light.

Figure 4.4 shows the method of calculating the phase shift from the relationship between the two fringe patterns. In the figure, P is the fringe period and x is the shift distance of the fringe. The phase difference $\Delta\phi$ in this case can be computed by

$$\Delta\phi = \frac{2\pi \mathrm{x}}{\mathrm{P}} \tag{4.10}$$

Since equations 4.8 and 4.10 express the same phase difference, the following equation is obtained, i.e.

$$\frac{4\pi\Delta \mathrm{d} \sin \alpha}{\lambda} = \frac{2\pi \mathrm{x}}{\mathrm{P}} \tag{4.11}$$

As such the displacement of the cantilever in one fringe period can also be calculated by

$$\Delta \mathrm{d} = \frac{\lambda \mathrm{x}}{2\mathrm{P} \sin \alpha} \tag{4.12}$$

It can be seen from equations 4.9 and 4.12 that the displacement of the cantilever Δd is a function of the phase shift distance x and the fringe period P, or the phase

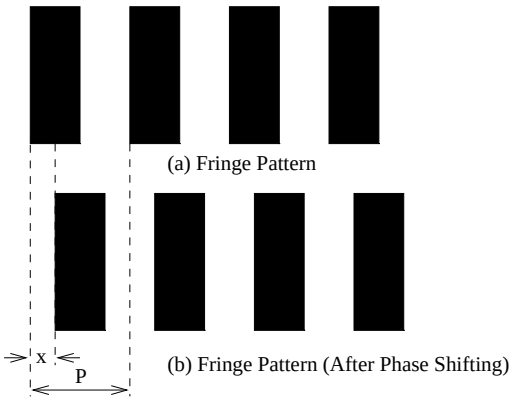

Figure 4.4: Determination of the phase shift

difference $\Delta\phi$. Therefore, fringe pattern matching can be used to determine the phase difference and the displacement of the cantilever of the capacitive sensor.

The principle of fringe pattern matching and the methods for achieving subpixel resolution have been described in detail in chapter 2. The procedure of measuring displacement by fringe pattern matching can be summarised as follows:

• Capture interferograms in sequence, and take the first as a reference fringe pattern for the matching.

• Select equation 2.9 or equation 2.10 as the mismatch function according to the fringe shifting direction. Use equation 2.9 for the fringes shifted in the left direction, and equation 2.10 for the fringes shifted in the right direction, assuming that the fringes are vertical in the fringe patterns.

• Choose a fixed image patch in the first fringe pattern as a reference image patch, and a shifted image patch in another fringe pattern with the same size as the reference image patch for the matching.

• Compute the mean-square-difference values for each shift to obtain the phase curves with the phase difference between the fringe patterns.

• Calculate the phase difference from the phase curves. Subpixel accuracy may be achieved by linear interpolation or polynomial curve fitting .

• Find the actual displacement on the basis of the relationship between the phase

difference and the displacement as described by equations 4.9 and 4.12. The calibration of measurement is normally needed to reduce or suppress systematic errors for high precision measurement.

• The periodic constant must be added in the measurement if the phase shift is larger than one fringe period.

4.3 Experimentation

In this section, the experimental set-up of the fibre-optic interferometer system for measuring electrostatic force displacement of a capacitive sensor is described. The fibre-optic interferometer is suitable for the measurement because of the small surface area of the cantilever and high resolution required. The experimental results are given on the basis of the measurement made by fringe pattern matching together with linear interpolation.

4.3.1 Experimental Set-up

The experimental set-up of the fibre-optic interferometer system for measuring electrostatic force displacement of a capacitive sensor is shown in figure 4.2. In the set-up, the cantilever of the capacitive sensor in the experiment had a surface area of 15×2 mm^2. The distance between the cantilever and the base of the capacitive sensor was about 10μm. The wavelength of the 15-mw He-Ne laser used in the experimental set-up was 0.6328 μm.

In the experiment, the PZT (piezo-electric transducer) with a resolution of 1 nm was used for the calibration of measurement, and the capacitive sensor was mounted on the PZT to reduce or suppress the systematic error and the error from miscalibration. The displacements of the PZT and the cantilever of the capacitive sensor were controlled by the 486 computer with the two 12-bit digital to analogue

converters D/A 1 and D/A 2. The computer was programmed to output the voltages needed for the calibration and the displacements of the cantilever of the capacitive sensor through the two D/A converters and capture fringe patterns automatically to minimise the errors from the fringe drift and vibration during the measurement.

4.3.2 Experimental Results

In the measurement, the quality of the interferometric image was badly affected by the non-ideal optical surface of the cantilever of the capacitive sensor from which several hundreds of noisy interferograms were captured. The interferograms captured in sequence in the experiment were 8-bit grey-level images with the size of 512×512 pixels.

Figure 4.5 shows three of the noisy interferograms, and the light intensities from row 255 of the noisy interferograms are shown in figure 4.6. The phase curves shown in figure 4.7 have a clear picture of phase differences among the three fringe patterns although the noise can be seen clearly from the intensity distributions in figure 4.5 and figure 4.6. Figure 4.8 shows the experimental result which is a good fit with the theoretical result calculated from equation 4.1. In figure 4.8, the theoretical result is plotted as the solid line, and the experimental result is plotted as the circle line.

In the measurement, the reference and shifted image patches with the size of 100×252 pixels were used for the calculations of mean-square-difference to obtain the phase curves. The displacements after calibration were obtained from the relationship between the phase difference and the displacement of the cantilever described by equation 4.12. A resolution of 1/182 wavelength was achieved from 250 noisy interferograms using fringe pattern matching together with linear interpolation.

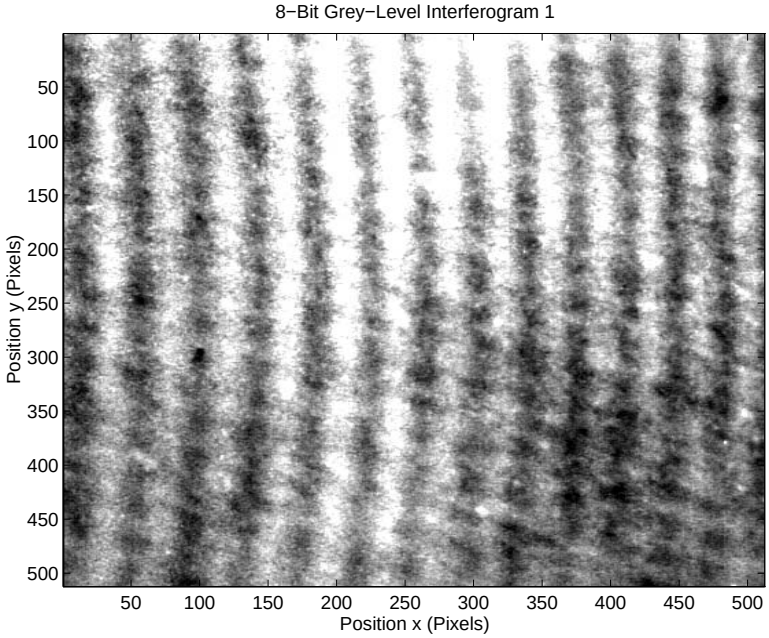

(a) Interferogram 1

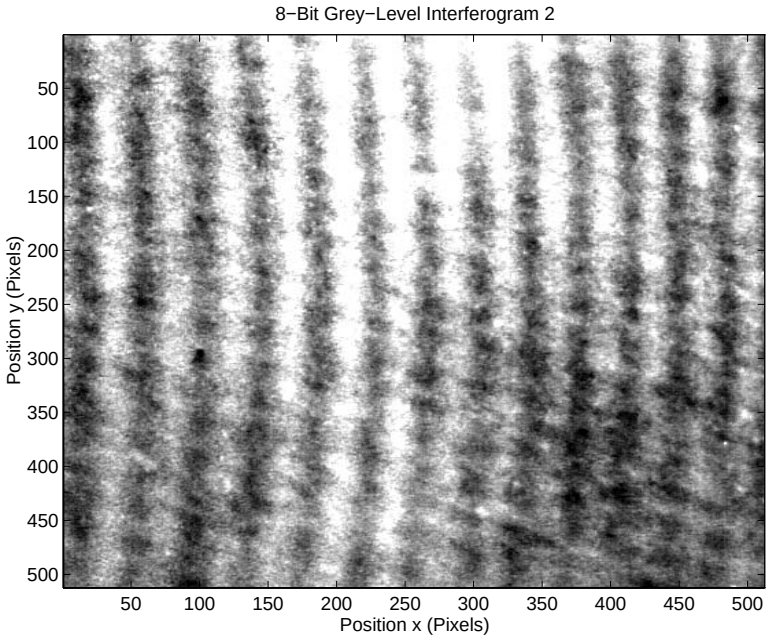

(b) Interferogram 2

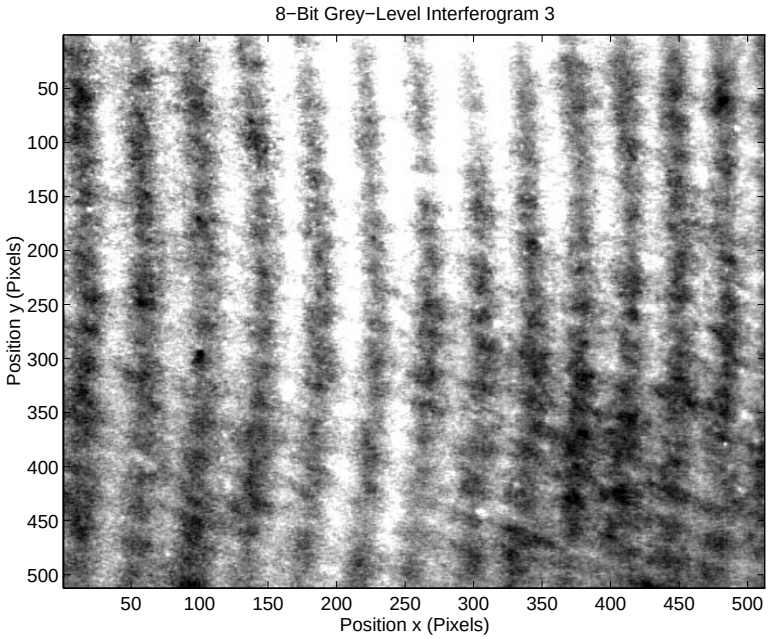

(c) Interferogram 3

Figure 4.5: Three interferograms with 512×512 pixels

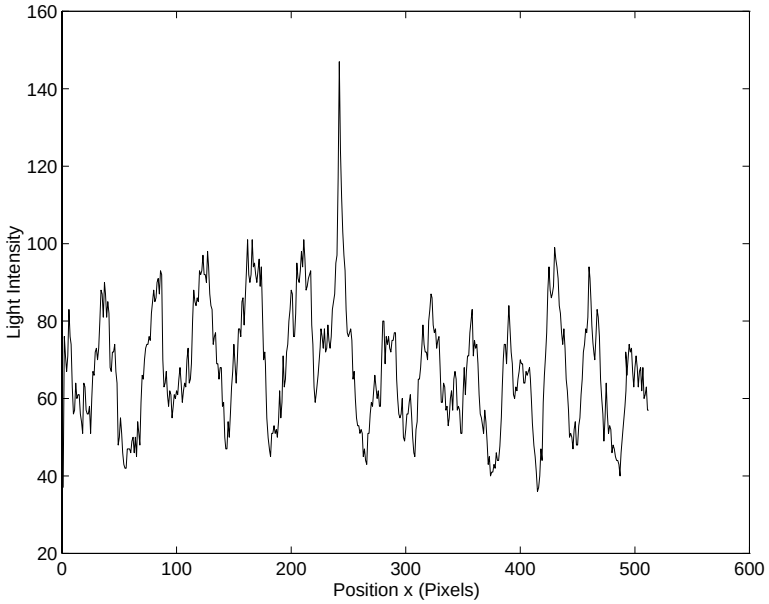

(a) Light intensity in row 255 of interferogram 1

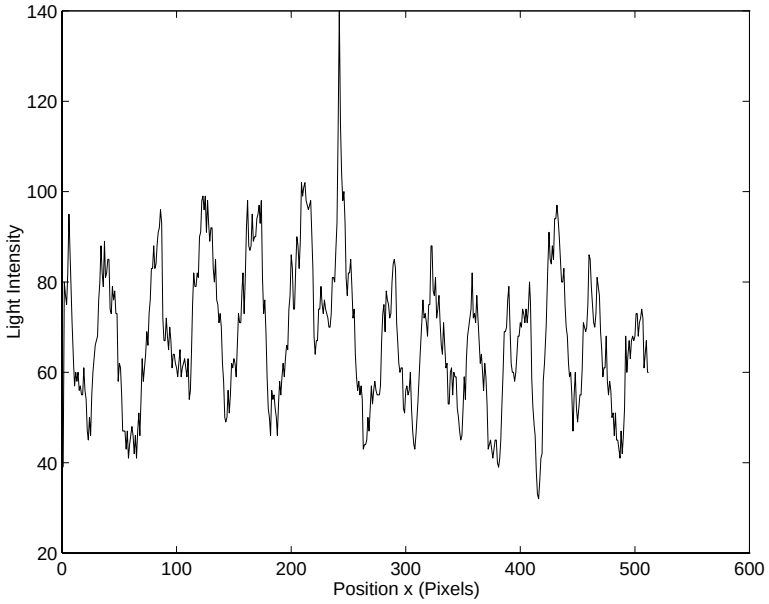

(b) Light intensity in row 255 of interferogram 2

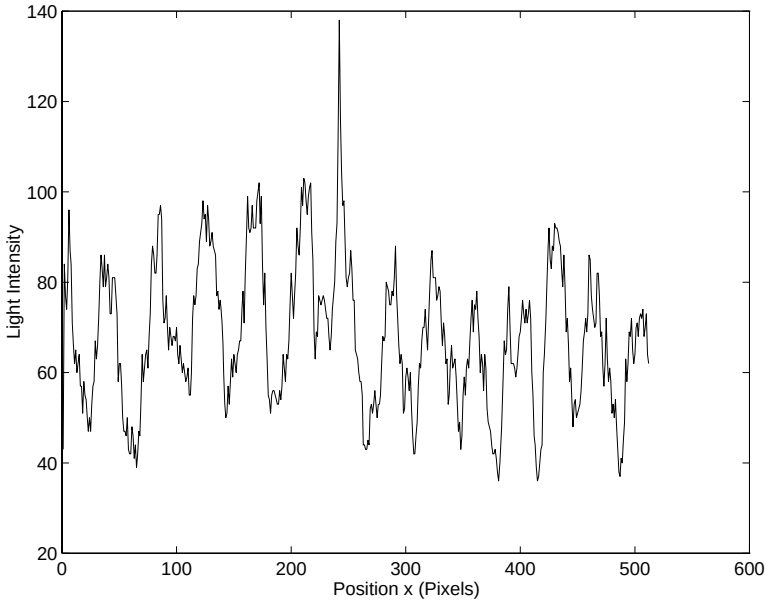

(c) Light intensity in row 255 of interferogram 3

Figure 4.6: Light intensity distributions in row 255 of the three interferograms

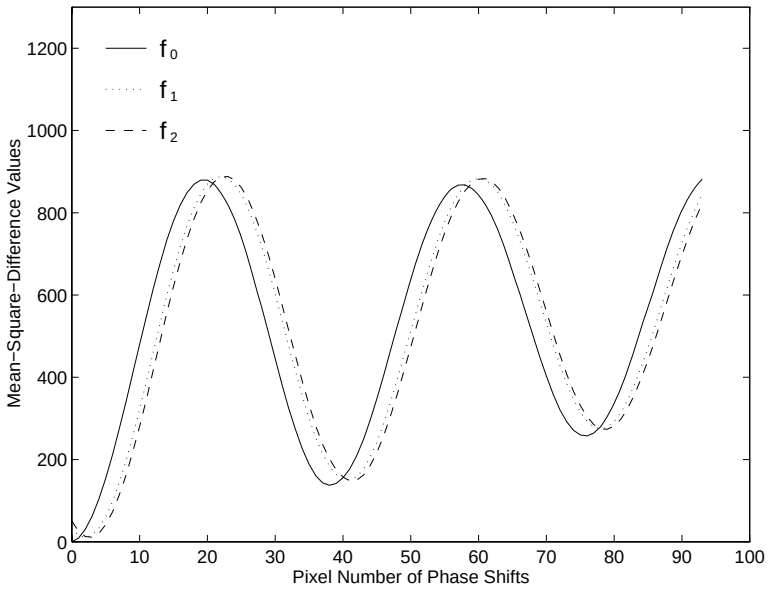

Figure 4.7: Phase curves with phase differences

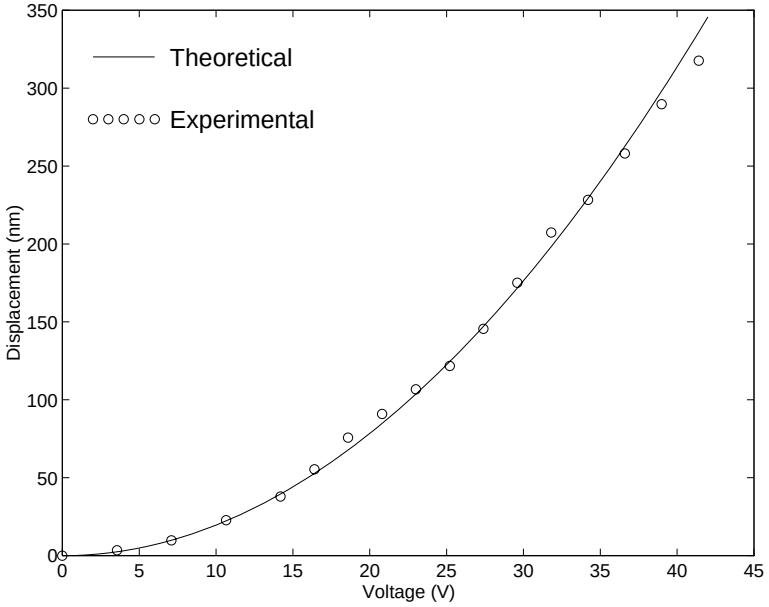

Figure 4.8: Theoretical and experimental results

4.4 Discussion

It can be seen clearly from figures 4.5 and 4.6 that the fringe patterns are corrupted by noise mainly arising from the non-ideal optical surface of the cantilever of the capacitive sensor. Figure 4.7 shows that the signal to noise ratio is significantly improved by fringe pattern matching. This indicates that fringe pattern matching is powerful in its practical use for the measurement of displacement from noisy interferograms.

In figure 4.2, the PZT is used for calibrating the interferometer through outputting a known displacement which is then measured by the interferometer to reduce or suppress the systematic error and the error from miscalibration. The calibration based on the experimental set-up can theoretically suppress the systematic error if the displacement direction of the cantilever is the same as that of the PZT. Therefore, the calibration method is useful for minimising the measurement error.

For the reduction of the effect of vibration the fibre-optic interferometer system was constructed on an optical breadboard, and the optical breadboard was placed on the optical bench with pneumatic vibration isolation supports in a basement laboratory. In addition all the measurements were performed after working hours to weaken the influences of the vibrations from traffic, machinery and human activity.

4.5 Conclusion

The displacement measurement made by fringe pattern matching in this chapter is a region-based measurement, so that it contains more accurate information of displacement compared with the conventional techniques that employ only a small part of the fringe pattern for measurement. The experiment has shown

that fringe pattern matching is effective in displacement measurement. The high precision measurement of displacement from the noisy interferograms is achieved due to the region-based measurement and its effect of averaging noise. The experimental results also indicate that the advantage of high resistance to noise makes fringe pattern matching powerful for displacement measurement in the presence of noise.

Bibliography

[1] M.J. Downs and K.W. Raine, "An unmodulated bi-directional fringe-counting interferometer system for measuring displacement," *Precision Eng.* **1**, 85-88 (1979).

[2] N. Hagiwara, Y. Nishitani, M. Yanase, and T. Saegusa, "A phase encoding method for improving the resolution and reliability of laser interferometers," *IEEE Trans. Instrum. Meas.* **38**(2), 548-551 (1989).

[3] S. Hosoe, "Laser interferometric system for displacement measurement with high precision," *Nanotechnology* **2**, 88-95 (1991).

[4] Y. Martin, C.C. Williams, and H.K. Wickramasinghe, "Atomic force microscope-force mapping and profiling on a sub 100-$\mathring{A}$ scale," *J. Appl. Phys.* **61**(10), 4723-4729 (1987).

[5] P.G. Charette, I.W. Hunter, and C.J.H. Brenan, "A complete high performance heterodyne interferometer displacement transducer for microactuator control," *Rev. Sci. Instrum.* **63**(1), 241-248 (1992).

[6] M. Sasaki, K. Hane, S. Okuma, M. Hino, and Y. Bessho, "Improved differential heterodyne interferometer for atomic force microscopy," *Rev. Sci. Instrum.* **65**(12), 3697-3701 (1994).

[7] J. Schneir, T.H. McWaid, J. Alexander, and B.P. Wilfley, "Design of an atomic force microscope with interferometric position control," *J. Vac. Sci.*

Technol. B **12**(6), 3561-3566 (1994).

[8] D. Rugar, H.J. Mamin, R. Erlandsson, J.E. Stern, and B.D. Terris, "Force microscope using a fiber-optic displacement sensor," *Rev. Sci. Instrum.* **59**(11), 2337-2340 (1988).

[9] C. Schonenberger and S.F. Alarado, "A differential interferometer for force microscopy," *Rev. Sci. Instrum.* **60**(10), 3131-3134 (1989).

[10] D. Rugar, H.J. Mamin, and P. Guethner, "Improve fiber-optic interferometer for atomic force microscopy," *Appl. Phys. Lett.* **55**(25), 2588-2590 (1989).

[11] A. Goshtasby, G.C. Stockman, and C.V. Page "A region-based approach to digital image registration with subpixel accuracy," *IEEE Trans. Geoscience and Remote Sensing* **GE-24**(3), 390-399 (1986).

[12] A. Kashko, H. Buxton, B.F. Buxton, and D.A. Castelow, "Parallel matching and reconstruction algorithms in computer vision," *Parallel Computing* **8**(1-3), 3-17 (1988).

[13] G. He and K. Novak, "On line data capture by image matching on the mobile mapping system," *Proc. SPIE* **1820**, 50-56 (1992).

[14] A. Gruen and D. Stallmann, "High-accuracy matching of object edges," *Proc. SPIE* **1820**, 70-82 (1992).

[15] W.S.N. Trimmer and K.J. Gabriel, "Design considerations for a practical electrostatic micro-motor," *Sensors and Actuators* **11**, 189-206 (1987).

[16] G. Neubauer, S.R. Cohen, G.M. McClelland, D. Horne, and C.M. Mate, "Force microscopy with a bidirectional capacitance sensor," *Rev. Sci. Instrum.* **61**(9), 2296-2307 (1990).

[17] D. Bosch, B. Heimhofer, G.Muck, H. Seidel, U. Thumser, and W. Welser, "A silicon microvalve with combined electromagnetic/electrostatic actuation," *Sensors and Actuators A* **37-38**, 684-692 (1993).

Chapter 5

Displacement Measurement Based on Young's Experiment

5.1 Introduction

The high precision measurement of displacement made by optical interferometry is often based on the changes of optical path length [1, 2, 3, 4, 5, 6, 7, 8, 9, 10, 11, 12] and it is very sensitive to its working environments. Therefore, unlike some other techniques, for example, optical triangulations [13, 14, 15, 16], it is not suitable for the measurement of displacement over a long distance.

In this chapter, a method of displacement measurement based on Young's experiment is presented. In the method, fringe pattern matching is used for directly measuring the fringe spacing from interferograms, and the displacement is then determined according to the fringe spacing equation derived from Young's experiment. The method was examined in a fibre-optic interferometer system, and the fringe spacing with subpixel accuracy was achieved from fringe pattern matching together with linear interpolation. The effect of imager resolutions on the accuracy of displacement measurement was also investigated by computer simulation.

In section 5.2 of this chapter, the principle of displacement measurement based on Young's experiment is introduced. Section 5.3 illustrates the experimental results, and the effect of imager resolutions on the accuracy of displacement measurement is discussed in section 5.4. The discussion and conclusion are given in section 5.5 and section 5.6.

5.2 Principle

Figure 5.1 shows the schematic of Young's experiment in which the two slits have been replaced by two fibres [17, 18].

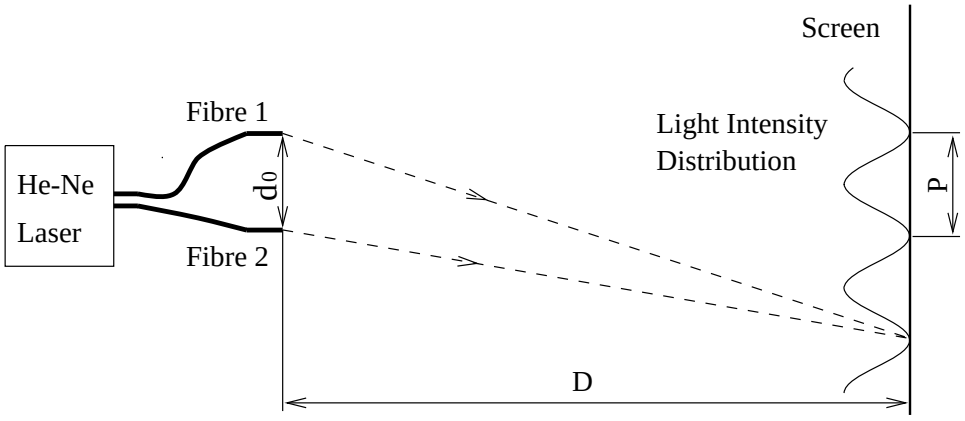

Figure 5.1: Schematic of Young's experiment for displacement measurement

In figure 5.1, if the distance between the screen and the fibres D is considerably greater than the distance between the two fibres d_0, the distance D, as discussed in chapter 1, can be expressed as

$$D = \frac{d_0 P}{\lambda} \tag{5.1}$$

Equation 5.1 indicates that the distance D is proportional to the fringe spacing P when the wavelength λ and the distance between the two fibres d_0 are in constant.

Therefore, the relative displacement ΔD can be calculated using

$$\Delta D = \frac{d_0 \Delta P}{\lambda} \tag{5.2}$$

where ΔP is the change of fringe spacing. It can be seen that the displacement ΔD is a linear function of ΔP for the constant wavelength λ and distance d_0. If D_0 is a given distance between the screen and the two fibres, equation 5.1 becomes

$$D_0 = \frac{d_0 P_0}{\lambda} \tag{5.3}$$

where P_0 is the fringe spacing corresponding to the distance D_0.

By combining equation 5.2 and equation 5.3, the displacement ΔD with the change of fringe spacing ΔP can be obtained, i.e.

$$\Delta D = \frac{D_0 \Delta P}{P_0} \tag{5.4}$$

Equation 5.4 is valid under the conditions that the distance between the two fibres d_0, wavelength λ and the magnification factor of lens [19] are constants, and that the distance D_0 is considerately greater than the distance d_0.

In this method, the fringe spacing and its changes are determined using fringe pattern matching together with linear interpolation to achieve subpixel accuracy [20, 21, 22, 23]. Assuming that the fringes are vertical in fringe patterns, the intensity distribution of the nth fringe pattern $I_n(i,j)$ used in the matching can be described by [24, 25, 26, 27]

$$I_n(i,j) = a_n(i,j) + b_n(i,j)\cos(\frac{2\pi i}{P} + \phi_n), \quad n = 0,1,2,...;\ i,j = 0,1,2,... \tag{5.5}$$

where $a_n(i,j)$ is the background illumination, $b_n(i,j)$ is the modulation of the fringes, and ϕ_n is the reference phase. It should be noted that the fringe spacing is not a constant in equation 5.5.

The mismatch function $f_n(t)$ in this case can be expressed as

$$f_n(t) = k_0 \sum_{(i,j)\in R} [I_n(i,j) - I_n(i+t,j)]^2, \quad n = 0, 1, 2, ... \tag{5.6}$$

where R is the region of the reference image patch, t is the shifted pixel number, and k_0 is the inverse of the element number in the calculation.

Figure 5.2, as an example, shows two computer generated 8-bit grey-level fringe patterns with a displacement of 10 mm between them. The fringe spacing of the reference fringe pattern for $D_0 = 1000$ mm is 100 pixels, as shown in figure 5.2(a). The given displacement is 10 mm and the measured is 9.9213 mm. The phase curves obtained from the two computer generated 8-bit grey-level, 512×512 pixel fringe patterns are shown in figure 5.3. It can be seen that the mismatch function expressed by equation 5.6 is equal to zero at the origin of co-ordinates, which is definitely the matching point for the fringe pattern, and it changes periodically.

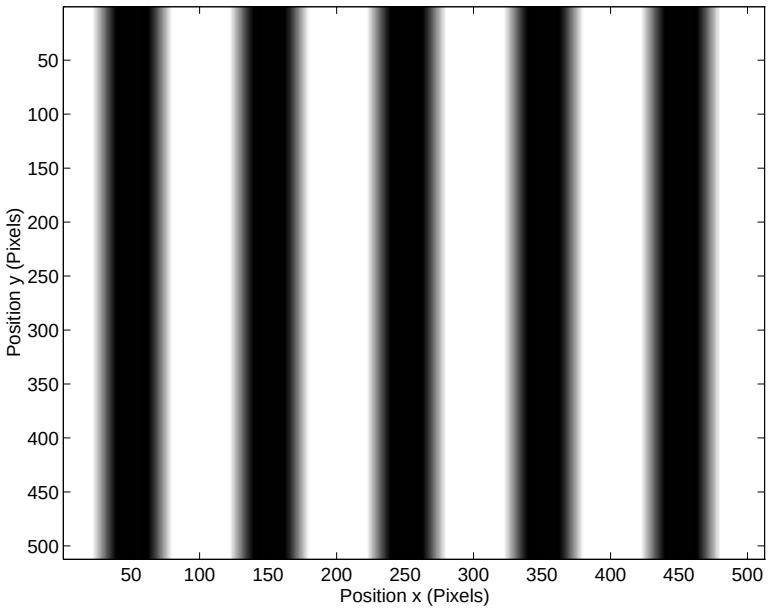

(a) Reference fringe pattern

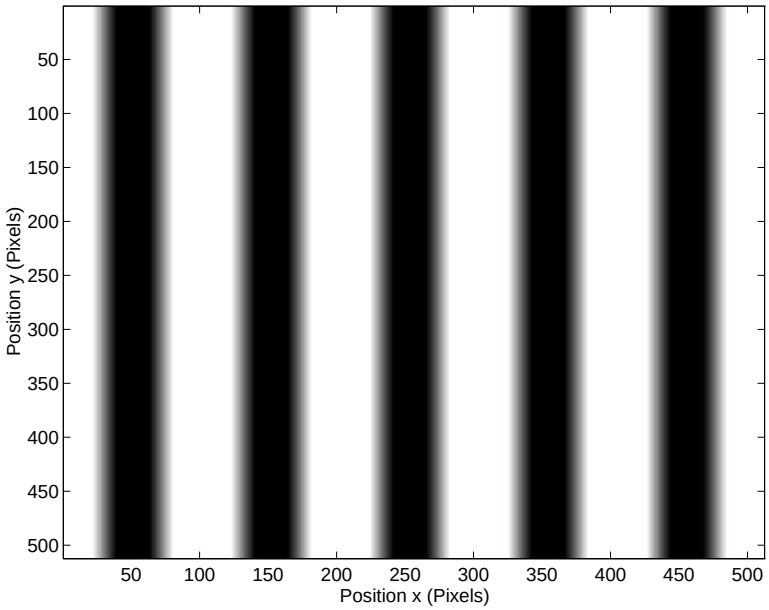

(b) Fringe pattern after a displacement of 10 mm

Figure 5.2: Two computer generated 8-bit grey-level fringe patterns with a displacement of 10 mm between them

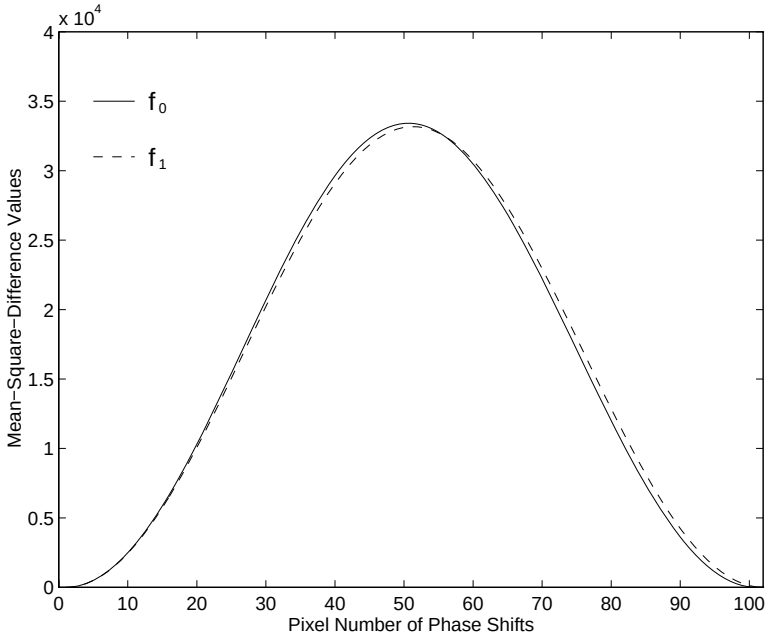

Figure 5.3: Phase curves from the two computer generated 8-bit grey-level fringe patterns

5.3 Experimentation

The method of displacement measurement based on Young's experiment was examined in a fibre-optic interferometer system as shown in figure 5.4. In the experiment, the optic fibres in figure 5.4 were displaced by a translation stage with a resolution of 0.01 mm to change the distance D and the fringe spacing P. The initial value of distance D was set to 1000 mm, i.e. D_0=1000 mm in equation 5.4. The distance between the diffuser and the CCD camera was kept constant during the experiment to suppress the effect of the focus of the camera on the experimental result when the distance D was changed. The distance between the fibres, d_0, was held constant at about 0.4 mm in the experiment.

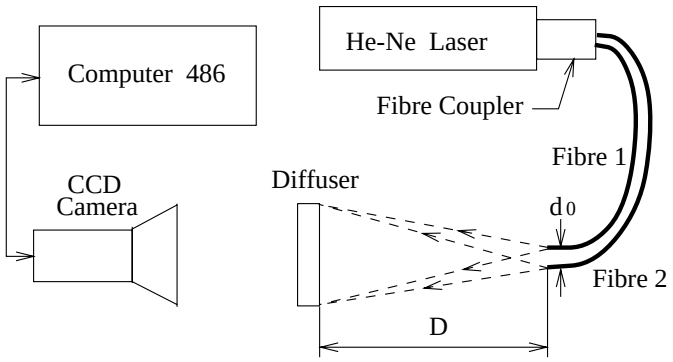

Figure 5.4: Schematic of displacement measurement system

Figure 5.5 shows two captured interferograms with a displacement of 10 mm between them. They are 8-bit grey-level, 512× 512 pixel images. The phase curves of the two interferograms calculated from equation 5.6 are shown in figure 5.6. Figure 5.7 shows the measured fringe spacing versus the given displacement over a range of 10 mm, and figure 5.8 shows the measured displacement versus the given displacement. The standard deviation versus the given displacement over a range of 10 mm is shown in figure 5.9.

In the experiment, the 301×312 pixel image patches were used for the calculations of mean-square-difference to obtain the phase curves. The standard deviation

obtained from one hundred and thirty captured interferograms was better than 0.12 mm over a range of 10 mm.

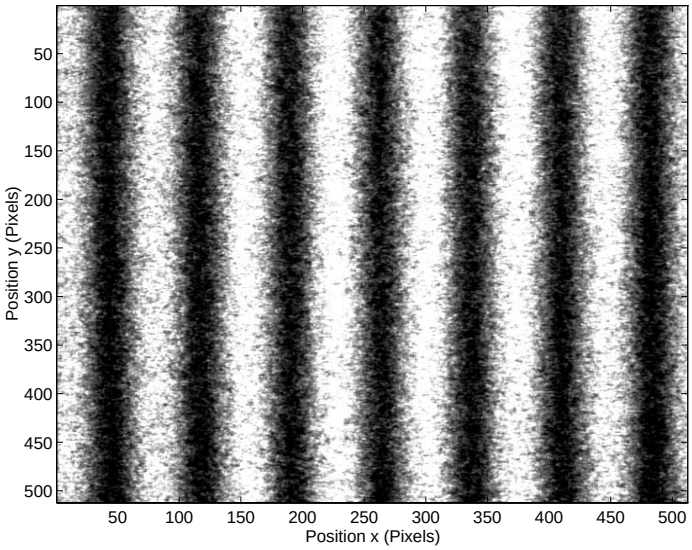

(a) Reference interferogram

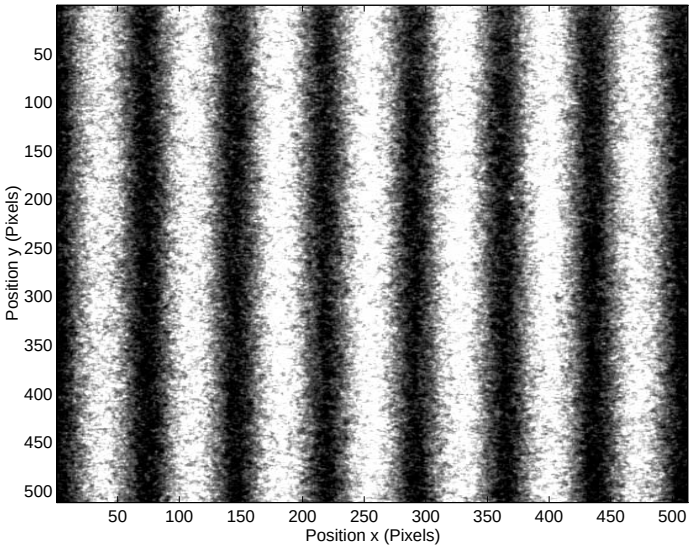

(b) Interferogram after a displacement of 10 mm

Figure 5.5: Two captured interferograms with a displacement of 10 mm between them

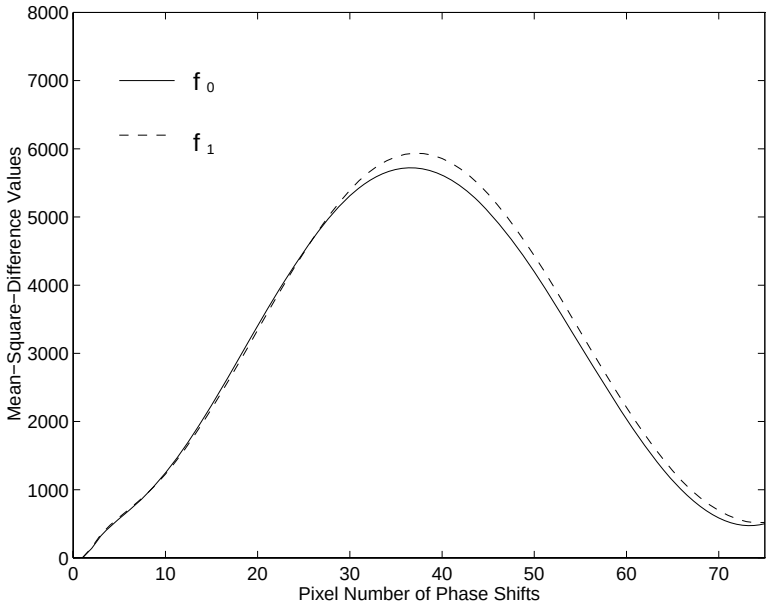

Figure 5.6: Phase curves from the two captured interferograms

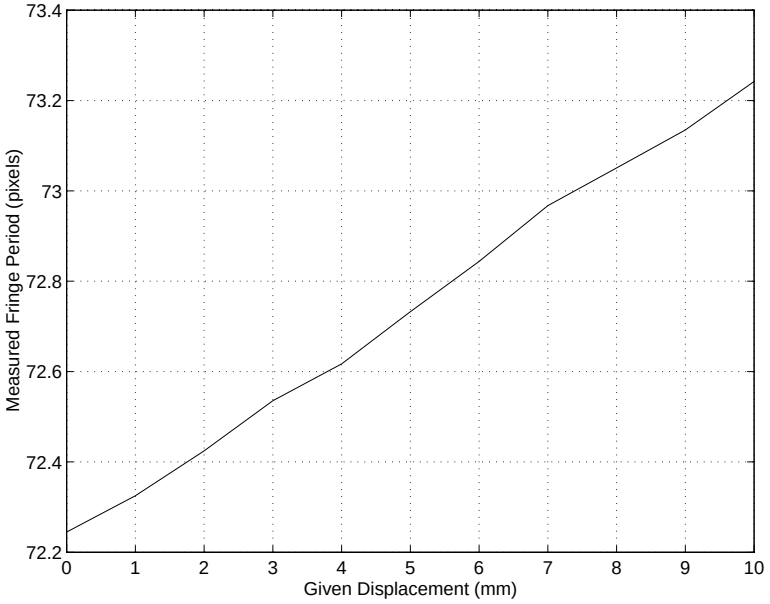

Figure 5.7: Measured fringe spacing versus given displacement over a range of 10 mm

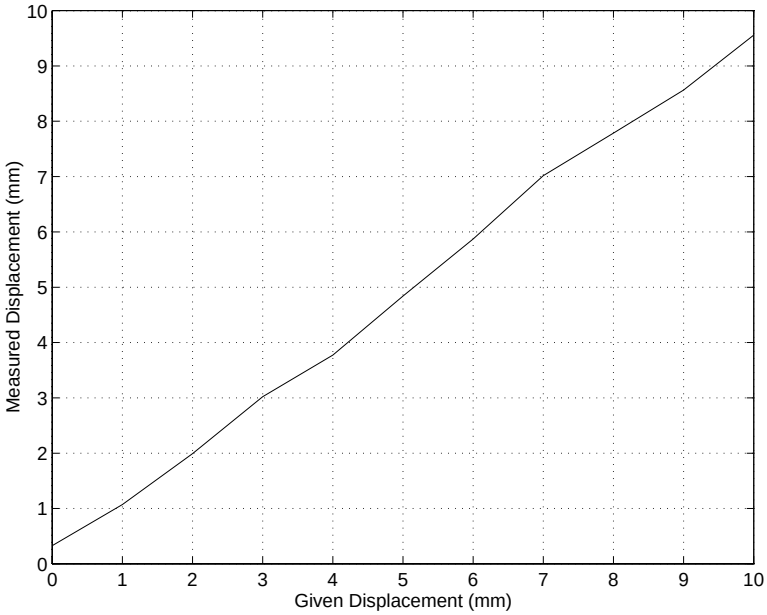

Figure 5.8: Measured displacement versus given displacement over a range of 10 mm

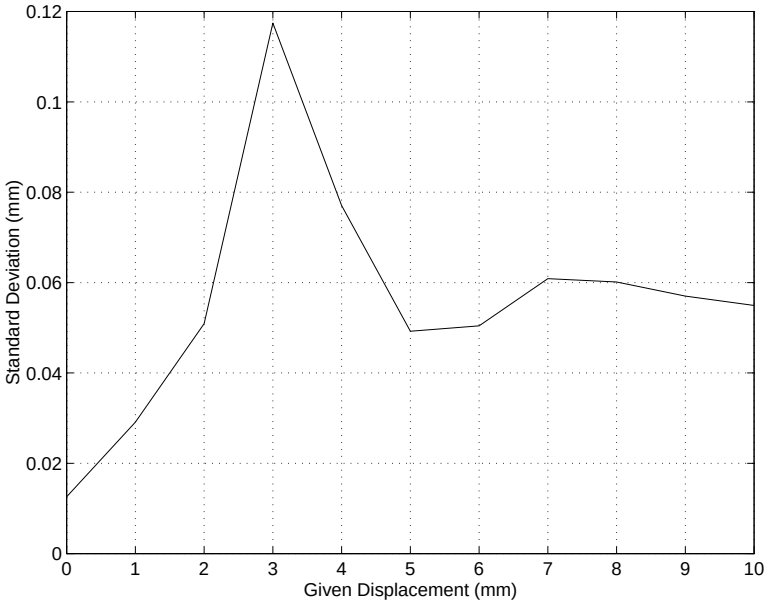

Figure 5.9: Standard deviation versus given displacement over a range of 10 mm

5.4 Effect of Imager resolutions

The effect of grey level resolution and spatial resolution on the measurement of displacement based on Young's experiment is illustrated in this section. The computer simulation results were obtained from different grey levels and fringe spacings of fringe patterns.

In the simulation, the intensity distribution of the computer generated fringe pattern was

$$I_n(i,j) = \text{round}[\frac{2^K - 1}{2}(1 + \cos\frac{2\pi i}{P})], \quad n = 0,1,2,...;\ i,j = 0,1,2,...,511 \quad (5.7)$$

where the function round(x) rounds x to the nearest integer to acquire the quantised fringe pattern. K stands for the bit number of discrete grey levels, and P is the fringe spacing.

There were two assumptions in the simulation. One was that the diffuser surface illumination and the light sensitivity of the CCD array were uniform. The other was that the fringe patterns were captured under the condition that the laser beams from the fibres were normal to the surfaces of the diffuser and CCD array.

5.4.1 Effect of Grey Level Resolution

In the simulation of the effect of grey level resolution on displacement measurement, the fringe spacing P in equation 5.7 was set to 100 pixels for a distance of 1000 mm, i.e. $P_0 = 100$ pixels when $D_0 = 1000$ mm.

Figure 5.10 shows the displacement error curve from two hundred 8-bit grey-level fringe patterns generated by computer over a range of 10 mm. The displacement error curves from 10-bit and 12-bit grey-level fringe patterns are shown in figures 5.11 and 5.12.

The maximum error of displacement measurement for 8-bit grey levels in the simulation was 105 μm, that for 10-bit grey levels was 57 μm, and that for 12-bit grey levels was 46 μm. It can be seen that the higher grey-level resolution has achieved a better accuracy in the measurement of displacement.

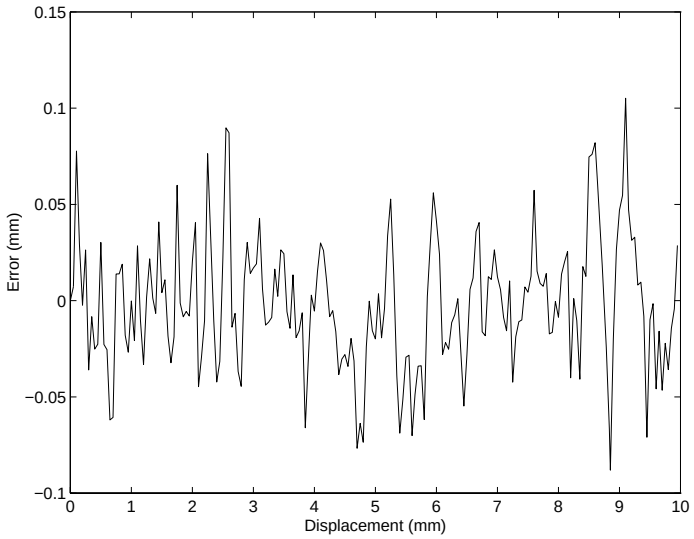

Figure 5.10: Displacement error curve from 8-bit grey-level fringe patterns

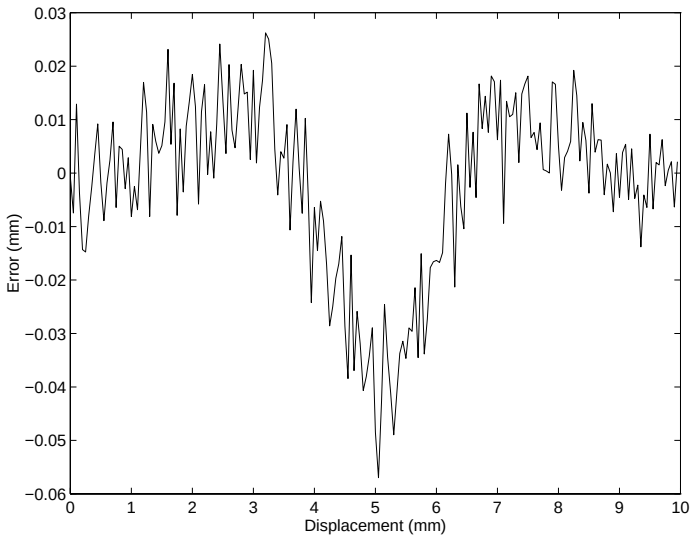

Figure 5.11: Displacement error curve from 10-bit grey-level fringe patterns

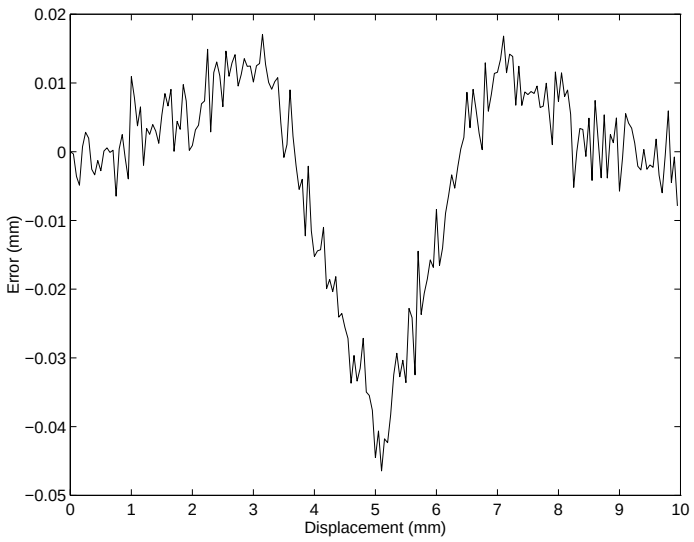

Figure 5.12: Displacement error curve from 12-bit grey-level fringe patterns

5.4.2 Effect of Spatial Resolution

In the simulation of the effect of spatial resolution on displacement measurement, the bit number of discrete grey levels was set to eight in equation 5.7. The initial fringe spacings for D_0=1000 mm were 60, 80 and 100 pixels, respectively.

Figure 5.13 shows the displacement error curve obtained from two hundred 8-bit grey-level fringe patterns with the initial fringe spacing of 60 pixels over a range of 10 mm. The displacement error curves from the fringe patterns with the initial fringe spacings of 80 and 100 pixels are shown in figure 5.14 and 5.15.

The maximum error of displacement measurement from the fringe patterns with the initial fringe spacing of 60 pixels was 151 μm, that from the fringe patterns with the initial fringe spacing of 80 pixels was 113 μm, and that from the fringe patterns with the initial fringe spacing of 100 pixels was 105 μm. It can be seen that the higher spatial resolution or sampling frequency has obtained a better accuracy in the measurement of displacement.

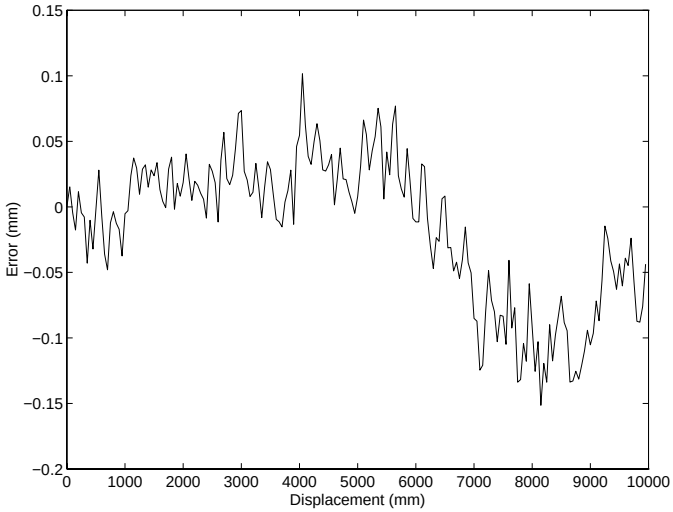

Figure 5.13: Displacement error curve from the fringe patterns with the initial fringe spacing of 60 pixels

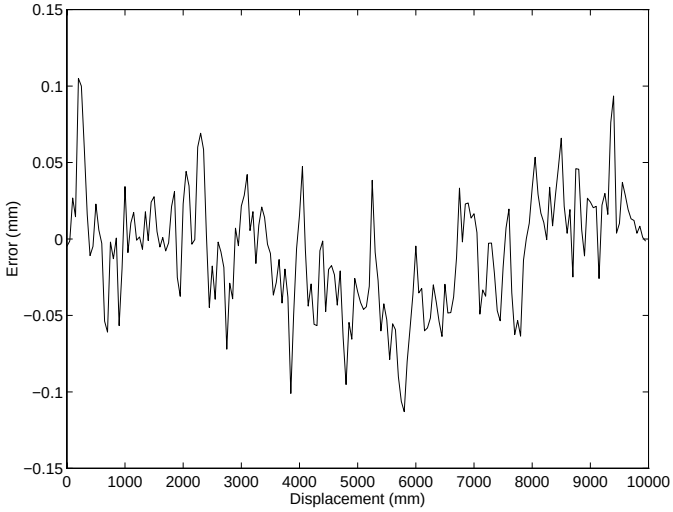

Figure 5.14: Displacement error curve from the fringe patterns with the initial fringe spacing of 80 pixels

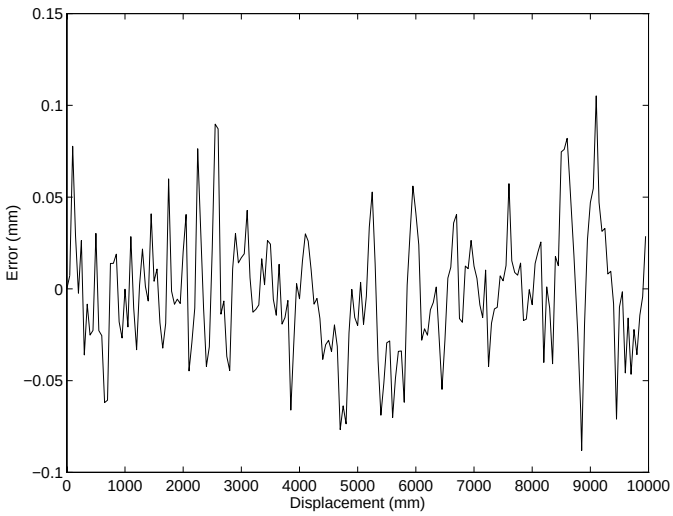

Figure 5.15: Displacement error curve from the fringe patterns with the initial fringe spacing of 100 pixels

5.5 Discussion

For the discussion of the effect of image patch size or noise on displacement measurement, equation 5.6 can be rewritten as

$$f_n(t) = k_0 \sum_{j=1}^{M} \sum_{i=1}^{N} w_n(t,i,j), \quad n = 0, 1, 2, ... \tag{5.8}$$

where

$$w_n(t,i,j) = [I_n(i,j) - I_n(i+t,j)]^2, \quad n = 0, 1, 2, ... \tag{5.9}$$

It is clear that equation 5.9 is the mismatch function obtained from the image patches of 1×1 pixel or one pixel, and equation 5.8 is the mismatch function obtained from the image patches of $M \times N$ pixels. The mismatch function expressed by equation 5.8 is in effect the superposition of $M \times N$ mismatch functions expressed by equation 5.9. Therefore, the method of fringe spacing determination by fringe pattern matching also has the advantage of averaging noise, and the effect of image patch size or noise on displacement measurement can be described by equation 3.21.

In theory, the fringe spacing can be acquired as accurate as expected in the calculations of mean-square-difference for the ideal fringe patterns. In practice, however, the accuracy is affected by many error sources such as the imager resolutions, unequally spaced fringes, non-uniform background illumination and noise. It can be seen, from the computer simulation results, that the accuracy of the displacement measurement based on Young's experiment is basically dependent on imager resolutions. The higher resolutions of the imaging sensor have a better accuracy in the measurement of displacement. In addition, the shape of the object will also limit the accuracy of the measurement if this method is used in a machine vision system.

In this chapter, it is assumed that the fringes are vertical in the fringe patterns. The method of displacement measurement by fringe pattern matching is in effect also valid for the fringe patterns in which the fringes are horizontal, oblique or curved, but the fringe spacing obtained from equation 5.6 is not the actual one in the case of oblique or curved fringes if the image patches are shifted in the horizontal or vertical directions. The error from the oblique or curved fringes can be corrected by careful calibration as it is a systematic error. For the fringe patterns with horizontal fringes, the image patches must be shifted along the axis of ordinates in this method.

5.6 Conclusion

The method of displacement measurement based on Young's experiment presented in this chapter provides a simple way to measure displacement. Fringe pattern matching is effective for the measurement of displacement. The computer simulation and experimental results have shown that it is possible to measure displacement or distance in a machine vision system in some cases using the method of displacement measurement based on Young's experiment.

Bibliography

[1] M.J. Downs and K.W. Raine, "An unmodulated bi-directional fringe-counting interferometer system for measuring displacement," *Precision Eng.* **1**, 85-88 (1979).

[2] N. Hagiwara, Y. Nishitani, M. Yanase, and T. Saegusa, "A phase encoding method for improving the resolution and reliability of laser interferometers," *IEEE Trans. Instrum. Meas.* **38**(2), 548-551 (1989).

[3] S. Hosoe, "Laser interferometric system for displacement measurement with high precision," *Nanotechnology* **2**, 88-95 (1991).

[4] D. Rugar, H.J. Mamin, R. Erlandsson, J.E. Stern, and B.D. Terris, "Force microscope using a fiber-optic displacement sensor," *Rev. Sci. Instrum.* **59**(11), 2337-2340 (1988).

[5] A. Oulamara, G. Tribillon, and J. Duvernoy, "Subpixel speckle displacement measurement using a digital processing technique," *J. Modern Opt.* **35**(7), 1201-1211 (1988).

[6] C. Schonenberger and S.F. Alarado, "A differential interferometer for force microscopy," *Rev. Sci. Instrum.* **60**(10), 3131-3134 (1989).

[7] D. Rugar, H.J. Mamin, and P. Guethner, "Improve fiber-optic interferometer for atomic force microscopy," *Appl. Phys. Lett.* **55**(25), 2588-2590 (1989).

[8] Y. Martin, C.C. Williams, and H.K. Wickramasinghe, "Atomic force microscope-force mapping and profiling on a sub 100-$\mathring{A}$ scale," *J. Appl. Phys.* **61**(10), 4723-4729 (1987).

[9] P.G. Charette, I.W. Hunter, and C.J.H. Brenan, "A complete high performance heterodyne interferometer displacement transducer for microactuator control," *Rev. Sci. Instrum.* **63**(1), 241-248 (1992).

[10] M. Sasaki, K. Hane, S. Okuma, M. Hino, and Y. Bessho, "Improved differential heterodyne interferometer for atomic force microscopy," *Rev. Sci. Instrum.* **65**(12), 3697-3701 (1994).

[11] N. Bobroff, "Recent advances in displacement measuring interferometry," *Meas. Sci. Technol.* **4**(9), 907-925 (1993).

[12] J. Schneir, T.H. McWaid, J. Alexander, and B.P. Wilfley, "Design of an atomic force microscope with interferometric position control," *J. Vac. Sci. Technol. B* **12**(6), 3561-3566 (1994).

[13] Z. Ji and M.C. Leu, "Design of optical triangulation devices," *Opt. Laser Technol.* **21**(5), 335-338 (1989).

[14] H. Tan and Y. Geng, "Laser non-contacting displacement measurement," *Proc. SPIE* **1230**, 427-428 (1990).

[15] P.J. Gloeckner, K. Kokini, and W.H. Stevenson, "3D measurement of thermal deformations on an ultra-high density circuit moduled with a laser range probe," *IEEE Trans. Components, Hybrids, and Manufacturing Technology* **15**(4), 571-577 (1992).

[16] M.F. Costa and J.B. Almeida, "Microtopographic inspection of surfaces: a comparison between moire, contrived lightning and discreet triangulation methods," *Proc. SPIE* **2003**, 30-35 (1993).

[17] M. françon, *Optical Interferometry*, Academic Press, London (1966).

[18] D.R. Burton and M.J. Lalor, "Multichannel Fourier fringe analysis as an aid to automatic phase unwrapping," *Appl. Opt.* **33**(14), 2939-2948 (1994).

[19] D. Vernon, *Machine vision, automated visual inspection and robot vision*, Prentice Hall, London (1991).

[20] A. Goshtasby, G.C. Stockman, and C.V. Page "A region-based approach to digital image registration with subpixel accuracy," *IEEE Trans. Geoscience and Remote Sensing* **GE-24**(3), 390-399 (1986).

[21] A. Kashko, H. Buxton, B.F. Buxton, and D.A. Castelow, "Parallel matching and reconstruction algorithms in computer vision," *Parallel Computing* **8**(1-3), 3-17 (1988).

[22] G. He and K. Novak, "On line data capture by image matching on the mobile mapping system," *Proc. SPIE* **1820**, 50-56 (1992).

[23] A. Gruen and D. Stallmann, "High-accuracy matching of object edges," *Proc. SPIE* **1820**, 70-82 (1992).

[24] M. Chang, C.P. Hu, P. Lam, and J.C. Wyant, "High precision deformation measurement by digital phase shifting holographic interferometry," *Appl. Opt.* **24**(22), 3780-3783 (1985).

[25] K. Creath, "Phase-measurement interferometry techniques," *Prog. Opt.* **26**, 349-393 (1988).

[26] P.E. Perry, Jr. and J. McKelvie, "Calibration of a phase shifting moire interferometer," *Proc. SPIE* **2003**, 147-158 (1993).

[27] C. Joenathan, "Phase-measuring interferometry: new methods and error analysis," *Appl. Opt.* **33**(19), 4147-4155 (1994).

Chapter 6

Phase-Shifting Interferometry with Arbitrary Phase Steps

6.1 Introduction

Phase-shifting interferometry [1, 2, 3, 4] is now a powerful technique for the high precision measurement of many physical quantities. The basic concept of phase-shifting interferometry is that the phase in the interferogram can be determined by acquiring at least three frames of interferograms with different phase steps. The phase steps can be introduced by phase shifters such as PZT (piezo-electric transducer) and LCD (liquid crystal device) either in the object or in the reference beams. So far many algorithms for phase-shifting interferometry have been developed for precision phase measurement. The algorithms, which are often used, include three-step [5], four-step [6, 7], five-step [8], and multi-step [9, 10]. These algorithms are different from each other mainly in the frame number and the accuracy obtained in their applications. It is assumed that the phase steps are equal and precise as required in the phase calculations of the algorithms.

In practice, the phase steps are not only determined by the phase shifter but also by any change of the optical path difference. Therefore, the desired phase

steps cannot be achieved, and the error of phase measurement is introduced due to the phase step errors caused by air turbulence, vibration, thermal drift, mechanical drift, miscalibration and nonlinearity of the phase shifter. In recent years, many papers [11, 12, 13, 14, 15, 16, 17, 18, 19, 20, 21, 22, 23, 24] have dealt with this topic to diminish or eliminate the phase step errors. In the papers, the phase step error compensating [11, 12, 13, 14, 15, 16, 17, 18] or the phase step determining [19, 20, 21, 22, 23, 24] algorithms are proposed. In the phase step error compensating algorithms, only one or two of the phase step errors can be theoretically reduced or suppressed in particular cases, so that they are limited in their applications. In the phase step determining algorithms, the phase shifts are taken as unknowns and they are determined by the processes such as iteration [19], FFT (fast-Fourier-transform) [20], ellipse fitting [21, 22], and iterative least-squares fitting [23, 24]. These algorithms are inherently free from the phase step errors since they rely solely on the fringe pattern itself in the determination of the phase step.

In this chapter, an algorithm of phase-shifting interferometry with arbitrary phase steps is presented. In the algorithm, the phase steps are taken as unknowns, and fringe pattern matching is used for directly determining the phase step from interferograms. The algorithm was examined in an experiment of reconstructing a 3-D object. The phase step with subpixel resolution was achieved from the mean-square-difference calculations of any two image patches shifted pixel by pixel, and the method of linear interpolation was employed in computing the phase steps between the fringe patterns from the phase curves. The comparison between the results achieved from the computer generated interferograms with and without phase step errors was also made in the computer simulation of 3-D surface measurement.

In section 6.2 of this chapter, the algorithm of phase-shifting interferometry with arbitrary phase steps is described in detail. Section 6.3 illustrates the computer

simulation and experimental results. The discussion and conclusion of this chapter are given in sections 6.4 and 6.5, respectively.

6.2 Principle

In the case of a phase-shifting interferometry, the intensity distribution of the nth fringe pattern $I_n(i,j)$ can be described by

$$I_n(i,j) = a(i,j) + b(i,j)\cos[\phi(i,j) - \phi_n], \quad n = 0,1,2,...;\ i,j = 0,1,2,... \tag{6.1}$$

where a(i,j) is the background illumination, b(i,j) is the modulation of the fringes, $\phi(i,j)$ is the phase related to the physical quantity to be measured, and $\phi_n(\phi_0{=}0)$ is the phase step. This equation indicates that at least three fringe patterns with different phase steps need to be recorded to find the phase $\phi(i,j)$ in phase-shifting interferometry. For simplicity, a three-step algorithm is used in the following discussion. The principle can also be applied to the algorithms of four-step, five-step, and multi-step phase-shifting interferometry.

In a three-step phase-shifting interferometry, the light intensity distributions of the three recorded fringe patterns with the phase steps of 0, ϕ_1 and ϕ_2 can be written as

$$I_0(i,j) = a(i,j) + b(i,j)\cos\phi(i,j) \tag{6.2}$$

$$I_1(i,j) = a(i,j) + b(i,j)\cos[\phi(i,j) - \phi_1] \tag{6.3}$$

$$I_2(i,j) = a(i,j) + b(i,j)\cos[\phi(i,j) - \phi_2] \tag{6.4}$$

and the phase can be calculated by

$$\phi(i,j) = \arctan\frac{(I_2 - I_1) + (I_0 - I_2)\cos\phi_1 + (I_1 - I_0)\cos\phi_2}{(I_2 - I_0)\sin\phi_1 + (I_0 - I_1)\sin\phi_2} \tag{6.5}$$

In equation 6.5, the phase steps ϕ_1 and ϕ_2 are taken as unknowns and they are determined by fringe pattern matching. Assuming that the fringes are vertical in the fringe patterns, the mismatch function $f_n(t)$, in this case, can be expressed as

$$f_n(t) = k_0 \sum_{(i,j)\in R} [I_0(i,j) - I_n(i \pm t, j)]^2, \quad n = 0, 1, 2 \tag{6.6}$$

where R is the region of the reference image patch, t is the shifted pixel number, and k_0 is the inverse of the element number in the calculation. The sign before t defines the fringe shifting direction. For the fringes shifted in the left direction the mismatch function $f_n(t)$ is

$$f_n(t) = k_0 \sum_{(i,j)\in R} [I_0(i,j) - I_n(i - t, j)]^2, \quad n = 0, 1, 2 \tag{6.7}$$

and for the fringes shifted in the right direction the mismatch function $f_n(t)$ is

$$f_n(t) = k_0 \sum_{(i,j)\in R} [I_0(i,j) - I_n(i + t, j)]^2, \quad n = 0, 1, 2 \tag{6.8}$$

For the determination of phase steps in the three-step PSI, the phase steps ϕ_1 and ϕ_2, according to equations 2.13, 2.14, 2.15, 2.19, 2.20, 2.21, 2.22, 2.23 and 2.24, can be calculated using the following equations:

$$y_{i01} = \frac{y_{0max1}}{2} \tag{6.9}$$

$$y_{ik1} = \frac{y_{kmax1} + y_{kmin1}}{2}, \quad k = 1, 2 \tag{6.10}$$

$$y_{i02} = \frac{y_{0max2} + y_{0min2}}{2} \tag{6.11}$$

$$t_{i01} = \frac{y_{i01} - y_{01}}{y_{02} - y_{01}} + t_{01} \tag{6.12}$$

$$t_{ik1} = \frac{y_{ik1} - y_{k1}}{y_{k2} - y_{k1}} + t_{k1}, \quad k = 1, 2 \tag{6.13}$$

$$t_{i02} = \frac{y_{i02} - y_{03}}{y_{04} - y_{03}} + t_{03} \tag{6.14}$$

$$P = t_{i02} - t_{i01} \tag{6.15}$$

$$\phi_k = \frac{t_{kmin1}}{P} \times 360^o, \quad k = 1, 2 \tag{6.16}$$

where the phase step in pixels is

$$t_{kmin1} = t_{ik1} - t_{i01}, \quad k = 1, 2 \tag{6.17}$$

In the above, it is assumed that the fringes are vertical in the fringe patterns. The algorithm of phase step determination by fringe pattern matching is also valid for the fringe patterns in which the fringes are horizontal, oblique or curved. For the fringe patterns with horizontal fringes, the image patches must be shifted along the axis of ordinates in the matching.

6.3 Experimentation

In the algorithm of phase-shifting interferometry with arbitrary phase steps, the phase steps are taken as unknowns in capturing fringe patterns and they are determined afterwards. The phase-shifted fringe patterns are processed by fringe pattern matching to find the phase steps. In this section, the algorithm of phase-shifting interferometry with arbitrary phase steps is illustrated through both computer simulation and experiment. Figure 6.1 shows the flow chart of programming for the three-step PSI with arbitrary phase shifts.

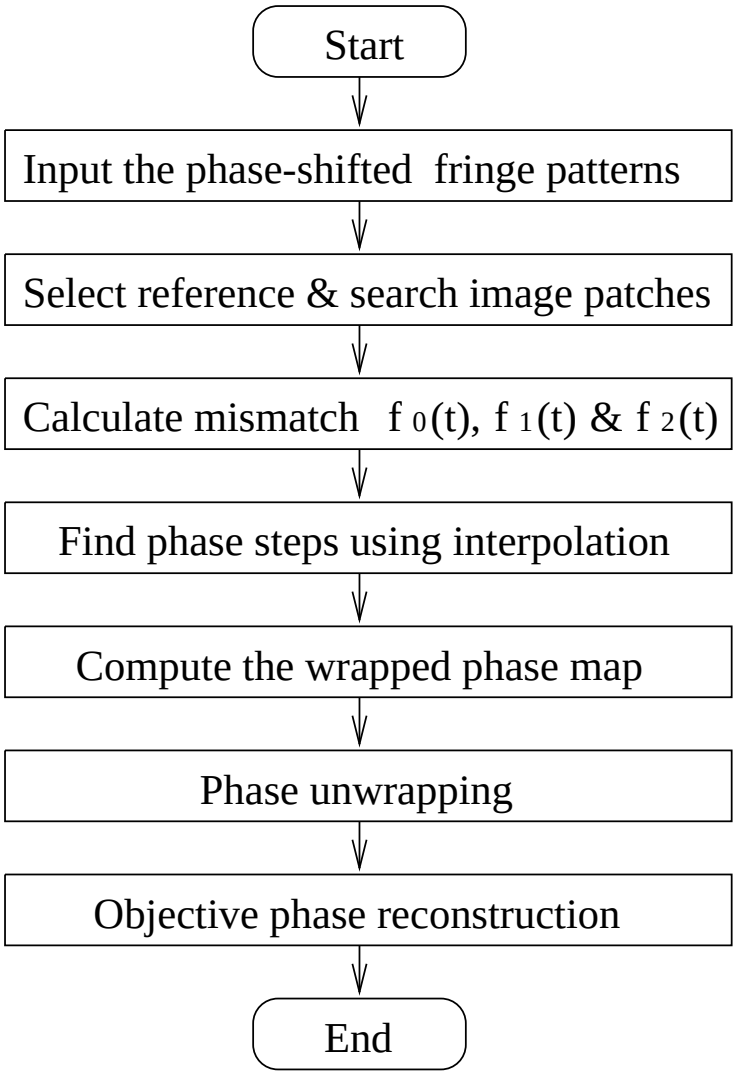

Figure 6.1: Flow chart of programming for the three-step PSI with arbitrary phase shifts

6.3.1 Computer Simulation

The algorithm of phase-shifting interferometry with arbitrary phase steps was examined in the computer simulation for measuring a 3-D surface. In the simulation, the computer generated 3-D surface was

$$Z(i,j) = \begin{cases} Z_0(i,j) & \text{if } Z_r(i,j) \geq 0 \\ 0 & \text{otherwise} \end{cases} \tag{6.18}$$

where

$$Z_r(i,j) = k_r^2[r^2 - (i-128)^2 - (j-128)^2] \tag{6.19}$$

and

$$Z_0(i,j) = \sqrt{Z_r(i,j)} \tag{6.20}$$

In equation 6.19, k_r is a constant and r is the radius of the object. A computer generated 3-D surface is shown in figure 6.2 in which r=64 pixels, $k_r = \frac{1}{16}$, and the image size is 256×256 pixels.

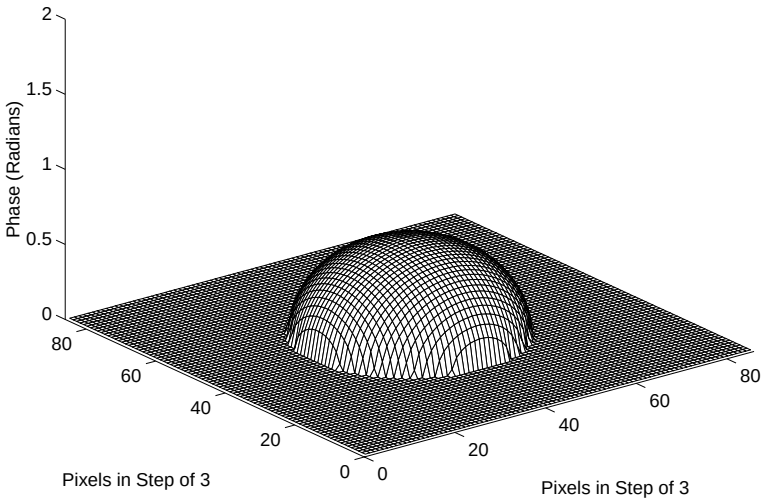

Figure 6.2: Computer generated 3-D surface

Figure 6.3 shows the schematic of computer simulation for 3-D surface measurement. In the figure, it is assumed that the surface illumination and reflectance are uniform, and that the viewing direction of the CCD camera is normal to the surface of the measured object.

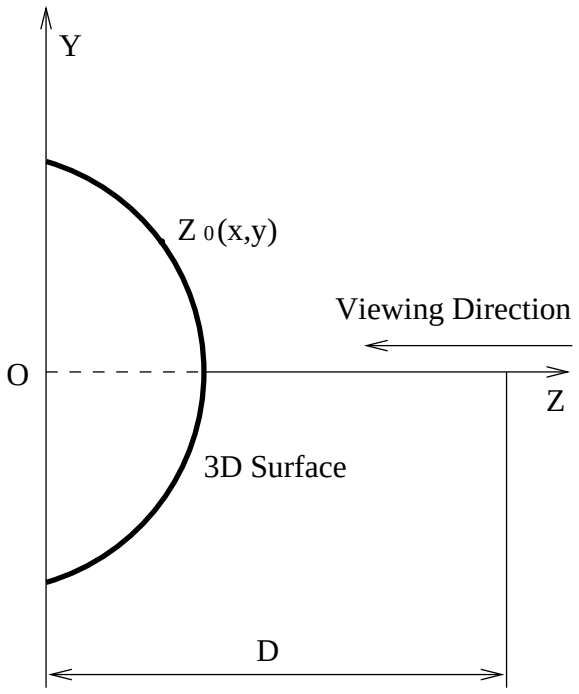

Figure 6.3: Schematic of computer simulation for 3-D surface measurement

From the discussion of Young's experiment and equation 1.22 in chapter 1, the deformed fringe patterns on the object surface can be described by the effective fringe period. The effective fringe period T(i,j) can be determined using

$$\mathrm{T(i,j)} = \frac{\lambda\,[\mathrm{D} - \mathrm{Z(i,j)}]}{\mathrm{d_0}} \tag{6.21}$$

where λ is the wavelength, D is the distance between the light source and the fringe projection screen, and $\mathrm{d_0}$ is the distance between the two slits. As such the three computer generated fringe patterns with the phase steps of 0^o, 89.5^o and

179^o can be expressed as

$$I_0(i,j) = \text{round}\{127.5 + 127.5\cos[\frac{2\pi i}{T(i,j)}]\} \tag{6.22}$$

$$I_1(i,j) = \text{round}\{127.5 + 127.5\cos[\frac{2\pi i}{T(i,j)} - \frac{89.5 \times 2\pi}{360}]\} \tag{6.23}$$

$$I_2(i,j) = \text{round}\{127.5 + 127.5\cos[\frac{2\pi i}{T(i,j)} - \frac{189 \times 2\pi}{360}]\} \tag{6.24}$$

where i=0, 1, 2, ..., 255 and j=0, 1, 2, ..., 255. The function round(x) rounds x to the nearest integer to obtain the 8-bit grey-level fringe patterns.

In the above, the phase $\phi(i,j)$ can be calculated by equation 6.5, and it can also be expressed as

$$\phi(i,j) = \frac{2\pi i}{T(i,j)} \tag{6.25}$$

Substituting equation 6.21 into equation 6.25 can obtain the relationship between the phase and the object dimension, i.e.

$$\phi(i,j) = \frac{2\pi d_0 i}{\lambda[D - Z(i,j)]} \tag{6.26}$$

or

$$Z(i,j) = \frac{\lambda D\phi(i,j) - 2\pi d_0 i}{\lambda\phi(i,j)} \tag{6.27}$$

In the above, D=1000 mm and $\frac{\lambda}{d_0} = 0.04$. The three computer generated 8-bit grey-level fringe patterns with the phase steps of 0^o, 89.5^o and 179^o are shown in figure 6.4. The fringes in the interferograms expressed by equations 6.22, 6.23 and 6.24 are shifted in the right direction, so that equation 6.8 is used to compute the mean-square-difference values. The phase curves of the three fringe patterns with the phase steps of 89.5^o and 179^o are shown in figure 6.5.

In the simulation, the phase steps of the fringe patterns, which were calculated by linear interpolation from the phase curves, were 89.4865^o and 178.9775^o, respec-

tively. The phase $\phi(i, j)$ was then calculated by equation 6.5 in which ϕ_1=89.4865^o and ϕ_2=178.9775^o. Figure 6.6 shows the wrapped phase map of the 3-D surface calculated from the fringe patterns with the phase steps of 0°, 89.4865° and 178.9775°, and figure 6.7 shows the 3-D plot of the unwrapped phase. The 3-D plot of the surface after reconstruction is shown in figure 6.8. Two of the MATLAB programmes for phase-shifting interferometry with arbitrary phase steps are given in appendix D.

The phase $\phi(i, j)$ was also calculated by equation 6.5 in which ϕ_1=89.5° and ϕ_2=179° in the simulation. Figure 6.9 shows the wrapped phase map of the 3-D surface from the fringe patterns with the phase steps of 0°, 89.5° and 189°, and figure 6.10 shows the 3-D plot of the unwrapped phase. The 3-D plot of the surface after reconstruction is shown in figure 6.11. Figure 6.12 shows the error distribution of the reconstructed surface from the fringe patterns with the given phase steps and the phase steps found by fringe pattern matching.

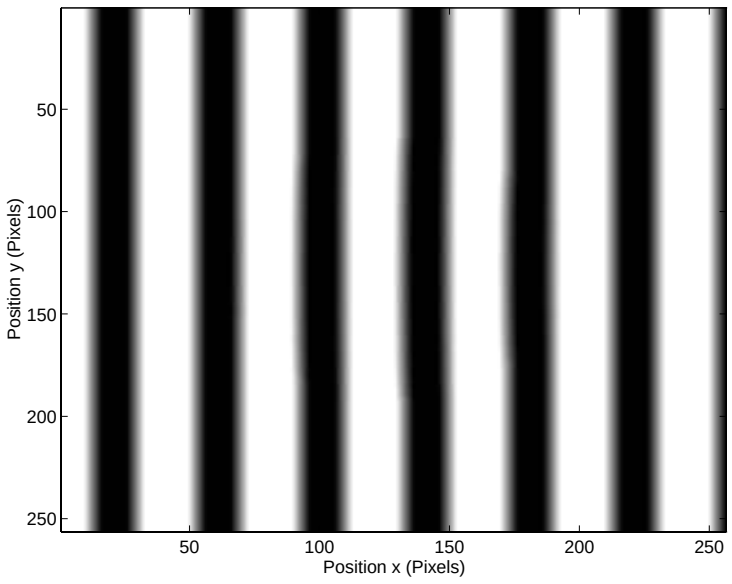

(a) Phase step ϕ_0=0^o

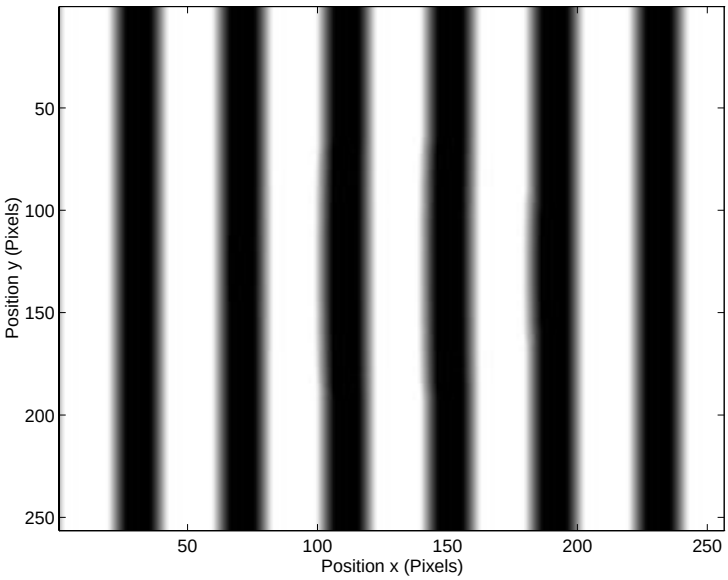

(b) Phase step ϕ_1=89.5^o

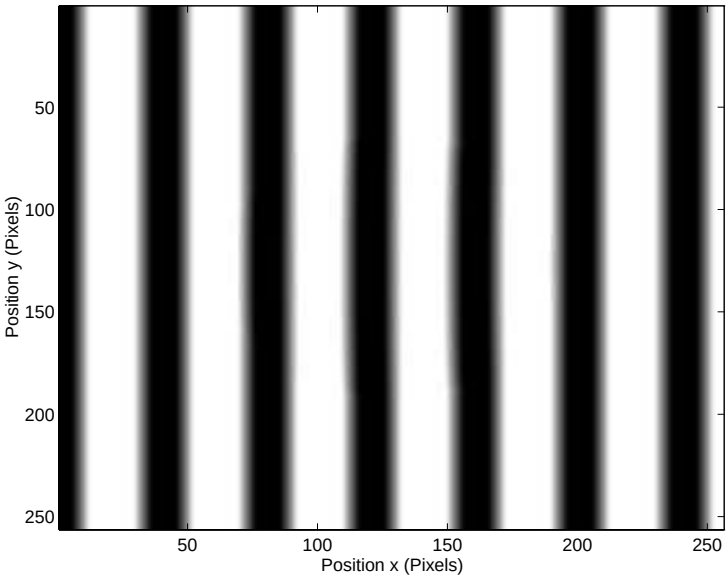

(c) Phase step ϕ_2=179^o

Figure 6.4: Three computer generated fringe patterns with the phase steps of 0^o, 89.5^o and 179^o

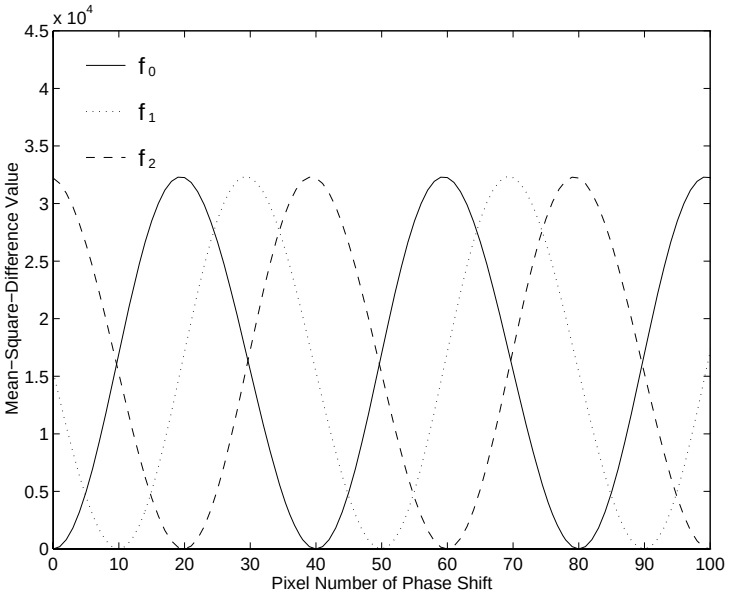

Figure 6.5: Phase curves from the three fringe patterns

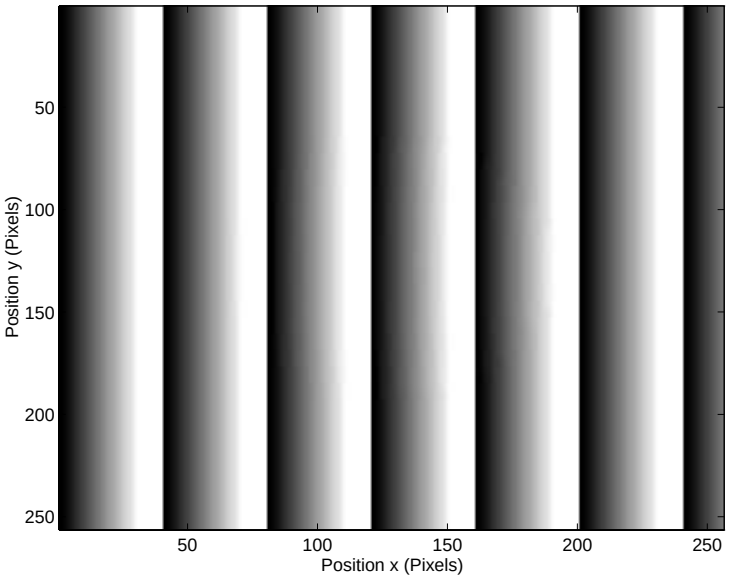

Figure 6.6: Wrapped phase map from the fringe patterns with the phase steps of 0°, 89.4865° and 178.9775°

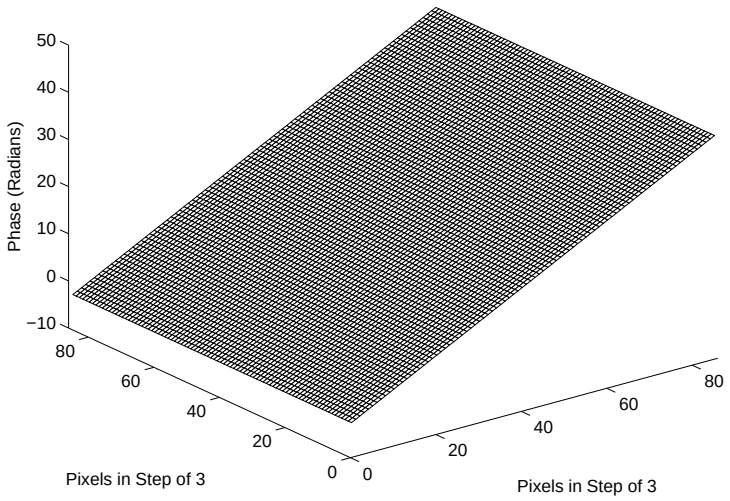

Figure 6.7: 3-D plot of the unwrapped phase from the fringe patterns with the phase steps of 0°, 89.4865° and 178.9775°

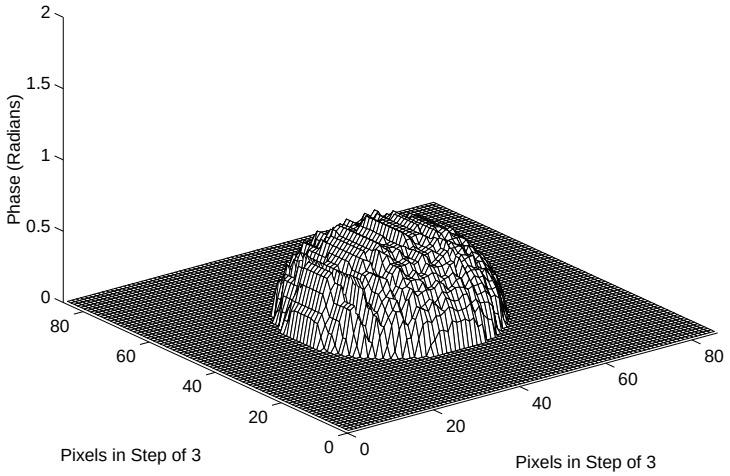

Figure 6.8: 3-D plot of the surface after reconstruction from the fringe patterns with the phase steps of 0°, 89.4865° and 178.9775°

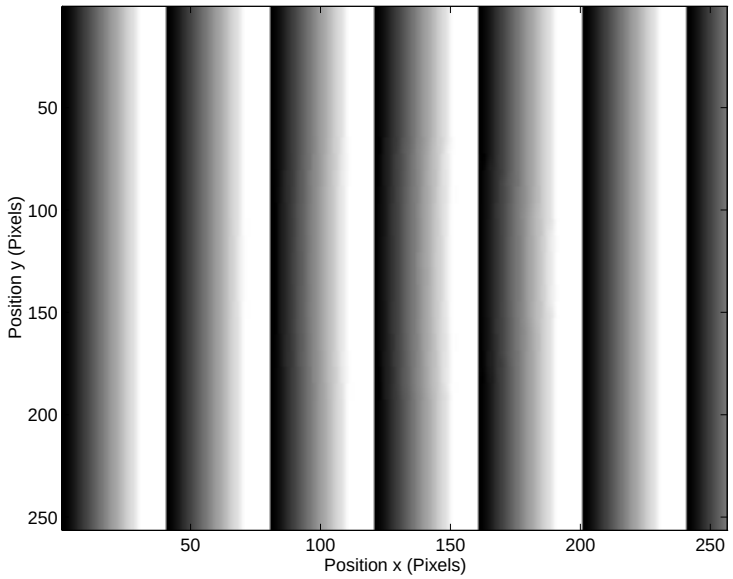

Figure 6.9: Wrapped phase map from the fringe patterns with the phase steps of 0°, 89.5° and 189°

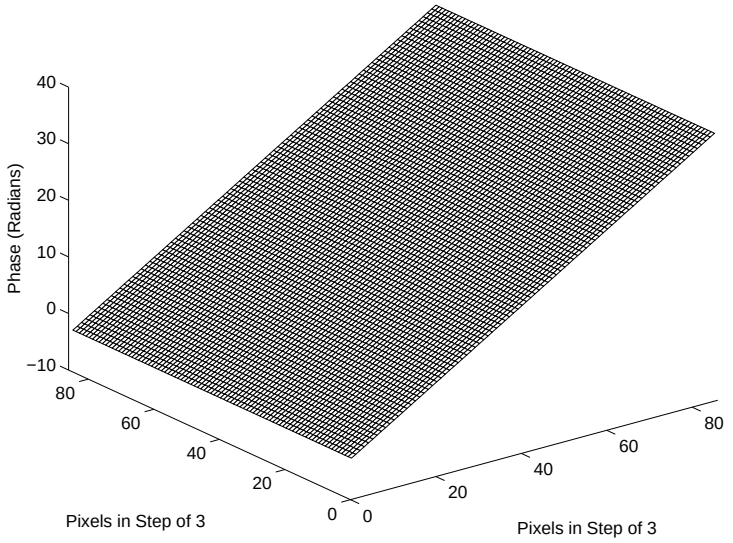

Figure 6.10: 3-D plot of the unwrapped phase from the fringe patterns with the phase steps of 0°, 89.5° and 189°

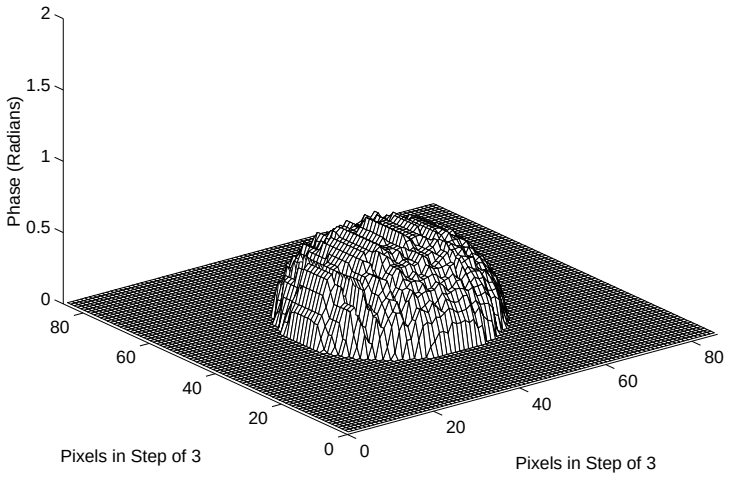

Figure 6.11: 3-D plot of the surface after reconstruction from the fringe patterns with the phase steps of 0°, 89.5° and 189°

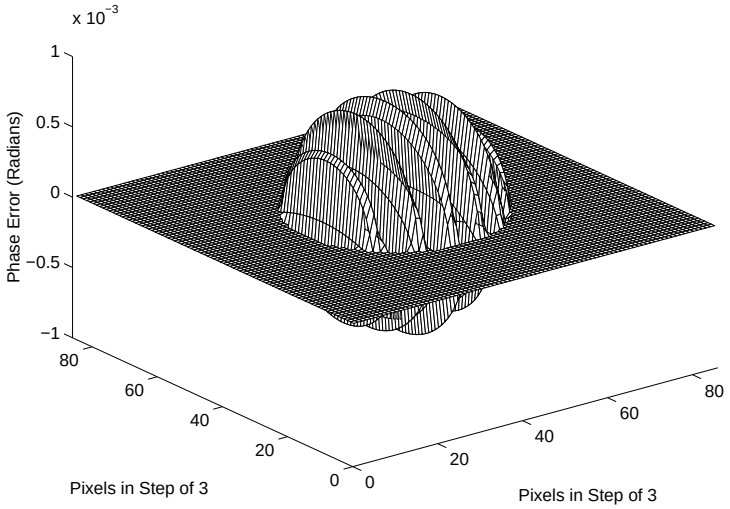

Figure 6.12: Error distribution of the reconstructed 3-D surface from the fringe patterns with the given phase steps and the phase steps found by fringe pattern matching

6.3.2 Experimental Results

The use of the algorithm of phase-shifting interferometry with arbitrary phase steps is illustrated using the system for reconstructing 3-D object shapes as shown in figure 6.13. In the experiment, the Michelson's interferometer, consisting of a He-Ne laser, pinhole, lenses 1 and 2, mirrors 1 and 2 and a beam splitter, was used to generate the projected fringe pattern onto the object in this system. The phase shifts of the transmitted light were carried out by the electronic phase shifter with an LCD (liquid crystal device) and a voltage control circuit of outputting a 100Hz square wave [25]. The nose of a statue was used as a test object in the experiment.

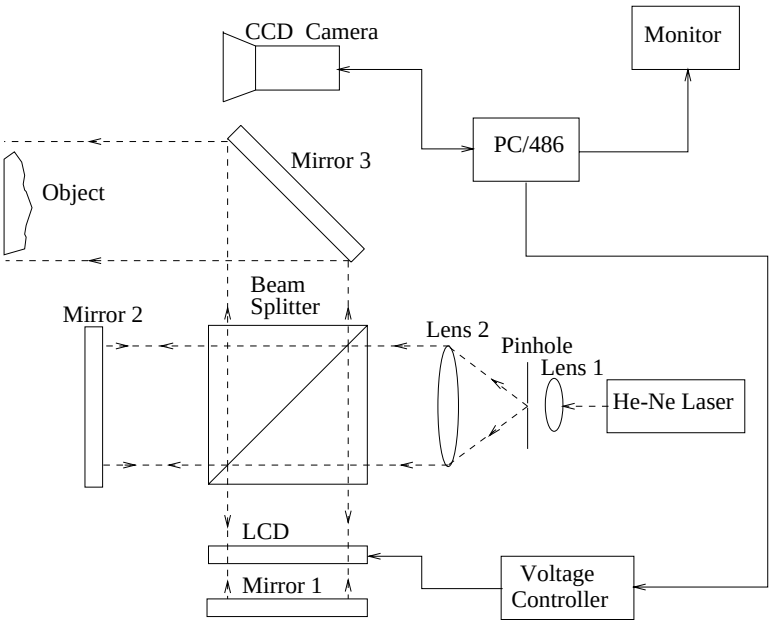

Figure 6.13: System for reconstructing 3-D object shapes

Figure 6.14 shows three 8-bit grey-level interferograms with the size of 512×512 pixels, captured in the experiment. The phase curves of the three interferograms obtained from the mean-square-difference calculations are shown in figure 6.15. The phase steps of the fringe patterns, which were calculated by fringe pattern matching together with linear interpolation, are 117.0° and 196.4°. Figure 6.16

shows the wrapped phase map of the nose, and figure 6.17 shows the 3-D plot of the unwrapped phase. The 3-D plot of the nose after reconstruction is shown in figure 6.18.

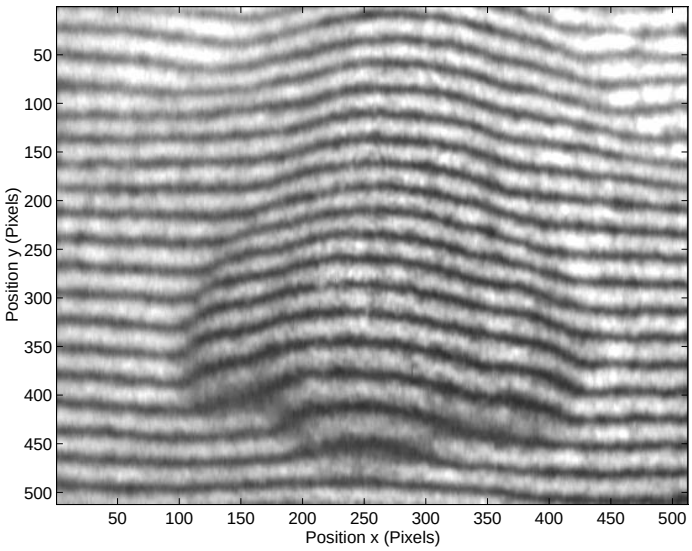

(a) Phase step $\phi_0 = 0^o$

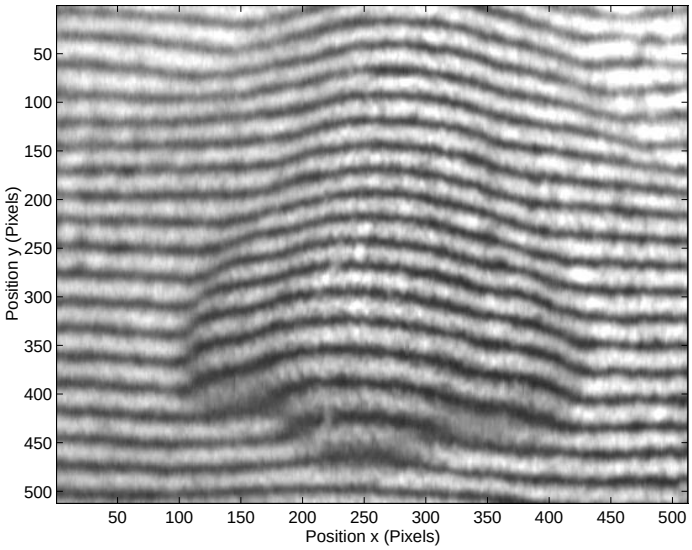

(b) Phase step $\phi_1 = 117.0^o$

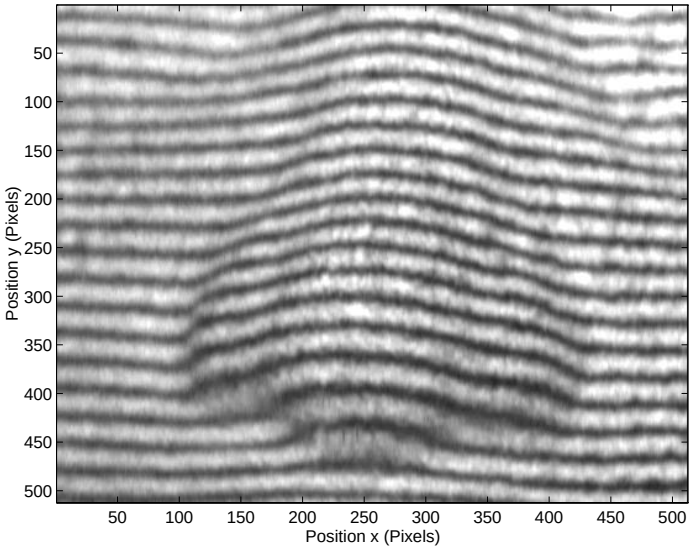

(c) Phase step $\phi_2 = 196.4^o$

Figure 6.14: Three captured interferograms with the phase steps of 0^o, 117.0^o and 196.4^o

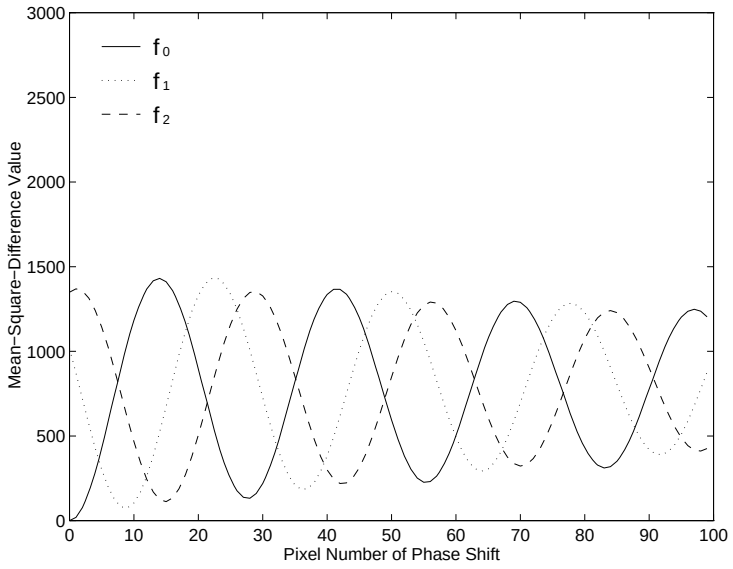

Figure 6.15: Phase curves obtained from the three captured interferograms

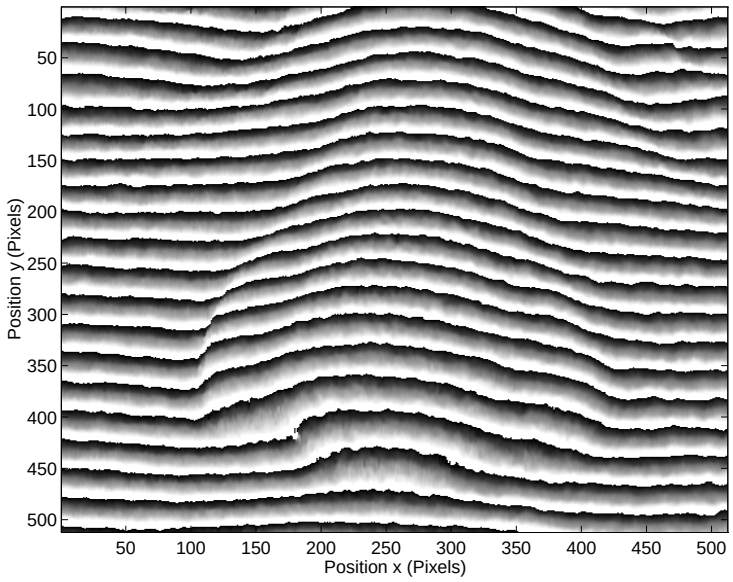

Figure 6.16: Wrapped phase map from the three captured interferograms

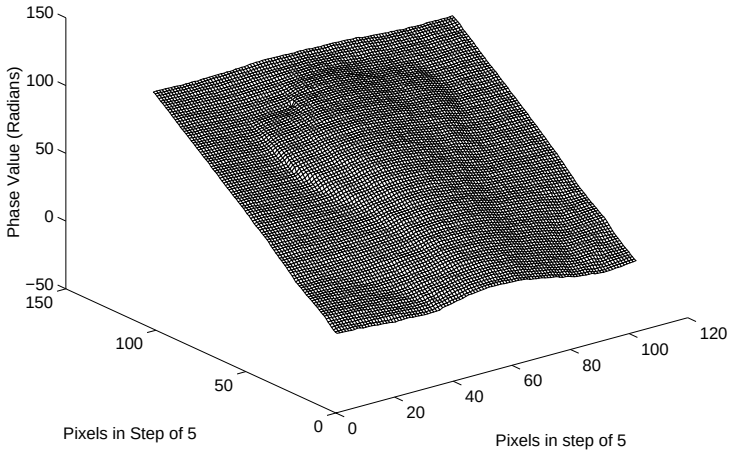

Figure 6.17: 3-D plot of the unwrapped phase from the three captured interferograms

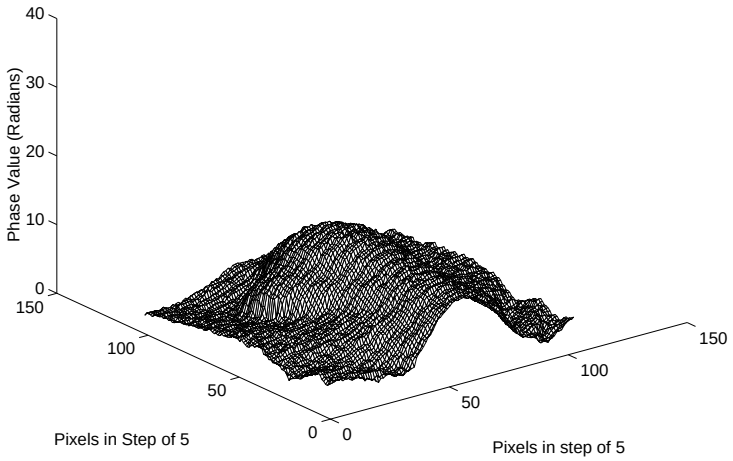

Figure 6.18: 3-D plot of the nose after reconstruction

6.4 Discussion

In phase-shifting interferometry, it is often difficult, or impossible to introduce the phase steps as accurately as expected due to the air turbulence, vibration, thermal drift, mechanical drift, miscalibration and nonlinearity of the phase shifter. Let $\phi'(\mathrm{x},\mathrm{y})$ be the phase calculated from the fringe patterns with the expected phase shifts of 0°, 90° and 180°. If the introduced phase steps are expected to be 0°, 90° and 180°, the phase error $\Delta\phi(\mathrm{x},\mathrm{y})$ caused by the inaccurate phase steps can be calculated using

$$\Delta\phi(\mathrm{x},\mathrm{y}) = \phi(\mathrm{x},\mathrm{y}) - \phi'(\mathrm{x},\mathrm{y}) \tag{6.28}$$

where

$$\phi'(\mathrm{x},\mathrm{y}) = \arctan\frac{(\mathrm{I}_2 - \mathrm{I}_1) + (\mathrm{I}_0 - \mathrm{I}_1)}{(\mathrm{I}_2 - \mathrm{I}_0)} \tag{6.29}$$

Figure 6.19 shows the wrapped phase map of the three computer generated fringe patterns computed from equation 6.29. The 3-D plot of the unwrapped phase is

shown in figure 6.20. Figure 6.21 shows the 3-D plot of the surface reconstructed from the computer generated fringe patterns with phase step errors, and the error distribution is shown in figure 6.22.

Figure 6.23 shows the wrapped phase map of the three captured interferograms calculated from equation 6.29. The 3-D plot of the unwrapped phase is shown in figure 6.24. Figure 6.25 shows the 3-D plot of the nose reconstructed from the captured interferograms with phase step errors, and the error distribution is shown in figure 6.26.

It is clear that the algorithm of phase-shifting interferometry with arbitrary phase steps needs the image patches with equi-spaced fringes in the interferograms to determine the phase steps. In the application of this algorithm, the image patches can be obtained directly from the interferograms in some cases, or from the additional fringe patterns [20].

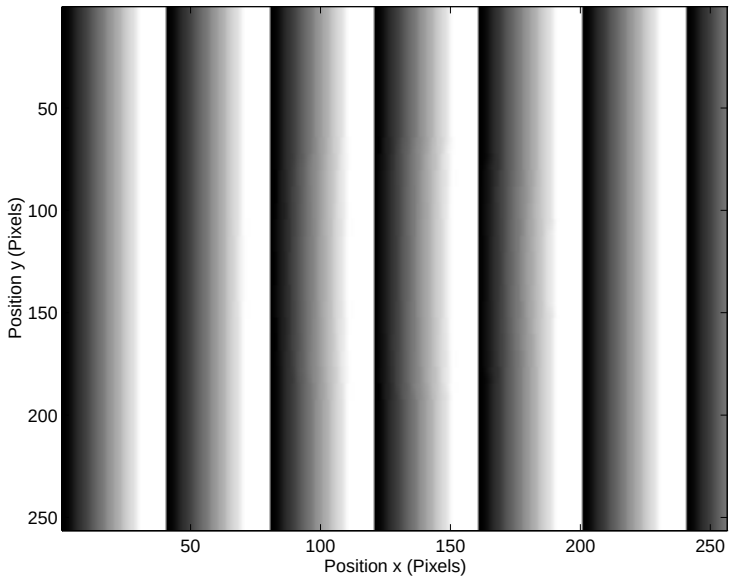

Figure 6.19: Wrapped phase map from the computer generated fringe patterns with phase step errors

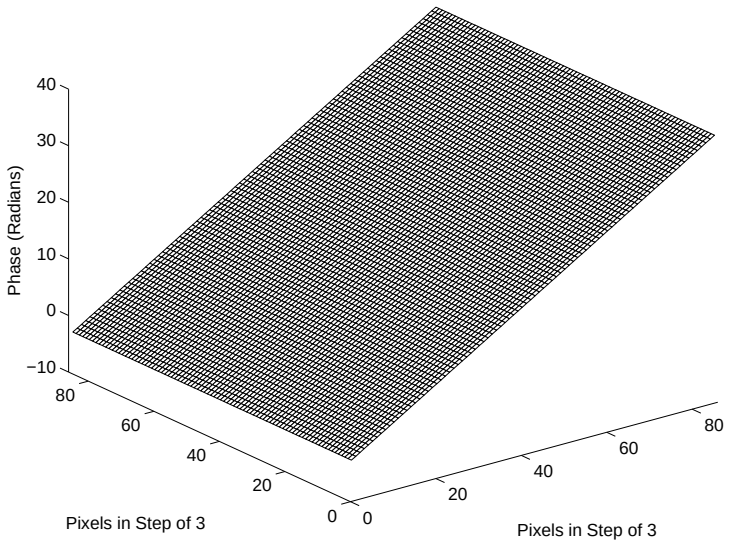

Figure 6.20: 3-D plot of the unwrapped phase from the computer generated fringe patterns with phase step errors

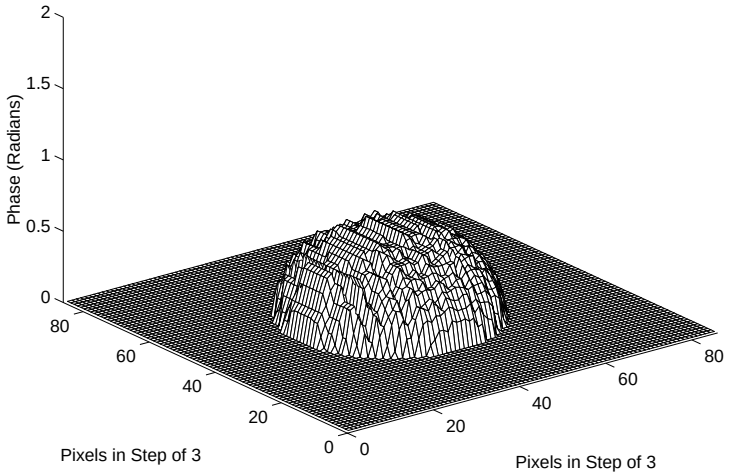

Figure 6.21: 3-D plot of the surface reconstructed from the computer generated fringe patterns with phase step errors

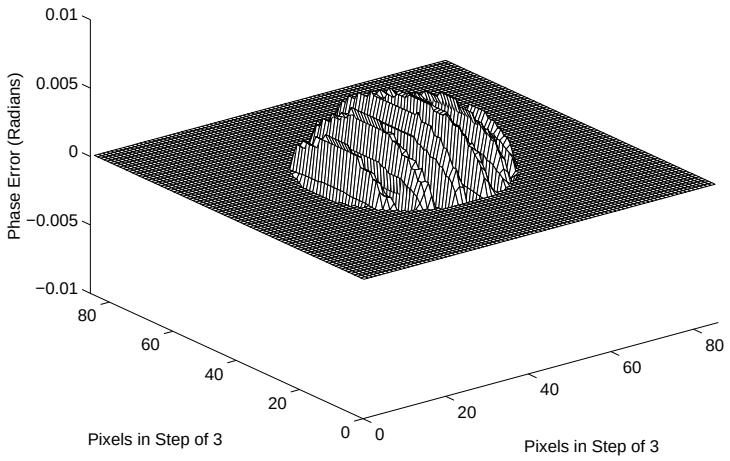

Figure 6.22: 3-D plot of the error distribution from the computer generated fringe patterns with phase step errors

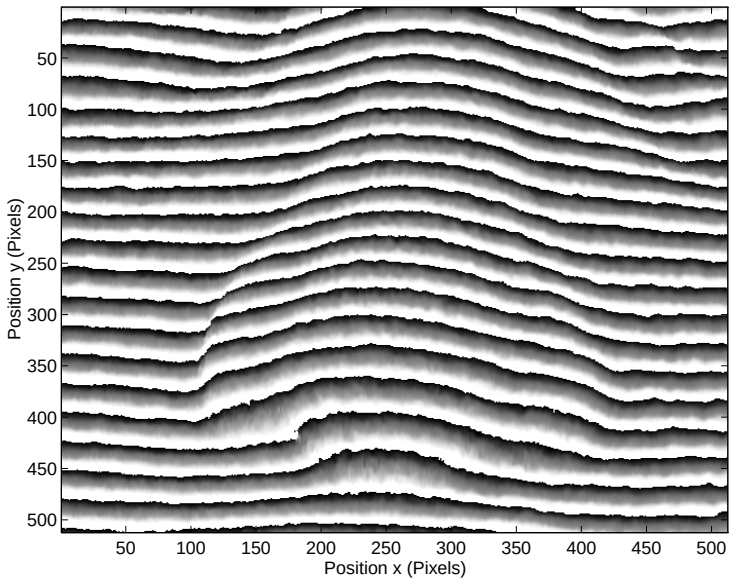

Figure 6.23: Wrapped phase map calculated from the three captured interferograms with phase step errors

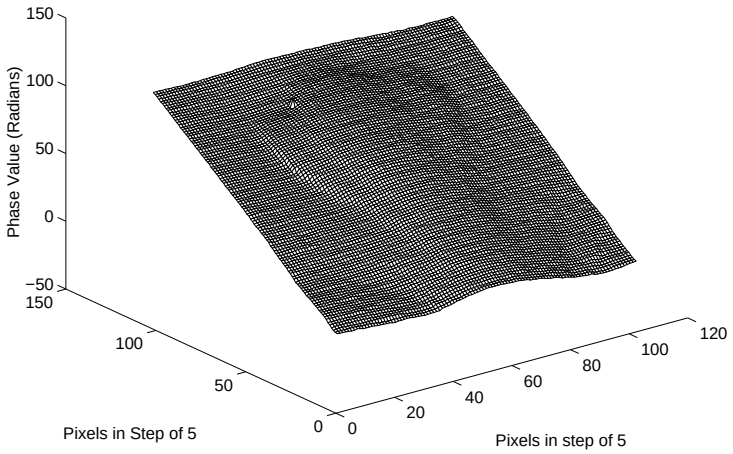

Figure 6.24: 3-D plot of the unwrapped phase obtained from the captured interferograms with phase step errors

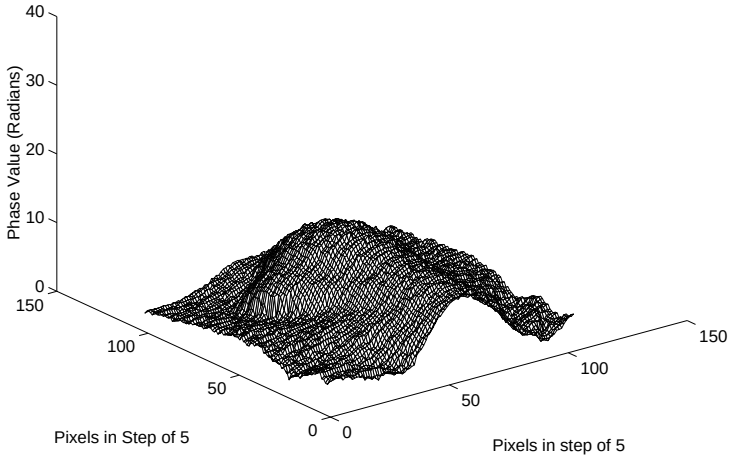

Figure 6.25: 3-D plot of the nose reconstructed from the captured interferograms with phase step errors

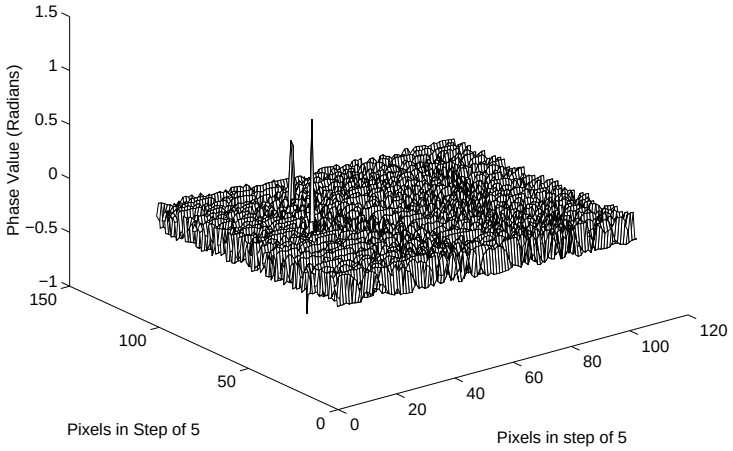

Figure 6.26: 3-D plot of the error distribution of the captured interferograms with phase step errors

6.5 Conclusion

In the algorithm of phase-shifting interferometry with arbitrary phase steps, the phase steps are taken as unknowns and they are determined by fringe pattern matching, so that it is inherently free from the phase step errors caused by air turbulence, vibration, thermal drift, mechanical drift, miscalibration and nonlinearity of the phase shifter. The computer simulation and experimental results have shown that fringe pattern matching is effective in phase-shifting interferometry to find the phase steps from the captured interferograms.

Bibliography

[1] K. Creath, "Phase-measurement interferometry techniques," *Prog. Opt.* **26**, 349-393 (1988).

[2] D. Malacara, "Phase shifting interferometry", *Revista Mexicana de Fisica* **36**, 6-22 (1990).

[3] D. Shough, "Beyond fringe analysis," *Proc. SPIE* **2003**, 208-223 (1993).

[4] C. Joenathan, "Phase-measuring interferometry: new methods and error analysis," *Appl. Opt.* **33**(19), 4147-4155 (1994).

[5] J.C. Wyant, B.F. Oreb, and P. Hariharan, "Testing aspherics using two-wavelength holography: use of digital electronic techniques," *Appl. Opt.* **23**(22), 4020-4023 (1984).

[6] P. Carré, "Installation et utilisation du comparateur photoélectrique et interférential du Bureau International des Poids et Measures," *Metrologia* **2**, 13-23 (1966).

[7] J.C. Wyant, "Use of an ac heterodyne lateral shear interferometer with real-time wavefront correction systems," *Appl. Opt.* **14**(11), 2622-2626 (1975).

[8] J. Schwider, R. Burow, K.-E. Elssner, J. Grzanna, R. Spolaczyk, and K. Merkel, "Digital wave-front measuring interferometry: some systematic error sources," *Appl. Opt.* **22**(21), 3421-3432 (1983).

[9] J.H. Bruning, D.R. Herriott, J.E. Gallagher, D.P. Rosenfeld, A.D. White, and D.J. Brangaccio, "Digital wavefront measuring interferometer for testing optical surfaces and lenses," *Appl. Opt.* **13**(11), 2693-2703 (1974).

[10] J.E. Greivenkamp, "Generalized data reduction for heterodyne interferometry," *Opt. Eng.* **23**(4), 350-352 (1984).

[11] Y. Cheng and J.C. Wyant, "Phase shifter calibration in phase shifting interferometry," *Appl. Opt.* **24**(18), 3049-3052 (1985).

[12] C. Ai and J.C. Wyant, "Effect of piezoelectric transducer nonlinearity on phase shift interferometry," *Appl. Opt.* **26**(6), 1112-1116 (1987).

[13] P. Hariharan, B.F. Oreb, and T. Eiju, "Digital phase-shifting interferometry: a simple error-compensating calculation algorithm," *Appl. Opt.* **26**(13), 2504-2505 (1987).

[14] J. Schwider, "Phase shifting interferometry: reference phase error reduction," *Appl. Opt.* **28**(18), 3889-3892 (1989).

[15] J. van Wingerden, H.J. Frankena, and C. Smorenburg, " Linear approximation for measurement errors in phase shifting interferometry," *Appl. Opt.* **30**(19), 2718-2729 (1991).

[16] C. Liu, "A method of eliminating the measurement error for phase shifting interferometry", *Proc. SPIE* **1983**, 706-707 (1993).

[17] J. Schwider, O. Falkenstorfer, H. Schreiber, A. Zoller, and N. Streibl, "New compensating 4-phase-algorithm for phase shifting interferometry," *Proc. SPIE* **1983**, 714-715 (1993).

[18] C. Liu, Z. Li, J. Chen, and X. Yu,"A new algorithm for phase shifting error,"*Proc. SPIE* **2003**, 431-434 (1993).

[19] K. Kinnstaetter, A.W. Lohmann, J. Schwider, and N. Streibl, "Accuracy of phase shifting interferometry," *Appl. Opt.* **27**(24), 5082-5089 (1988).

[20] G. Lai and T. Yatagai, "Generalized phase-shifting interferometry," *J. Opt. Soc. Am. A* **8**, 822-827 (1991).

[21] C.T. Farrell and M.A. Player, "Phase step measurement and variable step algorithms in phase-shifting interferometry," *Meas. Sci. Technol.* **3**, 953-958 (1992).

[22] C.T. Farrell and M.A. Player, "Phase-step insensitive algorithms for phase-shifting interferometry," *Meas. Sci. Technol.* **5**, 648-654 (1994).

[23] G.S. Han and S.W. Kim, "Numerical correction of reference phases in phase-shifting interferometry by iterative least-squares fitting," *Appl. Opt.* **33**(31), 7321-7325 (1994).

[24] I.B. Kong and S.W. Kim, "General algorithm of phase-shifting Interferometry by iterative least-squares fitting," *Opt. Eng.* **34**(1), 183-188 (1995).

[25] Z. Wang, P.J. Bryanston-Cross, and K.C. Tong, "Application of LCD in phase stepping," *Proc. International Conference on Fringe Analysis*, York University, 66-70 (1994).

Chapter 7

An Algorithm of Spatial Phase-Shifting Interferometry

7.1 Introduction

Phase-shifting interferometry (PSI) [1, 2, 3] includes the techniques of temporal PSI [4, 5, 6, 7, 8, 9], parallel PSI [10], and spatial PSI [11, 12, 13, 14, 15], as introduced in chapter 1. These techniques are different from each other mainly in phase shifting methods, accuracy, processing time, and the number of fringe patterns required for the phase calculation.

It is known that temporal PSI captures at least three fringe patterns with different phase steps in a temporal sequence, and it is now a well-established technique for high accuracy fringe pattern analysis. Parallel PSI acquires three or four phase stepped fringe patterns with three or four cameras at the same time. The technique of parallel PSI is useful for dynamic measurement, but its imaging system is complicated and it is difficult to align the system. Compared with temporal PSI and parallel PSI, spatial PSI uses only one captured fringe pattern to calculate the phase. This technique has a low accuracy in theory, but it is inherently free from the phase shift error, and it is appropriate for dynamic measurement in

comparison with temporal PSI. In addition, the imaging system of spatial PSI is simple and it can also be performed using the same imaging system as temporal PSI.

This chapter presents a spatial PSI algorithm. In this algorithm, one fringe pattern is captured by a CCD camera, and the other two shifted fringe patterns with the phase steps of 90^o and 180^o are generated by computer according to the features of light intensity distributions and the method of interpolation. The phase is then calculated by a standard three-step algorithm of temporal PSI. Unlike the four-pixel [11, 12, 13] and multi-pixel [14, 15] algorithms of spatial PSI, it is assumed that the objective phases are linearly changed in one fringe period and the fringe period is not treated as a constant in this algorithm. The algorithm of spatial PSI presented in this chapter was examined in an experiment for 3-D object reconstruction. The phase steps of the computer generated fringe patterns were also computed by fringe pattern matching, and the experimental results from spatial PSI and temporal PSI were obtained in the experiment.

In section 7.2, the principle of the spatial PSI algorithm based on interpolation is introduced. Section 7.3 illustrates some experimental results from the use of the spatial PSI algorithm. The discussion and conclusion of this chapter are given in sections 7.4 and 7.5, respectively.

7.2 Principle

In phase-shifting interferometry, the intensity distribution of two-beam interference fringe pattern I(i, j) can be expressed as

$$\mathrm{I(i,j)} = \mathrm{a(i,j)} + \mathrm{b(i,j)}\cos[\phi(\mathrm{i,j}) - \phi_{\mathrm{r}}], \quad \mathrm{i,j} = 0, 1, 2, ... \tag{7.1}$$

where a(i,j) is the background illumination, b(i,j) is the modulation of the fringes, $\phi(\mathrm{i},\mathrm{j})$ is the phase related to the physical quantity to be measured, and ϕ_r is a reference phase.

For a three-step PSI algorithm, the light intensity distributions of the three captured fringe patterns with the phase steps of 0^o, 90^o and 180^o can be written as

$$\mathrm{I}_1(\mathrm{i},\mathrm{j}) = \mathrm{a}(\mathrm{i},\mathrm{j}) + \mathrm{b}(\mathrm{i},\mathrm{j})\cos\phi(\mathrm{i},\mathrm{j}) \tag{7.2}$$

$$\mathrm{I}_2(\mathrm{i},\mathrm{j}) = \mathrm{a}(\mathrm{i},\mathrm{j}) + \mathrm{b}(\mathrm{i},\mathrm{j})\sin\phi(\mathrm{i},\mathrm{j}) \tag{7.3}$$

$$\mathrm{I}_3(\mathrm{i},\mathrm{j}) = \mathrm{a}(\mathrm{i},\mathrm{j}) - \mathrm{b}(\mathrm{i},\mathrm{j})\cos\phi(\mathrm{i},\mathrm{j}) \tag{7.4}$$

and the phase can be calculated by

$$\phi(\mathrm{i},\mathrm{j}) = \arctan\frac{(\mathrm{I}_3 - \mathrm{I}_2) + (\mathrm{I}_1 - \mathrm{I}_2)}{(\mathrm{I}_3 - \mathrm{I}_1)} \tag{7.5}$$

Based on the analysis of the features of sinusoidal signals and the method of interpolation, the light intensities of the two shifted fringe patterns generated by computer can be expressed as

$$\mathrm{I}_2'(\mathrm{i},\mathrm{j}) = \frac{1}{2}[\mathrm{I}_1(\mathrm{i},\mathrm{j}-\frac{\mathrm{T}}{4}) + \mathrm{I}_3'(\mathrm{i},\mathrm{j}+\frac{\mathrm{T}}{4})] \tag{7.6}$$

$$\mathrm{I}_3'(\mathrm{i},\mathrm{j}) = \frac{1}{2}[\mathrm{I}_1(\mathrm{i},\mathrm{j}-\frac{\mathrm{T}}{2}) + \mathrm{I}_1(\mathrm{i},\mathrm{j}+\frac{\mathrm{T}}{2})] \tag{7.7}$$

where $\mathrm{I}_2'(\mathrm{i},\mathrm{j})$ and $\mathrm{I}_3'(\mathrm{i},\mathrm{j})$ are the light intensity distributions with the phase steps of 90^o and 180^o, respectively. T is the effective fringe period in the captured fringe pattern and it may not be a constant in this case.

In equations 7.6 and 7.7, it is assumed that the fringes are horizontal in the

interferograms. For the fringes being vertical in the interferograms, the intensities of the two shifted fringe patterns can also be written as

$$I_2^{'}(i,j) = \frac{1}{2}[I_1(i - \frac{T}{4}, j) + I_3^{'}(i + \frac{T}{4}, j)] \tag{7.8}$$

$$I_3^{'}(i,j) = \frac{1}{2}[I_1(i - \frac{T}{2}, j) + I_1(i + \frac{T}{2}, j)] \tag{7.9}$$

Let $\phi^{'}(i,j)$ be the phase calculated by $I_1^{'}$, $I_2^{'}$ and $I_3^{'}$ in stead of $\phi(i,j)$, I_1, I_2 and I_3 in equation 7.5. The new phase expression is

$$\phi^{'}(i,j) = \arctan\frac{(I_3^{'} - I_2^{'}) + (I_1^{'} - I_2^{'})}{(I_3^{'} - I_1^{'})} \tag{7.10}$$

where $I_1^{'} = I_1$.

For linear approximation, equations 7.6, 7.7, 7.8, 7.9, and 7.10 can be rewritten as

$$I_2^{'}(i,j) \approx I_2(i,j) \tag{7.11}$$

$$I_3^{'}(i,j) \approx I_3(i,j) \tag{7.12}$$

$$\phi^{'}(i,j) \approx \arctan\frac{(I_3 - I_2) + (I_1 - I_2)}{(I_3 - I_1)} \tag{7.13}$$

or

$$I_1^{'}(i,j) = a(i,j) + b(i,j)\cos\phi(i,j) \tag{7.14}$$

$$I_2^{'}(i,j) \approx a(i,j) + b(i,j)\sin\phi(i,j) \tag{7.15}$$

$$I_3^{'}(i,j) \approx a(i,j) - b(i,j)\cos\phi(i,j) \tag{7.16}$$

$$\phi^{'}(i,j) \approx \phi(i,j) \tag{7.17}$$

In the above, the linear changes of the background illumination, the modulation of the fringes and the objective phases in one fringe period are assumed. From equation 7.17, the phase $\phi(\mathrm{i},\mathrm{j})$ can be computed using

$$\phi(\mathrm{i},\mathrm{j}) \approx \arctan\frac{(\mathrm{I}_3^{'} - \mathrm{I}_2^{'}) + (\mathrm{I}_1 - \mathrm{I}_2^{'})}{(\mathrm{I}_3^{'} - \mathrm{I}_1)} \tag{7.18}$$

where I_1 is the fringe pattern captured by a CCD camera, and $\mathrm{I}_2^{'}$ and $\mathrm{I}_3^{'}$ are the fringe patterns with the phase steps of 90° and 180° which are generated by computer from equations 7.6 and 7.7 for the fringe patterns with horizontal fringes, or equations 7.8 and 7.9 for the fringe patterns with vertical fringes. It should be noted that equation 7.18 is valid under the condition of linear approximation.

The principle of the spatial PSI algorithm based on the method of interpolation has been described above. The procedure for the phase calculation may be summarised as follows:

- Capture one fringe pattern with the roughly horizontal or vertical fringes.
- Detect the peak points and valley points in the fringe pattern.
- Calculate $\mathrm{I}_3^{'}(\mathrm{i},\mathrm{j})$ period by period and line by line using equation 7.7 for the fringe patterns in which the fringes are horizontal or using equation 7.9 for the fringe patterns in which the fringes are vertical.
- Determine the peak points and valley points in fringe pattern $\mathrm{I}_3^{'}(\mathrm{i},\mathrm{j})$.
- Compute $\mathrm{I}_2^{'}(\mathrm{i},\mathrm{j})$ period by period and line by line using equation 7.6 for the fringe patterns in which the fringes are horizontal or using equation 7.8 for the fringe patterns in which the fringes are vertical.
- Find the wrapped phase distribution from equation 7.18.
- Unwrap the phase distribution.
- Reconstruct the objective phase.

7.3 Experimentation

The algorithm of spatial PSI was examined in the system for reconstructing 3-D object shapes as shown in figure 6.13 in chapter 6. In the experiment, the fringe patterns $I'_2(i,j)$ and $I'_3(i,j)$ were generated by computer, and the nose of a statue was used as a test object.

Figure 7.1 shows one captured fringe pattern. The two fringe patterns with the phase steps of 90^o and 180^o calculated by computer from equations 7.6 and 7.7 are shown in figures 7.2 and 7.3. Figures 7.4 and 7.5 show the wrapped and unwrapped phases of the nose computed from one captured fringe pattern, and the 3-D plot is given in figure 7.6. Two of the MATLAB programmes for spatial PSI are shown in appendix E.

In comparison with the temporal PSI technique, the nose of a statue was captured with the phase steps of 0^o, 90^o and 180^o. The 3-D plot of the nose obtained from temporal PSI is shown in figure 7.7. Figure 7.8 shows the difference phase distribution between spatial PSI and temporal PSI. The flow chart of MATLAB programming for spatial PSI is shown in figure 7.9.

The phase shifts between the captured fringe pattern and computer generated fringe patterns were also examined by fringe pattern matching. The phase curves obtained from the mean-square difference calculations are shown in figure 7.10. The phase steps of the two fringe patterns as shown in figures 7.2 and 7.3 are 93.4^o and 180.0^o. Figure 7.11 shows the wrapped phase computed from the fringe patterns with the phase steps of 0^o, 93.4^o and 180.0^o, and the 3-D plot of the unwrapped phase is shown in figure 7.12. Figure 7.13 shows the 3-D plot of the nose reconstructed from the fringe patterns with the phase steps of 0^o, 93.4^o and 180.0^o. The difference phase distribution from the captured and computer generated fringe patterns shown in figure 7.14. The RMS value between the difference phase distributions as shown in figures 7.8 and 7.14 is about 0.02

radians.

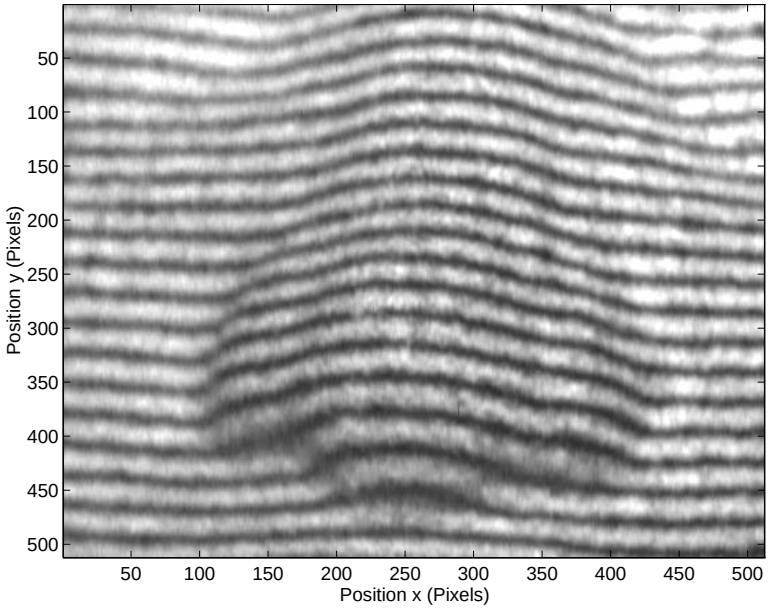

Figure 7.1: One captured fringe pattern

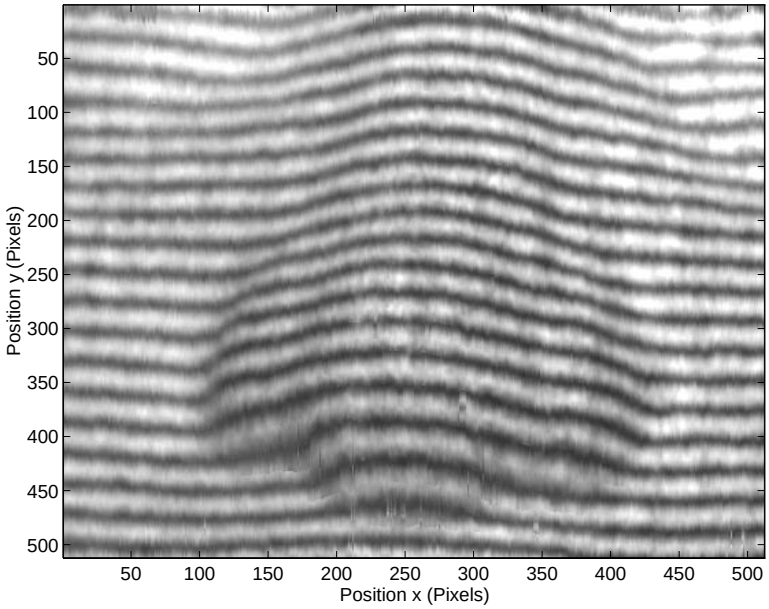

Figure 7.2: Computer generated fringe pattern with a phase shift of 90^{o}

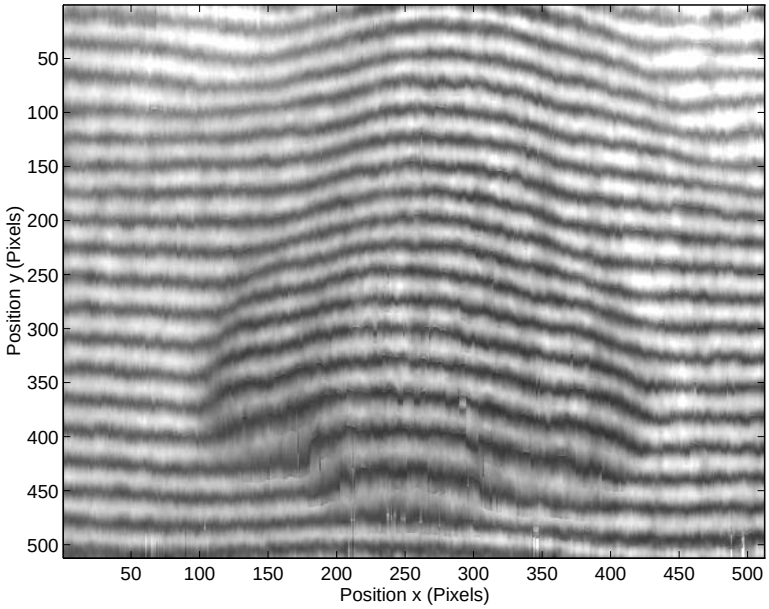

Figure 7.3: Computer generated fringe pattern with a phase shift of 180°

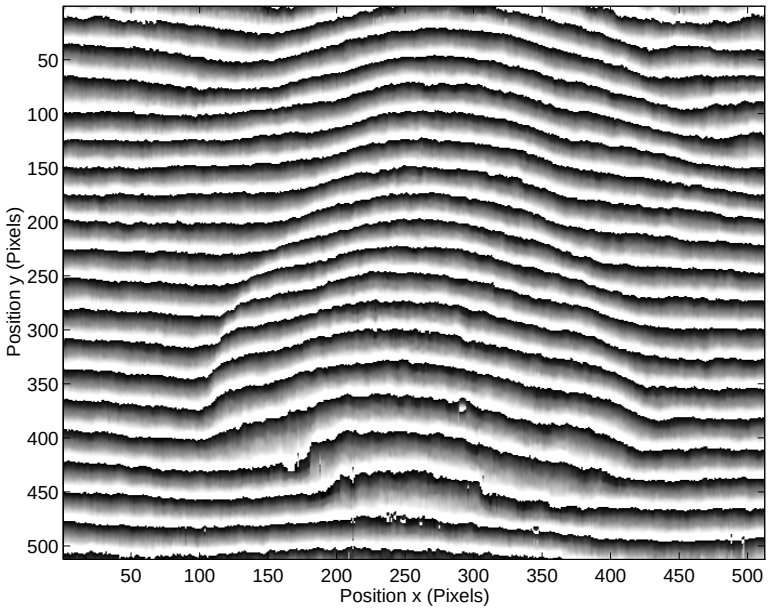

Figure 7.4: Wrapped phase of the nose computed from one captured fringe pattern

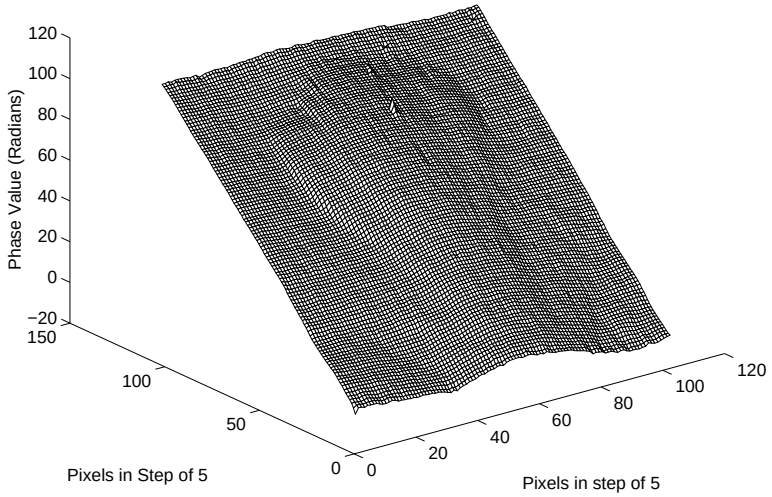

Figure 7.5: 3-D plot of the unwrapped phase of the nose obtained from one captured fringe pattern

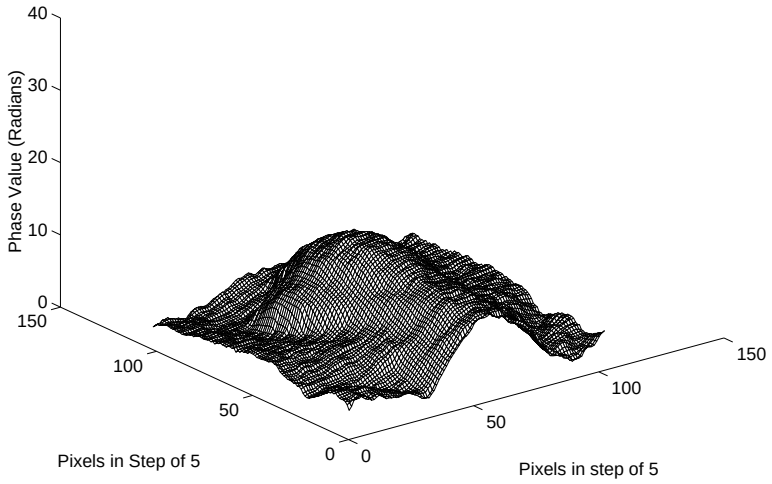

Figure 7.6: 3-D plot of the nose reconstructed from one captured fringe pattern

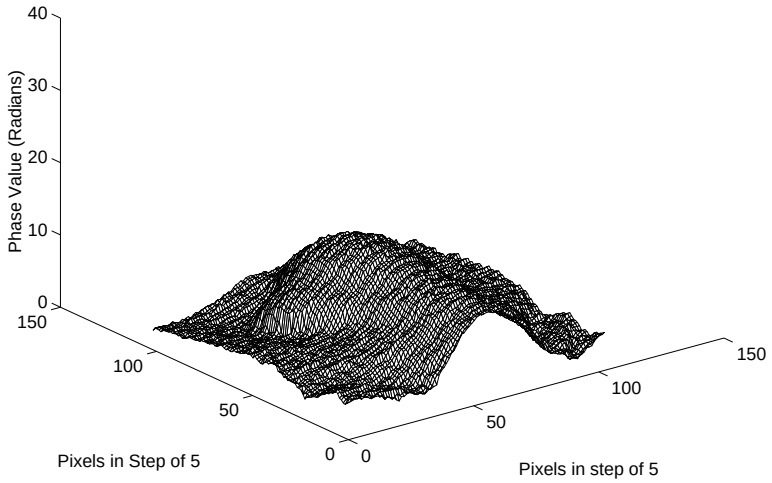

Figure 7.7: 3-D plot of the nose reconstructed from temporal PSI

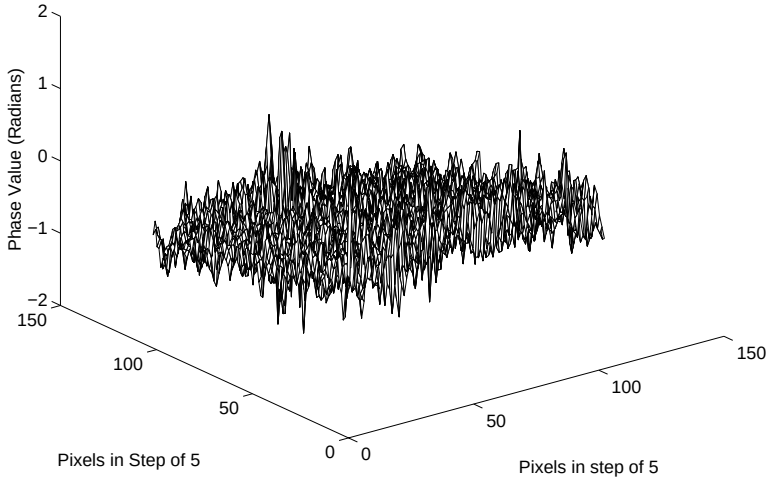

Figure 7.8: Difference phase distribution between spatial PSI and temporal PSI

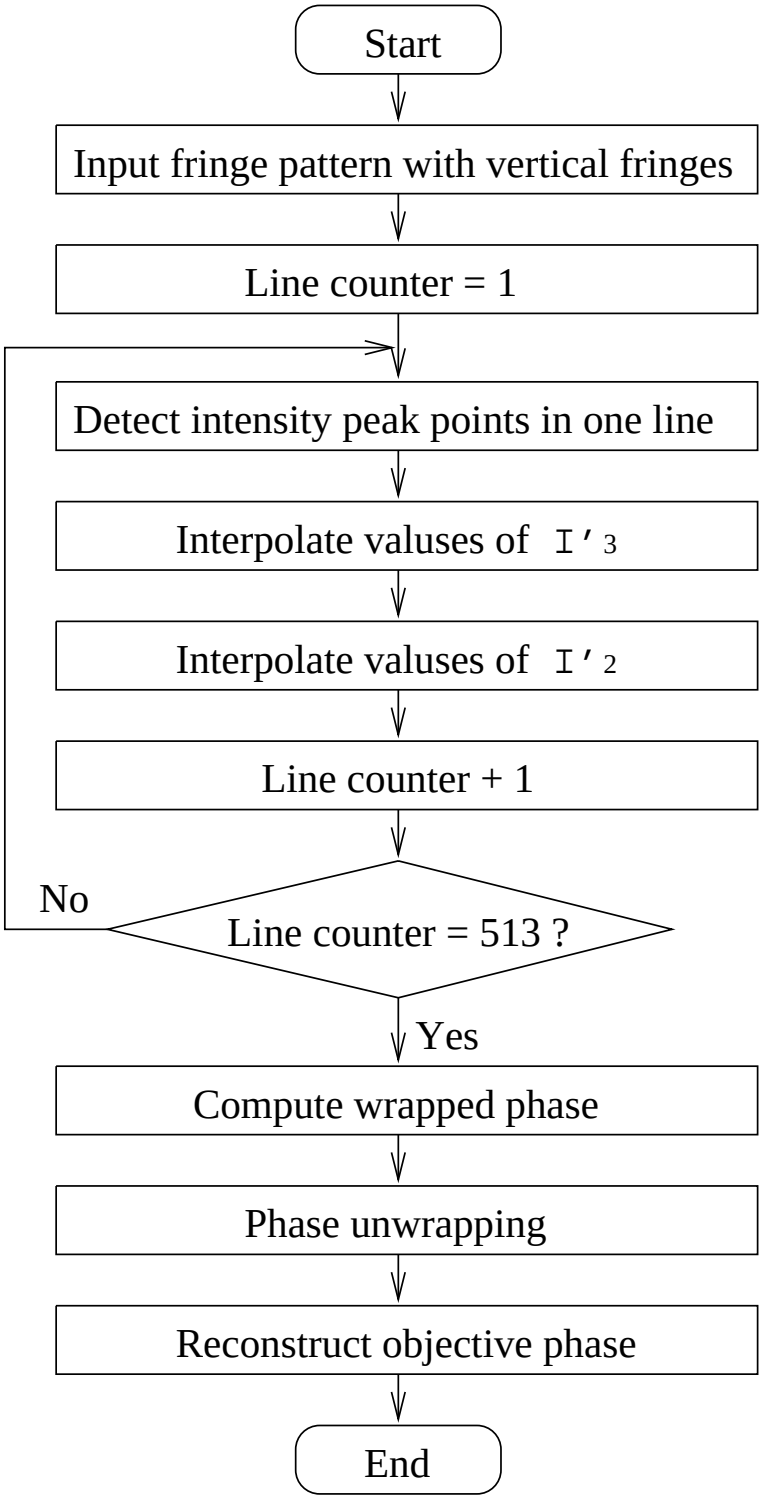

Figure 7.9: Flow chart of MATLAB programming for spatial PSI

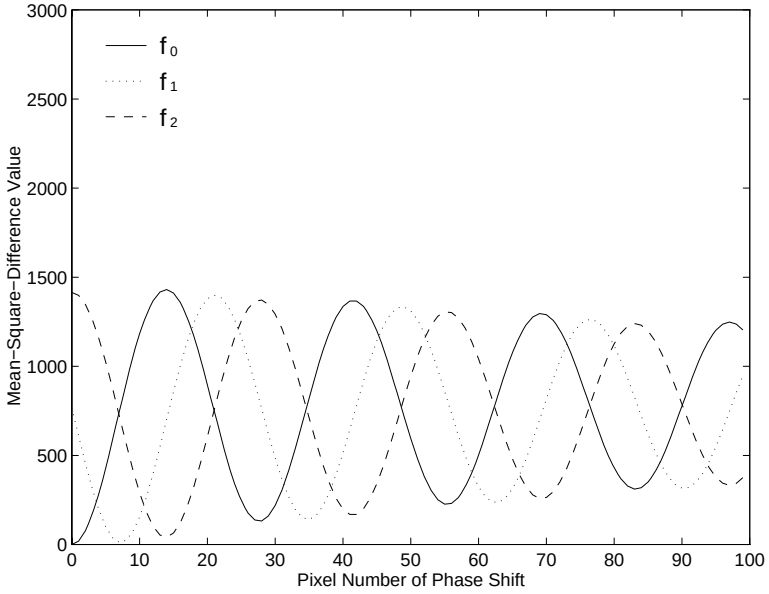

Figure 7.10: Phase curves obtained from fringe pattern matching

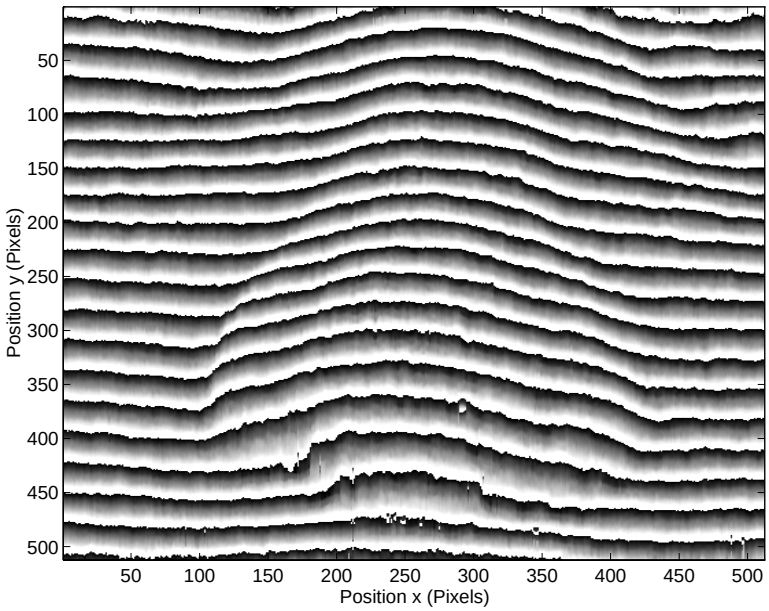

Figure 7.11: Wrapped phase computed from the fringe patterns with the phase steps of 0^o, 93.4^o and 180.0^o

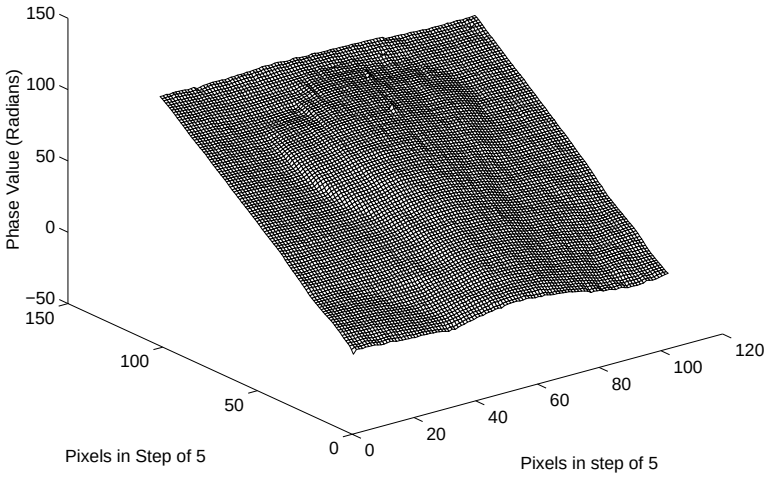

Figure 7.12: 3-D plot of the unwrapped phase obtained from the fringe patterns with the phase steps of 0°, 93.4° and 180.0°

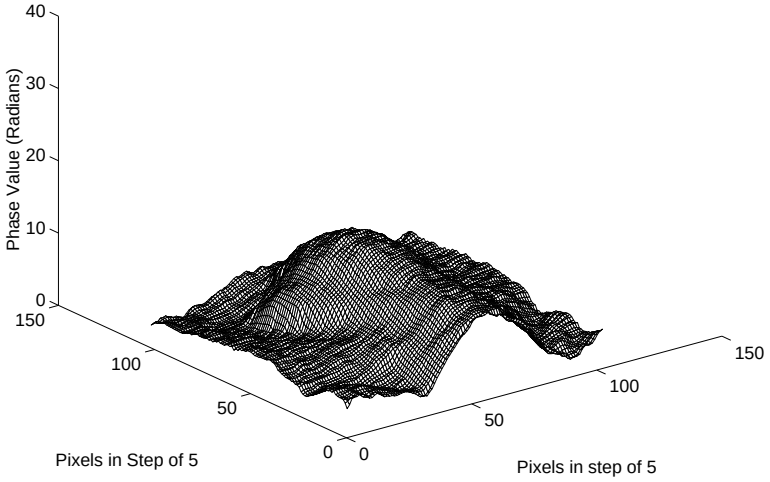

Figure 7.13: 3-D plot of the nose reconstructed from the fringe patterns with the phase steps of 0°, 93.4° and 180.0°

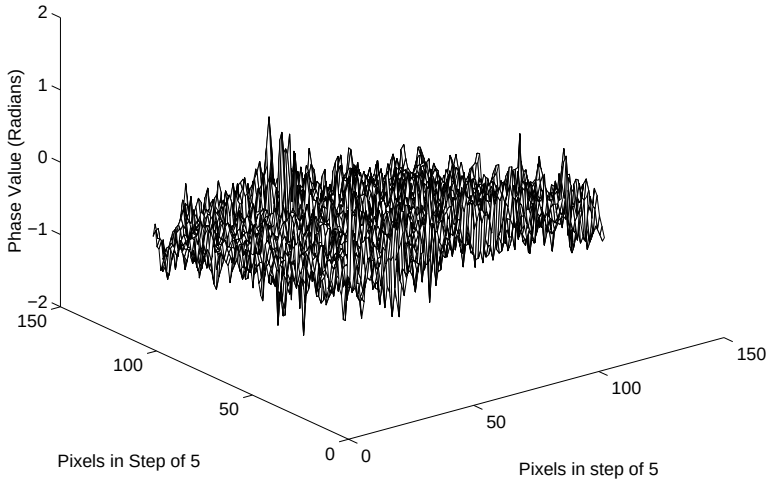

Figure 7.14: Difference phase distribution from the captured and computer generated fringe patterns

7.4 Discussion

In theory, the phase error caused by the algorithm of spatial PSI is

$$\Delta\phi(\mathrm{i},\mathrm{j}) = \phi(\mathrm{i},\mathrm{j}) - \phi^{'}(\mathrm{i},\mathrm{j}) \tag{7.19}$$

or

$$\Delta\phi(\mathrm{i},\mathrm{j}) = \arctan\frac{(\mathrm{I}_3 - \mathrm{I}_2) + (\mathrm{I}_1 - \mathrm{I}_2)}{(\mathrm{I}_3 - \mathrm{I}_1)} - \arctan\frac{(\mathrm{I}_3^{'} - \mathrm{I}_2^{'}) + (\mathrm{I}_1 - \mathrm{I}_2^{'})}{(\mathrm{I}_3^{'} - \mathrm{I}_1)} \tag{7.20}$$

It is clear that this algorithm needs a high spatial frequency to achieve a high accuracy of measurement since the phase $\phi^{'}(\mathrm{i},\mathrm{j})$ theoretically approaches to $\phi(\mathrm{i},\mathrm{j})$ when the effective fringe period T approaches to zero. This means that the high accuracy of measurement can be achieved when the spatial frequency is

high enough compared with the changes of the background illumination, the modulation of the fringes and the objective phases. In practice, however, the spatial frequency is limited by the resolution of the imaging sensor.

It can be seen, from equations 7.6 and 7.7, that the big error may occur on the borders of the phase map. This is because the data on the borders cannot be guaranteed to be as accurate as the data obtained from the equations if the two computer generated fringe patterns keep the same size as the captured fringe pattern in this algorithm. Therefore, the data on the borders normally have a lower accuracy compared with the other data in the fringe pattern.

In addition, interpolation is used for generating the new fringe patterns as the fringe period is not a constant in this algorithm. In practice, the fringe period is often not an integer and the peak points of the computer generated fringes are also not guaranteed to be integers. Therefore, using interpolation to compute the two fringe patterns is necessary in this algorithm.

7.5 Conclusion

The algorithm of spatial PSI presented in this chapter is inherently free from the phase shift errors caused by air turbulence, vibration, thermal drift, mechanical drift, miscalibration and nonlinearity of the phase shifter since it uses only one captured fringe pattern and no phase shifter is required in the system. In practice, the algorithm is particularly appropriate for real-time fringe pattern analysis and dynamic measurement.

Bibliography

[1] K. Creath, "Phase-measurement interferometry techniques," *Prog. Opt.* **26**, 349-393 (1988).

[2] D. Shough, "Beyond fringe analysis," *Proc. SPIE* **2003**, 208-223 (1993).

[3] C. Joenathan, "Phase-measuring interferometry : new methods and error analysis," *Appl. Opt.* **33**(19), 4147-4155 (1994).

[4] J.C. Wyant, B.F. Oreb, and P. Hariharan, "Testing aspherics using two-wavelength holography : use of digital electronic techniques," *Appl. Opt.* **23**(22), 4020-4023 (1984).

[5] P. Carré, "Installation et utilisation du comparateur photoélectrique et interférential du Bureau International des Poids et Measures," *Metrologia* **2**, 13-23 (1966).

[6] J.C. Wyant, "Use of an ac heterodyne lateral shear interferometer with real-time wavefront correction systems," *Appl. Opt.* **14**(11), 2622-2626 (1975).

[7] J. Schwider, R. Burow, K -E, Elssner, J. Grzanna, R. Spolaczyk, and K. Merkel, "Digital wave-front measuring interferometry : some systematic error sources," *Appl. Opt.* **22**(21), 3421-3432 (1983).

[8] J.H. Bruning, D.R. Herriott, J.E. Gallagher, D.P. Rosenfeld, A.D. White, and D.J. Brangaccio, "Digital wavefront measuring interferometer for testing optical surfaces and lenses," *Appl. Opt.* **13**(11), 2693-2703 (1974).

[9] J.E. Greivenkamp, "Generalized data reduction for heterodyne interferometry," *Opt. Eng.* **23**(4), 350-352 (1984).

[10] C.L. Koliopoulos and M. Jensen, "Real-time video rate phase processor," *Proc. SPIE* **2003**, 264-268 (1993).

[11] D.M. Shough, O.Y. Kwon, and D.F. Leary, "High-speed interferometric measurement of aerodynamic phenomena," *Proc. SPIE* **1221**, 394-403 (1990).

[12] M. Kujawińska and J. Wójciak, "Spatial-carrier phase shifting technique of fringe pattern analysis," *Proc. SPIE* **1508**, 61-67 (1991).

[13] R. Gu and T. Yoshizawa, "Talbot projected 3-D profilometry by means of one step phase-shift algorithms," *Proc. SPIE* **1720**, 470-477 (1992).

[14] P.H. Chan, P.J. Bryanston-Cross, and S.C. Parker, "Spatial phase stepping method of fringe pattern analysis," *Opt. Lasers Eng.* **23**, 343-354 (1995).

[15] P.H. Chan, P.J. Bryanston-Cross, and S.C. Parker, "Analysis of fringe pattern using a spatial phase stepping method with automatic phase unwrapping," *Meas. Sci. Technol.* **6**, 1250-1259 (1995).

Chapter 8

General Conclusions and Further Work

8.1 General Conclusions

In this section, the approaches in optical interferometry presented in this thesis are outlined on the basis of the work described in chapters 2, 3, 4, 5, 6 and 7. Fringe pattern matching is presented as a powerful technique for phase difference determination. The method of displacement measurement based on Young's experiment is considered as a possible way for displacement measurement in a machine vision system. The algorithm of phase-shifting interferometry with arbitrary phase steps is treated as an effective method for determining phase steps in temporal PSI. In the last subsection, the spatial PSI algorithm based on interpolation is taken as a useful approach to spatial PSI.

8.1.1 Fringe Pattern Matching : A Powerful Technique for Phase Difference Determination in Optical Interferometry

Fringe pattern matching is a powerful technique for phase difference determination in optical interferometry. Chapter 2 has presented the principle of fringe pattern matching in the determination of phase difference. It has been known that the matching process provides a good quality of phase curves from which the phase differences can be seen clearly with a high signal to noise ratio. The exact phase difference can be theoretically determined by detecting the minimum of the mismatch function or the peak points from the phase curves. In practice, however, it is difficult, or impossible to find the minimum or peak points with subpixel resolution from the direct fringe pattern matching due to the finite resolutions of the imaging sensor and the presence of noise. In this case, the methods of linear interpolation and polynomial curve fitting can be used to achieve subpixel resolution from the phase curves. The calculation of linear interpolation method is simpler than that of polynomial curve fitting method. The computer simulation and experiment have shown that fringe pattern matching is powerful in the determination of phase difference between the interferograms with equispaced fringes. This technique has the advantage of high tolerance to noise due to the region-based matching and its effect of averaging noise.

The effect of image patch size on phase difference determination by fringe pattern matching has been discussed from the statistical point of view in chapter 3. The theoretical results have been examined by computer simulation and experiment. The computer simulation and experimental results, which are accordant with equations 3.14 and 3.21, have proved that the larger image patches used in the matching process have a better accuracy in the presence of noise. The signal to noise ratio is significantly improved due to the fact that each value in the phase curves is obtained from averaging M$\times$N pixels if the image patches with the size

of M×N pixels are used in the matching process. The advantage of averaging noise of this technique makes it powerful in the determination of phase difference from the statistical point of view.

The measurement of electrostatic force displacement made by the fibre-optic interferometer system as described in chapter 4 is an example of the use of fringe pattern matching. In the measurement, the quality of the fringe pattern was badly affected by the non-ideal optical surface of the cantilever of the capacitive sensor from which several hundreds of noisy interferograms were obtained. The fringe pattern matching was then used for detecting the displacement information from the hundreds of noisy interferograms. The experiment has shown that fringe pattern matching is effective in displacement measurement and the advantage of high resistance to noise makes it suitable for the measurement of displacement in the presence of noise.

In addition, the computer simulation and experimental results from the computer generated and captured interferograms indicate that the larger image patches have less distortion of the phase curves and higher signal to noise ratio in the presence of noise, but they need more processing time. In the application of fringe pattern matching, the size of image patch can be selected according to the shifting range of the image patch in the matching process, the required accuracy and processing time. It should be noted that the achievable accuracy in the determination of phase difference by fringe pattern matching is basically dependent on the quality of fringe patterns.

8.1.2 Fringe Pattern Matching : A Possible Way for Displacement Measurement in Machine Vision Systems

The method of displacement measurement based on Young's experiment has been illustrated in chapter 5. In the method, the fringe spacing is calculated by fringe pattern matching and the displacement is then determined according to the fringe spacing equation from Young's experiment. The fringe spacing with subpixel accuracy has been achieved from fringe pattern matching together with linear interpolation.

It is known, from the computer simulation in chapter 5, that the accuracy of displacement measurement is basically dependent on imager resolutions. The higher resolutions of the imaging sensor have achieved a better accuracy in the simulation. The accuracy of displacement measurement in practice is also affected by other error sources such as the unequally spaced fringes and non-uniform background illumination although fringe pattern matching has the advantage of averaging noise. The error may be reduced by careful calibration, but the object shape change will make the measurement complicated and difficult.

In conclusion, fringe pattern matching provides a possible way for measuring displacement in a machine vision system.

8.1.3 Fringe Pattern Matching : An Effective Method for Determining Phase Steps in Temporal PSI

The phase error from inaccurate phase steps is a significant problem in temporal phase-shifting interferometry. In theory, the desired phase steps can be introduced by a phase shifter in an experiment. In practice, however, it is difficult, or impossible to acquire the phase steps as accurately as expected due to air turbu-

lence, vibration, thermal drift, mechanical drift, miscalibration and nonlinearity of the phase shifter. In the algorithm of phase-shifting interferometry with arbitrary phase steps described in chapter 6, the phase steps are taken as unknowns and they are determined by fringe pattern matching. The algorithm is inherently free from the phase step errors since it relies solely on the fringe pattern itself in the determination of the phase step.

It is clear that the algorithm of phase-shifting interferometry with arbitrary phase steps needs the image patches with equi-spaced fringes to find the phase steps. In practical applications, the image patches can be obtained directly from the interferograms in some cases, or from the additional fringe patterns [1].

In conclusion, fringe pattern matching is effective in phase-shifting interferometry to determine the phase steps from the interferograms in temporal PSI.

8.1.4 Interpolation : A Useful Approach to Spatial PSI

The algorithm of spatial PSI based on interpolation has been discussed in chapter 7. In the algorithm, one fringe pattern is captured by CCD camera, and the other two shifted fringe patterns with the phase steps of 90^o and 180^o are generated by computer according to the features of light intensity distributions and the method of interpolation. The phase is then calculated by a standard three-step algorithm of temporal PSI. The experimental results have proved that the algorithm is meaningful for fringe pattern analysis using only one interferogram.

Unlike the other algorithms of spatial PSI, it is assumed that the objective phase is linearly changed in one fringe period and the fringe period is not treated as a constant in the algorithm presented in this thesis. Therefore, the spatial PSI algorithm based on interpolation is a useful approach to spatial PSI.

8.2 Further Work

In this section, three pieces of work for future research, which are the methods of phase difference determination by knowledge-based fitting, SNR (signal to noise ratio) estimation of fringe patterns and flexible fringe pattern analysis package, are briefly proposed.

8.2.1 Phase Difference Determination by Knowledge-Based Fitting

It is known that the fringe intensity distribution is theoretically a sinusoidal. This means that each row in the captured fringe pattern stands for a sine signal if the fringes are vertical. Therefore, it is possible to find the sine signal based on the captured fringe pattern in a least-squares sense, or in other words, the phase difference between fringe patterns may be obtained from the method of least-squares fitting [2, 3].

Assuming that the fringe spacing P is a constant in fringe patterns, the standard light intensity can be expressed as

$$I_{sn}(i,j) = a_{sn}(i,j) + b_{sn}(i,j)\cos[\frac{2\pi i}{P} + \alpha_{sn}(i,j)], \quad n = 0,1,2,...;\ i,j = 0,1,2,... \tag{8.1}$$

where $a_{sn}(i,j)$ is the background illumination, $b_{sn}(i,j)$ is the modulation of the fringes, and $\alpha_{sn}(i,j)$ is the reference phase.

For a captured fringe pattern with equi-spaced fringes, the squared sum of intensity differences is

$$F_{lsfn}(a_{sn}, b_{sn}, \alpha_{sn}) = \sum_{i=0}^{N-1}[I_{cn}(i,j) - I_{sn}(i,j)]^2, \quad n = 0,1,2,...;\ j = 0,1,2,...,M-1 \tag{8.2}$$

where $I_{cn}(i,j)$ is the captured fringe pattern. The size of fringe pattern is $M \times N$ pixels in equation 8.2.

In a least-squares sense, the values of a_{sn}, b_{sn} and α_{sn} in equation 8.1 can be obtained by setting the following partial derivatives to zero

$$\frac{\partial F_{lsfn}}{\partial a_{sn}} = 0, \quad n = 0, 1, 2, ... \tag{8.3}$$

$$\frac{\partial F_{lsfn}}{\partial b_{sn}} = 0, \quad n = 0, 1, 2, ... \tag{8.4}$$

$$\frac{\partial F_{lsfn}}{\partial \alpha_{sn}} = 0, \quad n = 0, 1, 2, ... \tag{8.5}$$

The reference phase α_{sn} can be therefore found from equations 8.3, 8.4 and 8.5. The phase difference between fringe patterns can then be calculated by subtracting the two corresponding reference phases, i.e. α_{sn+1}-α_{sn}.

It is clear that the least-squares fitting technique discussed above is in effect a technique of knowledge-based fitting. In addition, this method can be directly applied to fit the phase curve obtained from fringe pattern matching. Therefore, higher accuracy of phase difference determination can be expected to be achieved from the knowledge-based fitting in comparison with the method of fringe pattern matching presented in this thesis.

8.2.2 SNR Estimation of Fringe Patterns

The method of phase difference determination by fringe pattern matching is also dependent on the quality of fringe pattern, and the SNR of fringe pattern is a measure of the quality of fringe pattern, so that the SNR of fringe pattern is directly related to the achievable accuracy of phase difference determination [4].

On the basis of knowledge-based fitting approach to phase difference determination in optical interferometry, equation 8.1 stands for the ideal fringe pattern that is expected in the interference. In this case, the noise distribution can be found from the difference between the captured fringe pattern and the fringe pattern expressed by equation 8.1. Therefore, the SNR of the captured fringe pattern can be estimated in a least-squares sense.

8.2.3 Flexible Fringe Pattern Analysis Package

The new approaches in optical interferometry, which have been presented in this thesis, are all fringe pattern-based. The problem is that all the functions of image processing are performed by MATLAB for the particular applications and the MATLAB programmes are not appropriate for real-time or *in-situ* fringe pattern analysis. Therefore, a flexible fringe pattern analysis package programmed by C language is expected for various applications in real-time or *in-situ*. The basic functions of the package will include camera focusing, the estimation of the quality of fringe patterns, phase difference determination, wrapped phase calculation based on temporal PSI or spatial PSI, and phase unwrapping.

Camera focusing is an important technique in machine vision and imaging. This technique is directly related to the accuracy of information in the fringe pattern acquired from the real world. The four focus measures, grey-level variance [5, 6, 7, 8], image gradient [5, 6, 7], Laplacian [5, 6, 7, 8], and mismatch function variance [9], can be selected for camera focusing.

The estimation of the quality of fringe patterns is a worthwhile piece of work for fringe pattern analysis as the measurements made in optical interferometry are all dependent on the quality of fringe patterns such as intensity, visibility, orientation and SNR. The estimation can also be used for guiding fringe pattern acquisition and optical system alignment.

Phase difference determination is essential for the measurement of many physical quantities in optical interferometry. Fringe pattern matching is a powerful technique for the determination of phase difference between fringe patterns. The size of image patches can be selected according to the required accuracy and the quality of fringe patterns. The computer is programmed to identify the fringe shifting direction and calculate the phase difference based on fringe pattern matching as well as knowledge-based fitting.

The wrapped phase can be obtained from the algorithms of temporal PSI and spatial PSI. Each of them has its own advantages and disadvantages in its applications so that the flexible fringe pattern analysis package should be designed for enabling it to deal with each of them. In the case of temporal PSI, the phase steps can be determined by fringe pattern matching or knowledge-based fitting.

Phase unwrapping is vital to the measurement made by phase-shifting interferometry since this technique integrates the objective phase directly from the wrapped phase data and the unwrapping process is easily affected by noise. Various results may be obtained from various phase unwrapping algorithms in some cases because of the effect of noise. This means that the accuracy varies with different phase unwrapping algorithms under different conditions. Therefore, the combination of the advantages of various phase unwrapping algorithms based on the estimation of the quality of fringe patterns may be a useful approach to phase-shifting interferometry.

In conclusion, the functions of the flexible fringe pattern analysis package may be summarised as the follows:

- Camera focusing including the focus measures of grey-level variance, image gradient, Laplacian and mismatch function variance;
- Fringe quality estimation including intensity, visibility, orientation and SNR;
- Phase difference determination between any two fringe patterns including the methods of fringe pattern matching and knowledge-based fitting;

- Temporal PSI including the algorithms of three-step, four-step, five-step and arbitrary step;
- Spatial PSI including the algorithms of four-pixel, multi-pixel and interpolation;
- Phase unwrapping including the selections of algorithms, thresholds, and unwrapping modes (automatic or semi-automatic processing).

It is clear that the flexible fringe pattern analysis package will make the real-time or *in-situ* measurement based on various algorithms possible at the same time, and bring the researcher both an accurate result and a friendly use of it as any of the functions in the package can be individually selected for particular analysis purpose.

Bibliography

[1] G. Lai and T. Yatagai, "Generalized phase-shifting interferometry," *J. Opt. Soc. Am. A* **8**, 822-827 (1991).

[2] G.S. Han and S.W. Kim, "Numerical correction of reference phases in phase-shifting interferometry by iterative least-squares fitting," *Appl. Opt.* **33**(31), 7321-7325 (1994).

[3] I.B. Kong and S.W. Kim, "General algorithm of phase-shifting Interferometry by iterative least-squares fitting," *Opt. Eng.* 34(1), 183-188 (1995).

[4] K.R. Castleman, *Digital image processing,* Prentice-Hall, Englewood Cliffs and London (1979).

[5] M. Subbarao, T. Choi, and A. Nikzad, "Focusing techniques", *Opt. Eng.* **32**(11), 2824-2836 (1993).

[6] J.H. Lee, K.S. Kim, B.D. Nam, J.C. Lee, Y.M. Kwon, and H.G. Kim, "Implementation of a passive automatic focusing algorithm for digital still camera," *IEEE Trans. on Consumer Electronics* **41**(3), 449-454 (1995).

[7] G. Lightart and F. Groen, "A comparison of different autofocus algorithms," *Proc. IEEE Int. Conf. on Pattern Recognition*, 597-600 (1982).

[8] E. Krotkov, "Focusing," *Int. J. Computer Vis.* **1**, 223-237 (1987).

[9] P.J. Bryanston-Cross and Z. Wang, "Camera Focusing Based on Fringe Pattern Matching," *Appl. Opt.* **36**(25), 6498-6502 (1997).